3

4

5

6

9

10

11

12

13

14

15

16

17

18

19

20

21

22

23

24

25

26

27

28

29 30

31

32

33

34

35

36

37

38

39 40

41

42

43

44

45

46

47

48

49

#### The Vera C. Rubin Observatory Data Preview 1

```
Vera C. Rubin Observatory Team, <sup>1</sup> Tatiana Acero-Cuellar <sup>(1)</sup>, <sup>2</sup> Emily Acosta <sup>(1)</sup>, <sup>1</sup> Christina L. Adair <sup>(1)</sup>, <sup>3</sup>
                  Prakruth Adari , <sup>4</sup> Jennifer K. Adelman-McCarthy , <sup>5</sup> Anastasia Alexov , <sup>1</sup> Russ Allbery , <sup>1</sup>
            Robyn Allsman, Yusra AlSayyad D. 6 Jhonatan Amado D. 5 Nathan Amouroux D. 7 Pierre Antilogus, 8
           alexis Aracena Alcayaga, Gonzalo Aravena-Rojas D, Claudio H. Araya Cortes, Éric Aubourg D, 10
TIM S. AXELROD , <sup>11</sup> JOHN BANOVETZ , <sup>12</sup> CARLOS BARRÍA, AMANDA E. BAUER , <sup>13</sup> BRIAN J. BAUMAN, <sup>14</sup> ELLEN BECHTOL , <sup>15</sup> KEITH BECHTOL , <sup>16</sup> ANDREW C. BECKER , <sup>17</sup> VALERIE R. BECKER , <sup>18</sup> MARK G. BECKET , <sup>19</sup>
                  ERIC C. BELLM , <sup>20</sup> PEDRO H. BERNARDINELLI , <sup>21</sup> FEDERICA B. BIANCO , <sup>2,22,23</sup> ROBERT D. BLUM , <sup>18</sup>
             JOANNE BOGART,<sup>24</sup> ADAM BOLTON D,<sup>3</sup> MICHAEL T. BOOTH,<sup>1</sup> JAMES F. BOSCH D,<sup>6</sup> ALEXANDRE BOUCAUD D,<sup>25</sup>
  Dominique Boutigny , Robert A. Bovill, Andrew Bradshaw, Johan Bregeon, Brian J. Brondel, 27
         Alex Broughton , <sup>24</sup> Audrey Budlong, <sup>28</sup> Dimitri Buffat, <sup>26</sup> Rodolfo Canestrari , <sup>29</sup> Neven Caplar , <sup>20</sup>
                      JEFFREY L. CARLIN , Ross Ceballo , R
     GLENAVER CHARLES-EMERSON, HSIN-FANG CHIANG, JAMES CHIANG, YUMI CHOI, 33 ERIC J. CHRISTENSEN, 5
            Charles F. Claver, Andy W. Clements, Joseph J. Cockrum, Franco Colleoni, Céline Combet 6, 26
                                Andrew J. Connolly , <sup>21</sup> Julio Eduardo Constanzo Córdova , <sup>9</sup> Hans E Contreras, <sup>9</sup>
                 John Franklin Crenshaw (D, 21 Sylvie Dagoret-Campagne (D, 34 Scott F. Daniel, 20 Felipe Daruich, 9
             Guillaume Daubard , <sup>8</sup> Greg Daues, <sup>35</sup> Erik Dennihy , <sup>1</sup> Stephanie JH Deppe , <sup>18</sup> Seth W. Digel , <sup>3</sup>
          Peter E. Doherty, <sup>36</sup> Alex Drlica-Wagner, <sup>5</sup> Gregory P. Dubois-Felsmann, <sup>7</sup> Frossie Economou, <sup>1</sup>
Orion Eiger , 3,24 Lukas Eisert , 3 Alan M. Eisner , 3 Anthony Englert , 39 Baden Erb, Juan A. Fabrega, 9
       Parker Fagrelius, Kevin Fanning, Angelo Fausti Neto, Peter S. Ferguson, Agnès Ferté,
               MERLIN FISHER-LEVINE , 40 GLORIA FONSECA ALVAREZ , 31 MICHAEL D. FOSS, 3 DOMINIQUE FOUCHEZ , 41
                    DAN C. FUCHS D, 3 EMMANUEL GANGLER D, 42 IGOR GAPONENKO, 3 JULEN GARCIA D, 43 JOHN H GATES, 3
                   RANPAL K. GILL , <sup>27</sup> ENRICO GIRO , <sup>44</sup> THOMAS GLANZMAN , <sup>8</sup> ROBINSON GODOY, <sup>9</sup> IAIN GOODENOW, <sup>1</sup>
MIRANDA R. GORSUCH D, 16 MICHELLE GOWER D, 35 MIKAEL GRANVIK D, 45,46 SARAH GREENSTREET D, 33 WEN GUAN D, 12
 THIBAULT GUILLEMIN <sup>10</sup>, <sup>7</sup> LEANNE P. GUY <sup>10</sup>, <sup>9</sup> DIANE HASCALL, <sup>3</sup> AREN NATHANIEL HEINZE <sup>10</sup>, <sup>21</sup> FABIO HERNANDEZ <sup>10</sup>, <sup>47</sup>
           Kenneth Herner , Ardis Herrold, Clare R. Higgs , Is Joshua Hoblitt , Erin Leigh Howard , 20
            MINHEE HYUN , PATRICK INGRAHAM, AVID H. IRVING, ELJKO IVEZIĆ, VI, 20 SUZANNE H. JACOBY, I
          Buell T. Jannuzi , <sup>48</sup> Sreevani Jarugula , <sup>5</sup> M. James Jee , <sup>49,50</sup> Tim Jenness , <sup>1</sup> Toby C. Jennings , <sup>3</sup>
Andrea Jeremie , Garrett Jernigan, 1, David Jiménez Mejías, Anthony S. Johnson , R. Lynne Jones , Roger William Lewis Jones , Claire Juramy-Gilles, Mario Jurić , Steven M. Kahn , Santa Mario Jurić , Steven M. Kahn , Santa Mario Jurić , Santa Mario Ma
 J. Bryce Kalmbach , Yijung Kang , Arun Kannawadi , Jeffrey P. Kantor, Edward Karavakis, Laravakis,
                  KSHITIJA KELKAR , LEE S. KELVIN , IVAN V. KOTOV, CÁBOR KOVÁCS, MIKOLAJ KOWALIK, KSHITIJA KELKAR, KOVÁCS, KELVIN , KOTOV, KOTOV, KOTOV, KOTOV, LEE S. KELVIN , KO
 Victor L. Krabbendam,<sup>1</sup> K. Simon Krughoff D, 1, * Petr Kubánek D, 9 Jacob A. Kurlander D, 21 Mile Kusulja, 26
                  CRAIG S. LAGE , <sup>50</sup> P. J. A. LAGO , <sup>27</sup> KATHERINE LALIOTIS , <sup>55</sup> TRAVIS LANGE , <sup>3</sup> DIDIER LAPORTE, <sup>8</sup>
                      Ryan M. Lau , <sup>33</sup> Juan Carlos Lazarte, <sup>3</sup> Quentin Le Boulc'h , <sup>47</sup> Pierre-François Léget , <sup>6</sup>
                        LAURENT LE GUILLOU , 8 BENJAMIN LEVINE , 4 MING LIANG, 1 SHUANG LIANG, 3 KIAN-TAT LIM , 3
                    Anja von der Linden , <sup>4</sup> Huan Lin , <sup>5</sup> Margaux Lopez , <sup>3</sup> Juan J. Lopez Toro, <sup>9</sup> Peter Love, <sup>52</sup>
                   ROBERT H. LUPTON , NATE B. LUST , LAUREN A. MACARTHUR , SEAN PATRICK MACBRIDE , 56
                 GREG M. MADEJSKI,<sup>24</sup> GABRIELE MAINETTI ,<sup>47</sup> STEVEN J. MARGHEIM ,<sup>6</sup> THOMAS W. MARKIEWICZ ,<sup>5</sup> PHIL MARSHALL ,<sup>50</sup> STUART MARSHALL,<sup>24</sup> GUIDO MAULEN, MORGAN MAY,<sup>57,12</sup> JEREMY MCCORMICK ,<sup>5</sup>
                     DAVID MCKAY , <sup>58</sup> ROBERT MCKERCHER, <sup>1</sup> GUILLEM MEGIAS HOMAR , <sup>59,24</sup> AARON M. MEISNER , <sup>33</sup>
  FELIPE MENANTEAU, 35 HEATHER R. MENTZER , 38 KRISTEN METZGER, 18 JOSHUA E. MEYERS , 44 MICHELLE MILLER, 33
    DAVID J. MILLS, JOACHIM MOEYENS, MARC MONIEZ, FRED E. MOOLEKAMP, C. A. L. MORALES MARÍN, 9,
           FRITZ MUELLER , JAMES R. MULLANEY, FREDDY MUÑOZ ARANCIBIA, KATE NAPIER, HOMER NEAL,
        ERIC H. NEILSEN, JR. 0,5 JEREMY NEVEU 0,34 NIMA SEDAGHAT 0,20 TIMOTHY NOBLE,62 ERFAN NOURBAKHSH 0,6
                  KNUT OLSEN , 3 WILLIAM O'MULLANE, 9 DMITRY ONOPRIENKO, MARCO ORIUNNO, SHAWN OSIER, 3
                Russell E. Owen, <sup>20</sup> Aashay Pai , <sup>32</sup> John K. Parejko , <sup>20</sup> Hye Yun Park , <sup>54</sup> James B. Parsons, <sup>35,*</sup>
                  MARIA T. PATTERSON , <sup>20</sup> MARINA S. PAVLOVIC , <sup>9</sup> KARLA PEÑA RAMÍREZ , <sup>9</sup> JOHN R. PETERSON , <sup>63</sup>
                                       STEPHEN R. PIETROWICZ D, 35 ANDRÉS A. PLAZAS MALAGÓN D, 3,24 REBEKAH POLEN, 54
```

51

52 53

54

55

56

57

58

59

60

61

62

63

64

65

66

67

68

69

70

71

72

73

75

76

77

78

79

81

82

87

88

89

90

91

92

93

94

95

96

97

98

99

100

101

102

103

104

105

```
HANNAH MARY MARGARET POLLEK,<sup>3</sup> PAUL A. PRICE <sup>[D],6</sup> BRUNO C. QUINT <sup>[D],1</sup> JOSÉ MIGUEL QUINTERO MARIN,<sup>9</sup>
             Markus Rabus , <sup>64</sup> Benjamin Racine , <sup>41</sup> Veljko Radeka, <sup>12</sup> Manon Ramel, <sup>26</sup> Arianna Ranabhat , <sup>65</sup>
              Andrew P. Rasmussen , <sup>24</sup> David A. Rathfelder, <sup>66</sup> Meredith L. Rawls , <sup>20</sup> Sophie L. Reed , <sup>67</sup> Kevin A. Reil , <sup>3</sup> David J. Reiss, <sup>20</sup> Michael A. Reuter , <sup>1</sup> Tiago Ribeiro , <sup>1</sup> Mickael Rigault , <sup>67</sup>
                     VINCENT J. RIOT , <sup>14</sup> STEVEN M. RITZ , <sup>38</sup> MARIO F. RIVERA RIVERA, <sup>9</sup> BRANT E. ROBERTSON , <sup>38</sup>
  William Roby D, 37 Gabriele Rodeghiero D, 68 Aaron Roodman D, 24 Luca Rosignoli D, 69, 68 Cécile Roucelle D, 25
         Matthew R. Rumore , <sup>12</sup> stefano russo, <sup>8</sup> Eli S. Rykoff , <sup>24</sup> Andrei Salnikov , <sup>3</sup> Bruno O. Sánchez , <sup>41</sup>
         DAVID SANMARTIM , CLARE SAUNDERS , RAFE H. SCHINDLER, 24 SAMUEL J. SCHMIDT , 50 JACQUES SEBAG, 9
                                      Brian Selvy, <sup>1</sup> Edgard Esteban Sepulveda Valenzuela, <sup>9</sup> Gonzalo Seriche <sup>1</sup>0, <sup>9</sup>
      Jacqueline C. Seron-Navarrete , <sup>9</sup> Ignacio Sevilla-Noarbe , <sup>70</sup> Alysha Shugart , <sup>9</sup> Jonathan Sick , <sup>71,1</sup>
      CRISTIÁN SILVA , MATHEW C. SIMS , ZALADH SINGHAL , KEVIN BENJAMIN SIRUNO, COLIN T. SLATER , ZOLIN T. S
  Brianna M. Smart D, 20 Adam Snyder D, 50 Christine Soldahl, 3 Ioana Sotuela Elorriaga D, 9 Brian Stalder D, 1
                 HERNAN STOCKEBRAND , ALAN L. STRAUSS , MICHAEL A. STRAUSS , KRZYSZTOF SUBERLAK , 20
         IAN S. SULLIVAN (10, 20 JOHN D. SWINBANK (10, 73,6 DIEGO TAPIA (10, 9 ALESSIO TARANTO (10, 68,69 DAN S. TARANU (10, 6
                            John Gregg Thayer, Sandrine Thomas, Adam J. Thornton, Roberto Tighe,
     Laura Toribio San Cipriano, <sup>70</sup> Te-Wei Tsai , <sup>1</sup> Douglas L. Tucker , <sup>5</sup> Max Turri, <sup>3</sup> J. Anthony Tyson , <sup>50</sup>
                      ELANA K. URBACH , <sup>74</sup> YOUSUKE UTSUMI , <sup>75</sup> BRIAN VAN KLAVEREN, WOUTER VAN REEVEN , <sup>9</sup>
            Peter Anthony Vaucher , Paulina Venegas, Aprajita Verma, Antonia Sierra Villarreal , Antonia Sierra Villarreal
     STELIOS VOUTSINAS , CHRISTOPHER W. WALTER , YUANKUN (DAVID) WANG , CHRISTOPHER Z. WATERS , KANDEL STELIOS VOUTSINAS , CHRISTOPHER Z. WATERS , , 
     Christina C. Williams , <sup>33</sup> Beth Willman , <sup>77</sup> Matthias Wittgen , <sup>3</sup> W. M. Wood-Vasey , <sup>78</sup> Wei Yang , <sup>3</sup>
         ZHAOYU YANG D, 12 BRIAN P. YANNY D, 5 PETER YOACHIM D, 20 TIANQING ZHANG D, 78 AND CONGHAO ZHOU D38
                                        Vera C. Rubin Observatory Project Office, 950 N. Cherry Ave., Tucson, AZ 85719, USA
                                  <sup>2</sup> Department of Physics and Astronomy, University of Delaware, Newark, DE 19716-2570, USA
                                       <sup>3</sup>SLAC National Accelerator Laboratory, 2575 Sand Hill Rd., Menlo Park, CA 94025, USA
                                   <sup>4</sup>Department of Physics and Astronomy, Stony Brook University, Stony Brook, NY 11794, USA
                                               <sup>5</sup>Fermi National Accelerator Laboratory, P. O. Box 500, Batavia, IL 60510, USA
                                         <sup>6</sup> Department of Astrophysical Sciences, Princeton University, Princeton, NJ 08544, USA
                    <sup>7</sup> Université Savoie Mont-Blanc, CNRS/IN2P3, LAPP, 9 Chemin de Bellevue, F-74940 Annecy-le-Vieux, France
                       <sup>8</sup> Sorbonne Université, Université Paris Cité, CNRS/IN2P3, LPNHE, 4 place Jussieu, F-75005 Paris, France
                                                 <sup>9</sup> Vera C. Rubin Observatory, Avenida Juan Cisternas #1500, La Serena, Chile
                                   <sup>10</sup> Université Paris Cité, CNRS/IN2P3, CEA, APC, 4 rue Elsa Morante, F-75013 Paris, France
                                  <sup>11</sup>Steward Observatory, The University of Arizona, 933 N. Cherry Ave., Tucson, AZ 85721, USA
                                                                   <sup>12</sup>Brookhaven National Laboratory, Upton, NY 11973, USA
                                                     <sup>13</sup> Yerkes Observatory, 373 W. Geneva St., Williams Bay, WI 53191, USA
                                       <sup>14</sup>Lawrence Livermore National Laboratory, 7000 East Avenue, Livermore, CA 94550, USA
                   <sup>15</sup> Wisconsin IceCube Particle Astrophysics Center, University of Wisconsin—Madison, Madison, WI 53706, USA
                                           <sup>16</sup>Department of Physics, University of Wisconsin-Madison, Madison, WI 53706, USA
                                                                           ^{17}Amazon\ Web\ Services,\ Seattle,\ WA\ 98121,\ USA
                                      <sup>18</sup> Vera C. Rubin Observatory/NSF NOIRLab, 950 N. Cherry Ave., Tucson, AZ 85719, USA
                    <sup>19</sup>Institute for Astronomy, University of Edinburgh, Royal Observatory, Blackford Hill, Edinburgh EH9 3HJ, UK
                                          <sup>20</sup> University of Washington, Dept. of Astronomy, Box 351580, Seattle, WA 98195, USA
  <sup>21</sup> Institute for Data-intensive Research in Astrophysics and Cosmology, University of Washington, 3910 15th Avenue NE, Seattle, WA
                                                                                                             98195, USA
                <sup>22</sup> Joseph R. Biden, Jr., School of Public Policy and Administration, University of Delaware, Newark, DE 19717 USA
                                                     <sup>23</sup> Data Science Institute, University of Delaware, Newark, DE 19717 USA
<sup>24</sup> Kavli Institute for Particle Astrophysics and Cosmology, SLAC National Accelerator Laboratory, 2575 Sand Hill Rd., Menlo Park, CA
                                                                                                             94025, USA
                                        ^{25}\,Universit\'e Paris Cit\'e, CNRS/IN2P3, APC, 4 rue Elsa Morante, F-75013 Paris, France
                             <sup>26</sup> Université Grenoble Alpes, CNRS/IN2P3, LPSC, 53 avenue des Martyrs, F-38026 Grenoble, France
                                                    <sup>27</sup> Vera C. Rubin Observatory/NSF NOIRLab, Casilla 603, La Serena, Chile
                                             <sup>28</sup> University of Washington, Dept. of Physics, Box 351580, Seattle, WA 98195, USA
                   <sup>29</sup> INAF Istituto di Astrofisica Spaziale e Fisica Cosmica di Palermo, Via Ugo la Malfa 153, 90146, Palermo, Italy
                                              <sup>30</sup>LSST Interdisciplinary Network for Collaboration and Computing, Tucson, USA
          <sup>31</sup>Department of Astronomy and Planetary Science, Northern Arizona University, P.O. Box 6010, Flagstaff, AZ 86011, USA
             <sup>32</sup>Department of Astronomy and Astrophysics, University of Chicago, 5640 South Ellis Avenue, Chicago, IL 60637, USA
                                                              <sup>33</sup>NSF NOIRLab, 950 N. Cherry Ave., Tucson, AZ 85719, USA
```

 $^{34}\,Universit\'e\,\,Paris-Saclay,\,\,CNRS/IN2P3,\,\,IJCLab,\,\,15\,\,Rue\,\,Georges\,\,Clemenceau,\,\,F-91405\,\,Orsay,\,\,France$ 106 <sup>35</sup>NCSA, University of Illinois at Urbana-Champaign, 1205 W. Clark St., Urbana, IL 61801, USA 107 <sup>36</sup>Smithsonian Astrophysical Observatory, 60 Garden St., Cambridge MA 02138, USA 108 <sup>37</sup> Caltech/IPAC, California Institute of Technology, MS 100-22, Pasadena, CA 91125-2200, USA 109 <sup>38</sup>Santa Cruz Institute for Particle Physics and Physics Department, University of California-Santa Cruz, 1156 High St., Santa Cruz, 110 CA 95064, USA 111 <sup>39</sup> Department of Physics, Brown University, 182 Hope Street, Providence, RI 02912, USA 112 <sup>40</sup>D4D CONSULTING LTD., Suite 1 Second Floor, Everdene House, Deansleigh Road, Bournemouth, UK BH7 7DU 113 <sup>41</sup> Aix Marseille Université, CNRS/IN2P3, CPPM, 163 avenue de Luminy, F-13288 Marseille, France 114 <sup>42</sup> Université Clermont Auvergne, CNRS/IN2P3, LPCA, 4 Avenue Blaise Pascal, F-63000 Clermont-Ferrand, France 115 <sup>43</sup>C. Iñaki Goenaga, 5, 20600, Guipúzcoa, Spain 116 <sup>44</sup>INAF Osservatorio Astronomico di Trieste, Via Giovan Battista Tiepolo 11, 34143, Trieste, Italy 117 <sup>45</sup>Department of Physics, P.O. Box 64, 00014 University of Helsinki, Finland 118 <sup>46</sup> Asteroid Engineering Laboratory, Luleøa University of Technology, Box 848, SE-981 28 Kiruna, Sweden 119 <sup>47</sup>CNRS/IN2P3, CC-IN2P3, 21 avenue Pierre de Coubertin, F-69627 Villeurbanne, France 120  $^{48}$  University of Arizona, Department of Astronomy and Steward Observatory, 933 N. Cherry Ave, Tucson, AZ 85721, USA 121 <sup>49</sup>Department of Astronomy, Yonsei University, 50 Yonsei-ro, Seoul 03722, Republic of Korea 122 <sup>50</sup> Physics Department, University of California, One Shields Avenue, Davis, CA 95616, USA 123 <sup>51</sup>Space Sciences Lab, University of California, 7 Gauss Way, Berkeley, CA 94720-7450, USA 124 <sup>52</sup>Lancaster University, Lancaster, UK 125 <sup>53</sup> Physics Department, University of California, 366 Physics North, MC 7300 Berkeley, CA 94720, USA <sup>54</sup>Department of Physics, Duke University, Durham, NC 27708, USA <sup>55</sup>Center for Cosmology and Astro-Particle Physics, The Ohio State University, Columbus, OH 43210, USA 128 <sup>56</sup> Physik-Institut, University of Zurich, Winterthurerstrasse 190, 8057 Zurich, Switzerland 129 <sup>57</sup>Department of Physics Columbia University, New York, NY 10027, USA 130 <sup>58</sup>EPCC, University of Edinburgh, 47 Potterrow, Edinburgh, EH8 9BT, UK 131 <sup>59</sup> Department of Aeronautics and Astronautics, Stanford University, Stanford, CA 94305, USA 132 60 soZen Inc., 105 Clearview Dr, Penfield, NY 14526 133 <sup>61</sup> Astrophysics Research Cluster, School of Mathematical and Physical Sciences, University of Sheffield, Sheffield, S3 7RH, United 134 Kinadom135  $^{62}Science$  and Technology Facilities Council, Rutherford Appleton Laboratory, Harwell, UK 136 <sup>63</sup>Department of Physics and Astronomy, Purdue University, 525 Northwestern Ave., West Lafayette, IN 47907, USA 137 <sup>64</sup>Departamento de Matemática y Física Aplicadas, Facultad de Ingeniería, Universidad Católica de la Santísima Concepción, Alonso de 138 Rivera 2850, Concepción, Chile 139  $^{65}Australian\ Astronomical\ Optics,\ Macquarie\ University,\ North\ Ryde,\ NSW,\ Australia$ 140 <sup>66</sup>AURA, 950 N. Cherry Ave., Tucson, AZ 85719, USA 141 <sup>67</sup> Université Claude Bernard Lyon 1, CNRS/IN2P3, IP2I, 4 Rue Enrico Fermi, F-69622 Villeurbanne, France 142 <sup>68</sup>INAF Osservatorio di Astrofisica e Scienza dello Spazio Bologna, Via P. Gobetti 93/3, 40129, Bologna, Italy <sup>69</sup>Department of Physics and Astronomy (DIFA), University of Bologna, Via P. Gobetti 93/2, 40129, Bologna, Italy 144 <sup>70</sup>Centro de Investigaciones Energéticas, Medioambientales y Tecnológicas, Av. Complutense 40, 28040 Madrid, Spain 145  $^{71}J.Sick\ Codes\ Inc.,\ Penetanguishene,\ Ontario,\ Canada$ 146 <sup>72</sup>Science and Technology Facilities Council, UK Research and Innovation, Polaris House, North Star Avenue, Swindon, SN2 1SZ, UK 147 <sup>73</sup>ASTRON. Oude Hoogeveensedijk 4. 7991 PD. Dwingeloo. The Netherlands 148 <sup>74</sup>Department of Physics, Harvard University, 17 Oxford St., Cambridge MA 02138, USA 149 <sup>75</sup> National Astronomical Observatory of Japan, Chile Observatory, Los Abedules 3085, Vitacura, Santiago, Chile 150 <sup>76</sup>Department of Physics, University of Oxford, Denys Wilkinson Building, Keble Road, Oxford, OX1 3RH, UK 151 <sup>77</sup>LSST Discovery Alliance, 933 N. Cherry Ave., Tucson, AZ 85719, USA 152 <sup>78</sup>Department of Physics and Astronomy, University of Pittsburgh, 3941 O'Hara Street, Pittsburgh, PA 15260, USA 153 (Dated: September 5, 2025) 154

#### ABSTRACT

155

156

157

158

We present Rubin Data Preview 1 (DP1), the first data from the NSF-DOE Vera C. Rubin Observatory, comprising raw and calibrated single-epoch images, coadds, difference images, detection catalogs, and ancillary data products. DP1 is based on 1792 optical/near-infrared exposures acquired over 48 distinct nights by the Rubin Commissioning Camera, LSSTComCam, on the Si-

160

161

162

163

164

166

167

168

169

170

171

172

173

174

175

176

177

178

179

180

181

182

183

185

186

187

188

189

190

191

192

193

194

195

196

197

198

199

200

201

monyi Survey Telescope at the Summit Facility on Cerro Pachón, Chile in late 2024. DP1 covers  $\sim 15~\rm deg^2$  distributed across seven roughly equal-sized non-contiguous fields, each independently observed in six broad photometric bands, ugrizy. The median FWHM of the point-spread function across all bands is approximately 1".14, with the sharpest images reaching about 0".58. The  $5\sigma$  point source depths for coadded images in the deepest field, Extended Chandra Deep Field South, are: u=24.55, g=26.18, r=25.96, i=25.71, z=25.07, y=23.1. Other fields are no more than 2.2 magnitudes shallower in any band, where they have nonzero coverage. DP1 contains approximately 2.3 million distinct astrophysical objects, of which 1.6 million are extended in at least one band in coadds, and 431 solar system objects, of which 93 are new discoveries. DP1 is approximately 3.5 TB in size and is available to Rubin data rights holders via the Rubin Science Platform, a cloud-based environment for the analysis of petascale astronomical data. While small compared to future LSST releases, its high quality and diversity of data support a broad range of early science investigations ahead of full operations in late 2025.

211

214

216

217

221

223

227

Keywords: Rubin Observatory - LSST

#### 1. INTRODUCTION

The National Science Foundation (NSF)-Department of Energy (DOE) Vera C. Rubin Observatory is a ground-based, wide-field optical/near-infrared facility located on Cerro Pachón in northern Chile. Named in honor of Vera C. Rubin, a pioneering astronomer whose groundbreaking work in the 20th century provided the first convincing evidence for the existence of dark matter (V. C. Rubin & W. K. Ford 1970; V. C. Rubin et al. 1980), the observatory's prime mission is to carry out the Legacy Survey of Space and Time (formerly Large Synoptic Survey Telescope) (LSST) (Ž. Ivezić et al. 2019a). This 10-year survey is designed to obtain rapid-cadence, multi-band imaging of the entire visible southern sky approximately every 3-4 nights. Over its main 18,000 deg<sup>2</sup> footprint, the LSST is expected to reach a depth of  $\sim 27$  magnitude in the r-band, with  $\sim 800$  visits per pointing in all filters (F. B. Bianco et al. 2022).

The Rubin Observatory system consists of four main components: the Simonyi Survey Telescope, featuring an 8.4 m diameter (6.5 m effective aperture) primary mirror that delivers a wide field of view; a 3.2-gigapixel camera, capable of imaging 9.6 square degrees per exposure<sup>79</sup> with seeing-limited quality in six broadband filters, *ugrizy* (320–1050 nm); an automated Data Management System that processes and archives tens of terabytes of data per night, generating science-ready data products within minutes for a global community of scientists; and an Education and Public Outreach (EPO)

program that provides real-time data access, interactive tools, and educational content to engage the public. The integrated system's étendue<sup>80</sup> of  $319~\text{m}^2~\text{deg}^2$ , is over an order of magnitude larger than that of any previous optical observatory, enabling a fast, large-scale survey with exceptional depth in a fraction of the time compared to other observatories.

The observatory's design is driven by four key science themes: probing dark energy and dark matter; taking an inventory of the solar system; exploring the transient and variable optical sky; and mapping the Milky Way (Ž. Ivezić et al. 2019a). These themes inform the optimization of a range of system parameters, including image quality, photometric and astrometric accuracy, the depth of a single visit and the co-added survey depth, the filter complement, the total number of visits per pointing as well as the distribution of visits on the sky, and total sky coverage. Additionally, they inform the design of the data processing and access systems. By optimizing the system parameters to support a wide range of scientific goals, we maximize the observatory's scientific output across all areas, making Rubin a powerful discovery machine capable of addressing a broad range of astrophysical questions.

Throughout the duration of the LSST, Rubin Observatory will issue a series of Data Releases, each representing a complete reprocessing of all LSST data collected up to that point. Prior to the start of the LSST survey, commissioning activities will generate a significant volume of science-grade data. To make this early data available to the community, the Rubin Early Science Program (L. P. Guy et al. 2025) was established.

<sup>\*</sup> Author is deceased

<sup>79</sup> We define an "exposure" as the process of exposing all detectors in the focal plane. It is synonymous with the term "visit" in DP1. By contrast, an "image" is the output of a single detector following an exposure.

No. The product of the primary mirror area and the angular area of its field of view for a given set of observing conditions.

One key component of this program is a series of Data Previews; early versions of the LSST Data Releases. These previews include preliminary data products derived from both simulated and commissioning data, which, together with early versions of the data access services, are intended to support high-impact early science, facilitate community readiness, and inform the development of Rubin's operational capabilities ahead of the start of full survey operations. All data and services provided through the Rubin Early Science Program are offered on a shared-risk basis<sup>81</sup>.

234

235

236

237

238

239

240

241

242

243

244

245

246

247

248

249

250

251

252

253

254

255

256

257

258

259

260

262

263

264

265

266

267

269

270

271

272

273

274

275

276

277

This paper describes Rubin's second of three planned Data Previews: Data Preview 1 (DP1) (NSF-DOE Vera C. Rubin Observatory 2025a). The first, Data Preview 0 (DP0)<sup>82</sup>, contained data products produced from the processing of simulated LSST-like data sets, together with a very early version of the Rubin Science Platform (M. Jurić et al. 2019). DP1 contains data products derived from the reprocessing of science-grade exposures acquired by the Rubin Commissioning Camera (LSST-ComCam), in late 2024. The third and final Data Preview, Data Preview 2 (DP2), is planned to be based on a reprocessing of all science-grade data taken with the Rubin's LSST Science Camera (LSSTCam) during commissioning and is expected to be released around mid-2026.

All Rubin Data Releases and Previews are subject to a two-year proprietary period, with immediate access granted exclusively to LSST data rights holders (R. Blum & the Rubin Operations Team 2020). Data rights holders<sup>83</sup> are individuals or institutions with formal authorization to access proprietary data collected by the Vera C. Rubin Observatory. After the two-year proprietary period, DP1 will be made public.

304

310

311

312

313

316

317

318

319

322

323

326

327

In this paper, we present the contents and validation of, and the data access and community support services for, Rubin DP1, the first Data Preview to deliver data derived from observations conducted by the Vera C. Rubin Observatory. DP1 is based on the reprocessing of 1792 science-grade exposures acquired during the first on-sky commissioning campaign conducted in late 2024. It covers a total area of approximately  $\sim 15~\rm deg^2$  distributed across seven distinct non-contiguous fields. The data products include raw and calibrated single-epoch images, coadded images, difference images, de-

tection catalogs, and other derived data products. DP1 is about 3.5 TB in size and contains around 2.3 million distinct astronomical objects, detected in 2644 coadded images. Full DP1 release documentation is available at https://dp1.lsst.io. Despite Rubin Observatory still being in commissioning and not yet complete at the time the observations were acquired, Rubin DP1 provides an important first look at the data, showcasing its characteristics and capabilities.

The structure of this paper is as follows. In section 2 we describe the observatory system and overall construction and commissioning status at the time of data acquisition, the seven fields included in DP1, and the observing strategy used. Section 3 summarizes the contents of DP1 and the data products contained in the release. The data processing pipelines are described in section 4, followed by a description of the data validation and performance assessment in section 5. Section 6 describes the Rubin Science Platform (RSP), a cloudbased data science infrastructure that provides tools and services to Rubin data rights holders to access, visualize and analyze peta-scale data generated by the LSST. Section 7 presents the Rubin Observatory's model for community support, which emphasizes self-help via documentation and tutorials, and employs an open platform for issue reporting that enables crowd-sourced solutions. Finally, a summary of the DP1 release and information on expected future releases of data is given in section 8. The appendix contains a useful glossary of terms used throughout this paper.

All magnitudes quoted are in the AB system (J. B. Oke & J. E. Gunn 1983), unless otherwise specified.

#### 2. ON-SKY COMMISSIONING CAMPAIGN

The first Rubin on-sky commissioning campaign was conducted using the LSSTComCam. The campaign's primary objective was to optically align the Simonyi Survey Telescope and verify its ability to deliver acceptable image quality using LSSTComCam. In addition, the campaign provided valuable operations experience to facilitate commissioning the full LSSTCam (T. Lange et al. 2024; A. Roodman et al. 2024). We note that commissioning LSSTComCam was not an objective of the campaign. Instead, LSSTComCam was used as a tool to support broader observatory commissioning, including early testing of the Active Optics System (AOS) and the LSST Science Pipelines. As a result, many artifacts present in the data are specific to LSSTComCam and will be addressed only if they persist with LSST-Cam. Accordingly, the image quality achieved during this campaign, and in the DP1 data, do not reflect the performance ultimately expected from LSSTCam.

<sup>81</sup> Shared risk means early access with caveats: the community benefits from getting a head start on science, preparing analyses, and providing feedback, while also accepting that the system may not work as well as it will during full operations.

 $<sup>^{82}</sup>$  See https://dp0.lsst.io

<sup>83</sup> See https://www.lsst.org/scientists/international-drh-list

331

332

333

334

335

336

337

338

339

340

341

342

343

344

345

346

347

348

349

350

351

352

353

354

355

356

357

358

360

361

363

364

365

367

368

369

370

371

372

373

374

375

376

377

378

379

380

Approximately 16,000 exposures were collected during this campaign, the majority in support of AOS commissioning, system-level verification, and end-to-end testing of the telescope's hardware and software. This included over 10000 exposures for AOS commissioning, more than 2000 bias and dark calibration frames, and over 2000 exposures dedicated to commissioning the LSST Science Pipelines. For DP1, we have selected a subset of 1792 science-grade exposures from this campaign that are most useful for the community to begin preparing for early science.

391

392

305

402

403

418

At the time of the campaign, the observatory was still under construction, with several key components, such as dome thermal control, full mirror control, and the final AOS configuration either incomplete or still undergoing commissioning. As a result, image quality varied widely throughout the campaign and exhibited a broader distribution than is expected with LSST-Cam. Despite these limitations, the campaign successfully demonstrated system integration and established a functional observatory.

#### 2.1. Simonyi Survey Telescope

The Simonyi Survey Telescope (B. Stalder et al. 2024) features a unique three-mirror design, including an 8.4meter Primary Mirror Tertiary Mirror (M1M3) fabricated from a single substrate, and a 3.5-meter Secondary Mirror (M2). This compact configuration supports a wide 3.5-degree field of view while enabling exceptional stability, allowing the telescope to slew and settle in under five seconds. To achieve the scientific goals of the 10-year LSST, the Observatory must maintain high image quality across its wide field of view (Ž. Ivezić et al. 2019b). This is accomplished through the AOS (B. Xin et al. 2015; G. Megias Homar et al. 2024), which corrects, between successive exposures, wavefront distortions caused by optical misalignments and mirror surface deformations, primarily due to the effect of gravitational and thermal loads.

The AOS, which comprises an open-loop component and a closed-loop component, optimizes image quality by aligning the camera and M2 relative to M1M3, as well as adjusting the shapes of all three mirrors to nanometer precision. The AOS open-loop component corrects for predictable distortions and misalignments, while the closed-loop component addresses unpredictable or slowly varying aberrations using feedback from the corner wavefront sensors. The closed-loop wavefront sensing technique is curvature wavefront sensing, which infers wavefront errors in the optical system by analyzing extra- and intra-focal star images (S. Thomas et al. 2023). Since LSSTComCam lacks dedi-

cated wavefront sensors, wavefront errors were instead estimated by defocusing the telescope  $\pm 1.5$  mm on either side of focus and applying the curvature wavefront sensing pipeline to the resulting images. Each night began with an initial alignment correction using a laser tracker to position the system within the capture range of the closed-loop algorithm (G. Megias Homar et al. 2024). Once this coarse alignment was complete, the AOS refined the optical alignment and applied mirror surfaces corrections to optimize the image quality across the LSSTComCam field of view.

During LSST Science Pipelines commissioning (§2.4), observations were conducted using the AOS in open-loop mode only, without closed-loop corrections between exposures. Closed-loop operation, which requires additional intra- and extra-focal images with LSSTCom-Cam, was not compatible with the continuous data acquisition needed by the pipelines. The image quality for these data was monitored by measuring the Point Spread Function (PSF) Full Width at Half-Maximum (FWHM), and closed-loop sequences were periodically run when image quality degradation was observed.

#### 2.2. The LSST Commissioning Camera

LSSTComCam (B. Stalder et al. 2022, 2020; J. Howard et al. 2018; SLAC National Accelerator Laboratory & NSF-DOE Vera C. Rubin Observatory 2024) is a 144-megapixel version of the 3.2-gigapixel LSST-Cam. It covers approximately 5% of the LSSTCam focal plane area, with a field of view of  $\sim 0.5 \text{ deg}^2$  (40'x40'), compared to LSSTCam's 9.6 deg<sup>2</sup>. It was developed to validate camera interfaces with other observatory components and evaluate overall system performance prior to the start of LSSTCam commissioning. Although it has a smaller imaging area, LSSTComCam shares the same plate scale of 0".2 per pixel and is housed in a support structure that precisely replicates the total mass, center of gravity, and physical dimensions of LSSTCam. All mechanical and utility interfaces to the telescope are implemented identically, enabling full end-to-end testing of observatory systems, including readout electronics, image acquisition, and data pipelines.

The LSSTCam focal plane is composed of 25 modular rafts arranged in a  $5\times 5$  grid; 21 rafts are dedicated to science imaging, while four corner rafts are used for guiding and wavefront sensing. Each science raft is a self-contained unit comprising nine  $4K\times 4K$  Charge-Coupled Device (CCD) (G. E. Smith 2010) sensors arranged in a  $3\times 3$  mosaic, complete with integrated readout electronics and cooling systems. Each sensor is subdivided into 16 segments arranged in a  $2\times 8$  layout, with each segment consisting of  $512\times 2048$  pixels and read out in par-

allel using individual amplifiers. LSSTCam uses CCD sensors from two vendors: Imaging Technology Laboratory, University of Arizona (UA)) (ITL) and Teledyne (E2V). To maintain uniform performance and calibration each raft is populated with sensors from only one vendor.

432

433

434

435

436

437

438

439

440

441

442

443

444

445

446

447

448

449

450

451

453

454

455

456

457

458

459

LSSTComCam consists of a single science raft equipped exclusively with ITL sensors. The sensors selected for LSSTComCam represent the best performing of the remaining ITL devices after the LSSTCam rafts were fully populated. They exhibit known issues such as high readout noise (e.g., Detector 8, S22 in Figure 2) and elevated Charge Transfer Inefficiency (CTI) (e.g., Detector 5, S12 in Figure 2). As a result, certain image artifacts present in the DP1 dataset may be specific to LSSTComCam. Although the cryostat in LSST-ComCam, uses a different cooling system than that of LSSTCam, LSSTComCam incorporated a refrigeration pathfinder to validate the cryogenic refrigeration system intended for LSSTCam,. Figure 1 shows the single-raft LSSTComCam positioned at the center of the full LSST-Cam focal plane, corresponding to the central science raft position. LSSTComCam is designated as Raft 22 (R22).

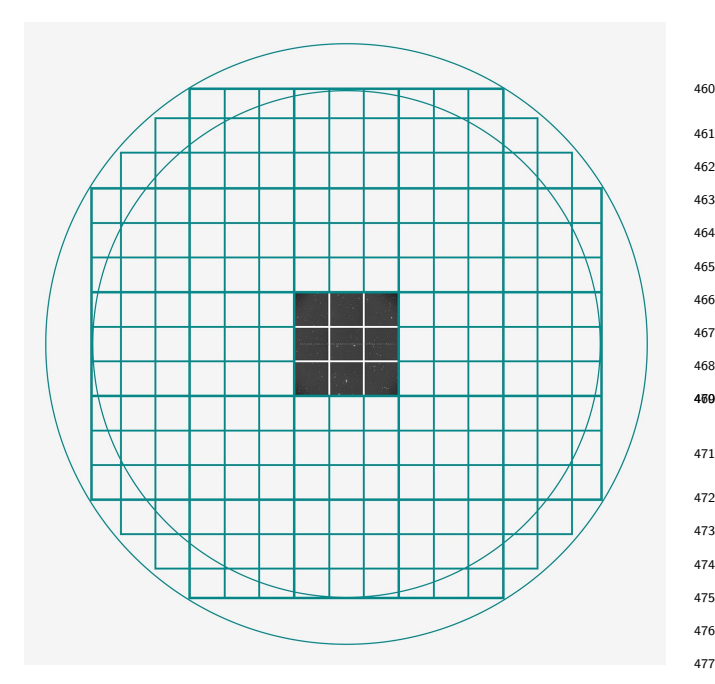


**Figure 1.** Schematic showing the single-raft LSSTComCam positioned at the center of the full LSSTCam focal plane. The perspective is from above, looking down through the LSSTComCam lenses onto the focal plane. Credit: RubinObs/NOIRLab/SLAC/NSF/DOE/AURA.

The LSSTCam and LSSTComCam focal planes are described in detail in A. A. Plazas Malagón et al. (2025).

482

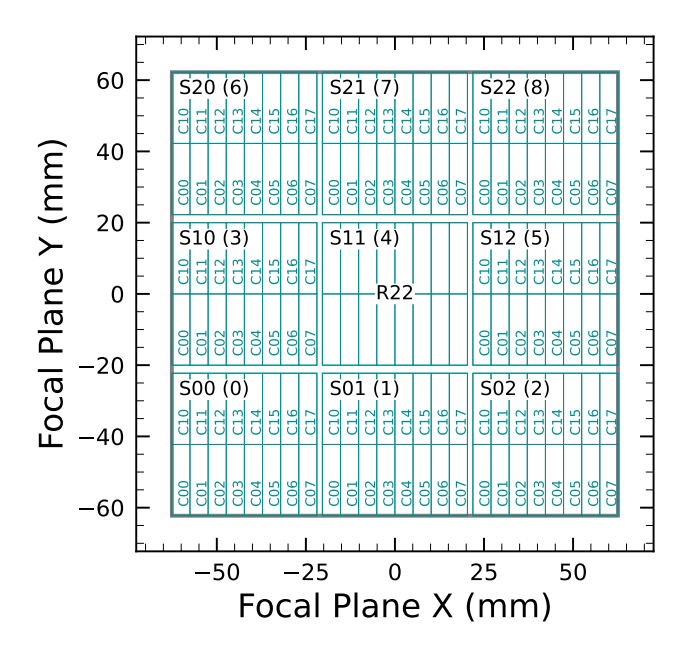


Figure 2. LSSTComCam focal plane layout illustrating the placement and numbering scheme of sensors (S) and amplifiers (C). The view is looking down from above the focal plane through the LSSTComCam lenses. Each sensor contains 16 amplifiers, and a group of nine sensors comprises one raft. LSSTComCam is Raft 22 (R22). The detector number for each sensor is shown in parentheses.

#### 2.2.1. Filter Complement

LSSTComCam supports imaging with six broadband filters ugrizy spanning 320–1050 nm, identical in design to LSSTCam. Whereas the LSSTCam filter exchanger holds five filters, the LSSTComCam exchanger holds only three at a time. The full-system throughput of the six LSSTComCam filters, which encompasses contributions from a standard atmosphere at airmass 1.2, telescope optics, camera surfaces, and the mean ITL detector quantum efficiency is shown in Figure 3.

#### 2.2.2. Timing Calibration

The absolute time accuracy of data taken with LSST-ComCam relies on the Network Time Protocol (NTP) for clock synchronization, which should be accurate to approximately 1 millisecond. In order to evaluate the absolute timing accuracy of the entire system we observed the geosynchronous satellite EUTELSAT 117 West B with a set of 10 usable 10-second exposures over two nights. EUTELSAT 117 West B is part the GPS system and serves as one of the WAAS (Wide Area Augmentation System) satellites operated for the U.S. Federal Aviation Administration (FAA) and used to broadcast GPS corrections to air traffic.

As these satellites are part of the GPS system, their positions are tracked very precisely and the record of

487

488

490

491

493

494

495

496

497

498

499

500

501

502

503

504

505

506

507

508

509

510

511

512

513

514

515

516

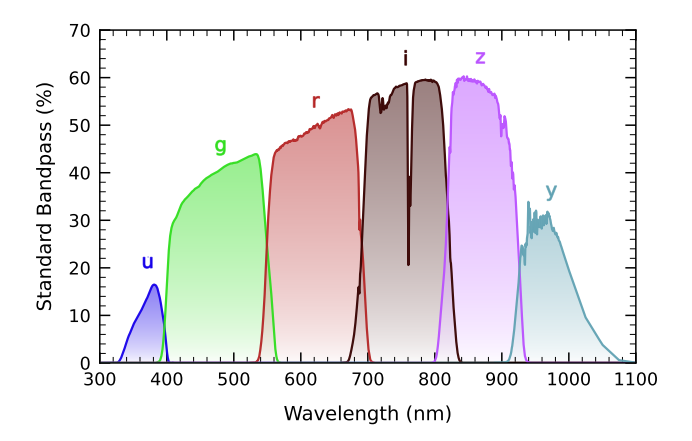


**Figure 3.** LSSTComCam standard bandpasses, illustrating full system throughput. The bandpasses include a standard atmosphere at airmass 1.2, telescope optics, camera surfaces, and mean ITL detector quantum efficiency.

their locations is published after the fact and can be downloaded. Following the technique previously employed by other surveys, (J. L. Tonry et al. 2018), we observed the satellite while tracking the sky and then downloaded the data-files with its precise locations from the National Satellite Test Bed web site<sup>84</sup>. By comparing the measured and predicted locations of the start of the satellite track on the sky, we determined that (relative to the start of integration-time recorded in the FITS headers) our time was accurate to  $53.6 \pm 11.0$  milliseconds.

This work continues to be an area of ongoing study, as the exact timing of when the shutter open command is issued, and the complete profile of the shutter movement are not yet determined. However the open command is on average near 29 milliseconds later. Incorporating the delays into the fit reduces the offset to  $24.8 \pm 11.0$  milliseconds.

The full shutter takes approximately 396 milliseconds to completely open. As the LSSTComCam sensors are centered in the aperture, the center of the focal plane should be exposed about half-way through the shutter open procedure, 198 milliseconds after the open command. There are uncertainties on the full motion profile, and the blade direction motions are currently not known, but the fraction of the shutter aperture subtended by the focal plane is 52%. This implies that the shutter will pass any pixel between 198  $\pm$  103 milliseconds. Subtracting this from the fitted delay of 24.8 milliseconds and adding the fitted error of 11.0 milliseconds in quadrature, results in a current conservative estimate

of the delay of -173.2  $\pm$  104.1 milliseconds, consistent with and smaller than the constraints on the timing offset determined using astrometric residuals from known asteroid associations presented in §5.10.2.

518

520

521

522

523

524

525

526

538

539

541

543

554

557

566

567

#### 2.3. Flat Field System

During the on-sky campaign, key components of the Rubin calibration system (P. Ingraham et al. 2022), including the flat field screen, had not yet been installed. As a result, flat fielding for DP1 relied entirely on twilight flats. While twilight flats pose challenges such as non-uniform illumination and star printthrough, they were the only available option during LSSTComCam commissioning and for DP1 processing. To mitigate these limitations, dithered, tracked exposures were taken over a broad range of azimuth and rotator angles to construct combined flat calibration frames. Exposure times were dynamically adjusted to reach target signal levels of between 10,000 and 20,000 electrons. Future campaigns will benefit from more stable and uniform flat fielding using the Rubin flat field system, described in P. Fagrelius & E. S. Rykoff (2025).

#### 2.4. LSST Science Pipelines Commissioning

Commissioning of the LSST Science Pipelines, (Rubin Observatory Science Pipelines Developers 2025), began once the telescope was able to routinely deliver subarcsecond image quality. The goals included testing the internal astrometric and photometric calibration across a range of observing conditions, validating the difference image analysis and Prompt Processing (K.-T. Lim 2023) framework, and accumulating over 200 visits per band to evaluate deep coadded images with integrated exposure times roughly equivalent to those of the planned LSST Wide Fast Deep (WFD) 10-year depth. To support these goals, seven target fields were selected that span a range of stellar densities, overlap with external reference datasets, and collectively span the full breadth of the four primary LSST science themes. These seven fields form the basis of the DP1 dataset. Figure 4 shows the locations of these seven fields on the sky, overlaid on the LSST baseline survey footprint (R. L. Jones et al. 2021; P. Yoachim 2022; Rubin's Survey Cadence Optimization Committee et al. 2022, 2023, 2025), along with sky coverage of both the LSSTCam and LSSTComCam focal planes.

Each of the seven target fields was observed repeatedly in multiple bands over many nights. A typical observing epoch on a given target field consisted of 5-20 visits in each of the three loaded filters (§2.2.1). All DP1 images were captured as single  $1\times30$ -second exposures for all bands, rather than as  $2\times15$ -second "snap" exposures. Additionally, some u-band exposures were taken

<sup>84</sup> https://www.nstb.tc.faa.gov/nstbarchive.html

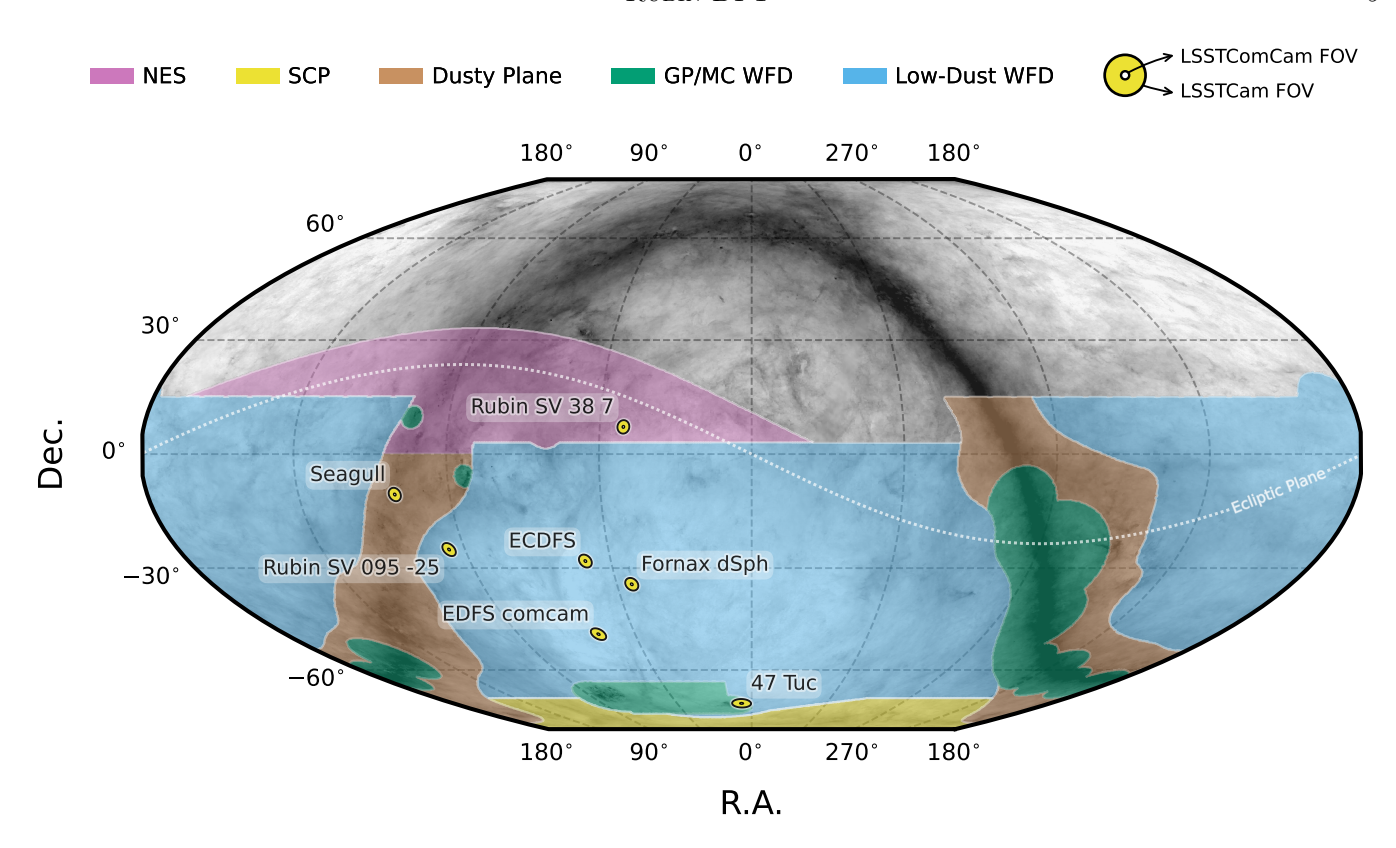


Figure 4. Locations of the seven DP1 fields overlaid on the LSST baseline survey footprint (Rubin's Survey Cadence Optimization Committee et al. 2025). NES: North Ecliptic Spur, SCP: South Celestial Pole, Low-Dust WFD: regions away from the Galactic Plane (GP) observed with a WFD cadence, GP/MC WFD: Galactic Plane and Magellanic Clouds regions observed with a WFD cadence. The fields of view covered by the LSSTCam and LSSTComCam focal planes are represented as outer and inner concentric circles, respectively, centered on the pointing center of each field.

as 38-second exposures. The exposure time for LSST images will be determined following further testing during the commissioning phase with LSSTCam. All images were acquired using the Rubin Feature-Based Scheduler (FBS), version 3.0 (E. Naghib et al. 2019; P. Yoachim et al. 2024). Table 1 lists the seven DP1 fields and their pointing centers, and provides a summary of the band coverage in each.

The temporal sampling distribution of observations per band and per night is shown in Figure 5. Gaps in coverage across some bands arise from the fact that LSSTComCam can only hold three filters at a time (see §2.2.1). As the campaign progressed, the temporal sampling became denser across all fields, reflecting improved efficiency and increased time allocated for science observations.

It is important to note that the time sampling in the DP1 dataset differs significantly from what will be seen in the final LSST data. Table 2 lists the  $5\sigma$  point source depths for coadded images per field and per band, where coverage in a band is non-zero.

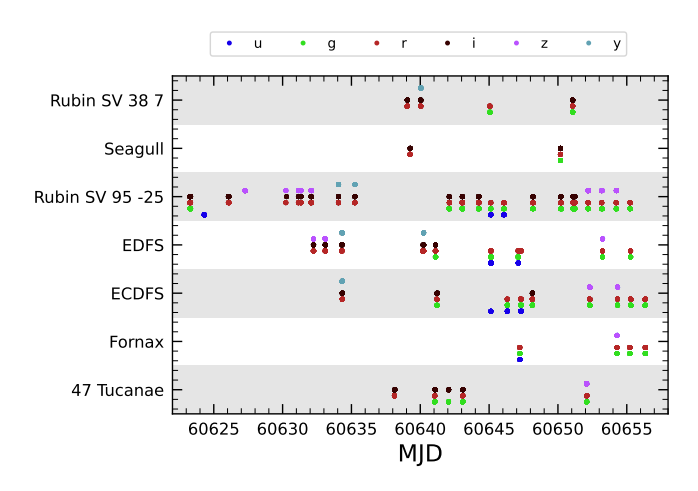


Figure 5. Distribution of DP1 observations by date grouped by field as a function of time over the 48 nights of data taking with LSSTComCam. Each dot represents a single exposure, color-coded by band.

All fields except for the low ecliptic latitude field, Rubin\_SV\_38\_7, used a small random dithering pattern. The random translational dithers of the telescope bore-

596

597

598

599

600

601

602

603

605

606

607

608

609

611

612

613

614

**Table 1.** DP1 fields and pointing centers with the number of exposures in each band per field. ICRS coordinates are in units of decimal degrees, and are specified as J2000.

Field Code	Field Name	RA	DEC	Band		Total				
		deg	deg	$\overline{u}$	g	r	i	z	y	•
47_Tuc	47 Tucanae Globular Cluster	6.128	-72.090	6	10	32	19	0	5	72
ECDFS	Extended Chandra Deep Field South	53.160	-28.100	43	230	237	162	153	30	855
EDFS_comcam	Rubin SV Euclid Deep Field South	59.150	-48.730	20	61	87	42	42	20	272
$Fornax\_dSph$	Fornax Dwarf Spheroidal Galaxy	40.080	-34.450	0	5	25	12	0	0	42
$Rubin\_SV\_095\25$	Rubin SV Low Galactic Latitude Field	95.040	-25.000	33	82	84	23	60	10	292
$Rubin\_SV\_38\_7$	Rubin SV Low Ecliptic Latitude Field	37.980	7.015	0	44	40	55	20	0	159
Seagull	Seagull Nebula	106.300	-10.510	10	37	43	0	10	0	100
Total				112	469	548	313	285	65	1792

618

610

620

622

624

625

626

627

629

641

642

643

645

Table 2. Median  $5\sigma$  coadd point source detection limits per field and band.

Field Code	Band							
	$\overline{u}$	g	r	i	z	$\overline{y}$		
47_Tuc	-	24.03	24.24	23.90	-	21.79		
ECDFS	24.55	26.18	25.96	25.71	25.07	23.10		
$EDFS\_comcam$	23.42	25.77	25.72	25.17	24.47	23.14		
$Fornax\_dSph$	-	24.53	25.07	24.64	-	-		
$Rubin\_SV\_095\25$	24.29	25.46	24.95	24.86	24.32	22.68		
$Rubin\_SV\_38\_7$	-	25.46	25.15	24.86	23.52	-		
Seagull	23.51	24.72	24.19	-	23.30	-		

sight were applied for each visit, with offsets of up to 0.2 degrees around the pointing center (Table 1). The rotational dithers of the camera rotator were typically approximately 1 degree per visit, with larger random offsets at each filter change, which worked to keep operational efficiency high. The Rubin\_SV\_38\_7 field used a different dither pattern to optimize coverage of Solar System Objects and test Solar System Object linking across multiple nights. These observations used a  $2\times2$  grid of LSSTComCam pointings to cover an area of about 1.3 degree×1.3 degrees. The visits cycled between the grid's four pointing centers, using small random translational dithers to fill chip gaps with the goal of acquiring 3-4 visits per pointing center per band in each observing epoch.

## 2.5. Delivered Image Quality

The delivered image quality is influenced by contributions from both the observing system (i.e., dome, telescope and camera) and the atmosphere. During the campaign, the Rubin Differential Image Motion Monitor (DIMM) was not operational, so atmospheric seeing was estimated using live data from the Southern Astrophysical Research Telescope (SOAR) Ring-Image Next Generation Scintillation Sensor (RINGSS) seeing monitor, also located on Cerro Pachón. Although accelerometers mounted on the mirror cell and top-end assembly were available to track dynamic optics effects, such as mirror oscillations that can degrade optical alignment, this data was not used during the campaign. Mount encoder data were used to measure the mount jitter in every image, with a measured median contribution of 0.004 arcseconds to image degradation. As the pointing model was not fine-tuned, tracking errors could range from 0.2 to 0.4 arcseconds per image, depending on RA and Dec. Dome and mirror-induced seeing were not measured during the campaign.

The DP1 median delivered image quality across all bands is 1".14, as measured by the PSF FWHM. The best images achieved a PSF FWHM of approximately 0".58. Ongoing efforts aim to quantify all sources of image degradation, including contributions from the camera system, static and dynamic optical components, telescope mount motion, observatory-induced seeing from the dome and mirror, and atmospheric conditions.

## 3. OVERVIEW OF THE CONTENTS OF RUBIN DP1

Here we describe Rubin DP1 data products and provide summary statistics for each. The DP1 science data products are derived from the 15972 individual CCD images taken across 1792 exposures in the seven LSST-ComCam commissioning fields (§2.4).

The data products that comprise DP1 provide an early preview of future LSST data releases and are strongly dependent on the type and quality of the data that was

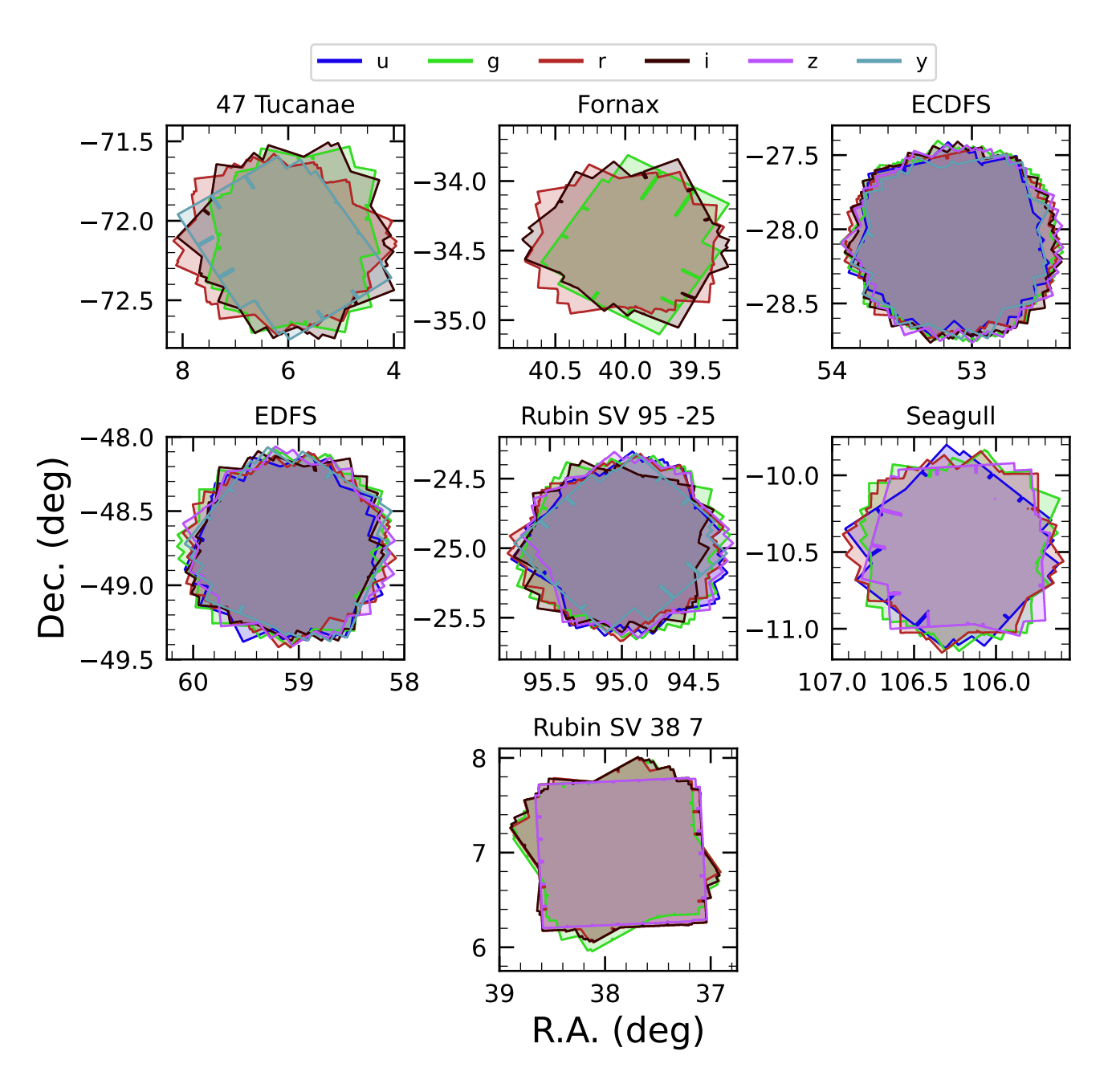


Figure 6. Sky coverage maps showing the distribution of visits in each field, color coded by band. The images clearly show the focal plane chip gaps and dithering pattern. Only the detectors for which single frame processing succeeded are included in the plots, which explains why the central region of 47\_Tuc looks thinner than the other fields.

collected during LSSTComCam on-sky campaign (§2.4). Consequently not all anticipated LSST data products, as described in the Data Product Definition Document (DPDD) (M. Jurić et al. 2023) were produced for the DP1 dataset.

651

652

653

654

655

656

657

Rubin Observatory has adopted the convention by which single-epoch detections are referred to as Sources. By contrast, the astrophysical object associated with a given detection is referred to as an Object <sup>85</sup>. As such, a given Object will likely have multiple associated Sources, since it will be observed in multiple epochs.

At the highest level, the DP1 data products fall into one of five types:

<sup>85</sup> We caution that this nomenclature is not universal; for example, some surveys call "detections" what we call "sources", and use the term "sources" for what we call "objects".

665

667

668

669

670

671

672

673

674

675

676

677

678

679

680

681

682

683

684

685

686

687

688

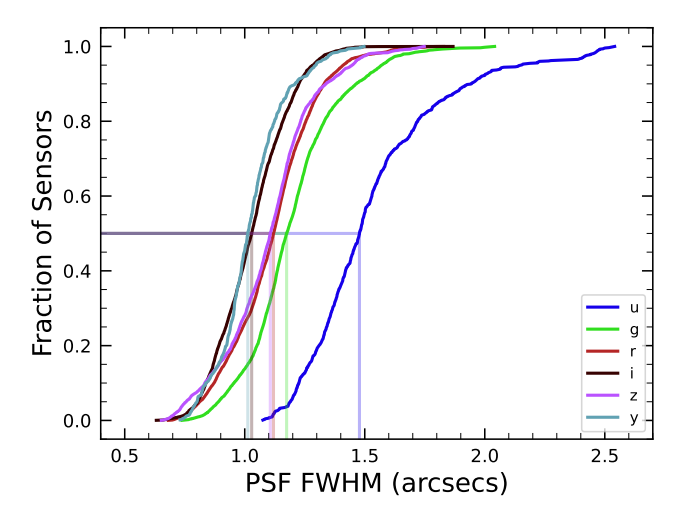


Figure 7. Cumulative distribution of PSF FWHM (arcsec) over all 16071 visits images in the DP1 dataset for each filter. The vertical dashed lines represent the median PSF FWHM at 1.46, 1.36, 1.24, 1.18 and 1.20 arcsec for the *ugrizy* wavebands, respectively.

- Images, including single-epoch images, deep and template coadded images, and difference images;
- Catalogs of astrophysical Sources and Objects detected and measured in the aforementioned images. We also provide the astrometric and photometric reference catalog generated from external sources that was used during processing to generate the DP1 data products;
- Maps, which provide non-science-level visualizations of the data within the release. They include, for example, zoomable multi-band images and coverage maps;
- Ancillary data products, including, for example, the parameters used to configure the data processing pipelines, log and processing performance files, and calibration data products (e.g., CTI models, brighter-fatter kernels, etc.);

715

Metadata in the form of tables containing information about each visit and processed image, such as pointing, exposure time, and a range of image quality summary statistics.

While images and catalogs are expected to be the primary data products for scientific research, we also recognize the value of providing access to other data types to support investigations and ensure transparency.

**Table 3.** Tract coverage of each DP1 field. The size of a tract is larger than the LSSTCam field of view; however, since each observed field extends across more than one tract, each field covers multiple tracts.

Field Code	Tract ID
47_Tuc	453, 454
ECDFS	4848, 4849, 5062, 5063, 5064
$EDFS\_comcam$	2234, 2235, 2393, 2394
$Fornax\_dSph$	4016,  4017,  4217,  4218
$Rubin\_SV\_095\25$	5305, 5306, 5525, 5526
$Rubin\_SV\_38\_7$	$10221,\ 10222,\ 10463,\ 10464,\ 10704,$
	10705
Seagull	7610, 7611, 7849, 7850

To facilitate processing, Rubin DP1 uses a single skymap<sup>86</sup> that covers the entire sky area encompassing the seven DP1 fields. The DP1 skymap divides the entire celestial sphere into 18938 tracts, each covering approximately 2.8 deg<sup>2</sup>. Each tract is further subdivided into 10 times 10 equally-sized patches, with each patch covering roughly 0.028 deg<sup>2</sup>. Both tracts and patches overlap with their neighboring regions. Since the LSST-ComCam only observed  $\sim 15 \text{ deg}^2$  of the sky during its campaign, only 29 out of the 18938 tracts have coverage in DP1. The tract identification numbers and corresponding target names for these tracts are listed in Table 3. The size of a tract is larger than the LSSTCam field of view; however, since each observed field extends across more than one tract, each field covers multiple tracts.

The skymap is integral to the production of co-added images. To create a coadded image, the processing pipeline selects all calibrated science images in a given field that meet specific quality thresholds (§3.1 and §4.5.1) for a given patch, warps them onto a single consistent pixel grid for that patch, as defined by the skymap, then coadds them. Each individual coadd image therefore covers a single patch. Coadded images and the catalogs of detections from them are termed tractlevel data products. By contrast, visit-level data products are those derived from individual LSSTComCam exposures, such as a raw image or a catalog of detections from a single calibrated image. Most science data products (i.e., images and catalogs) in DP1 are either tract

<sup>&</sup>lt;sup>86</sup> A skymap is a tiling of the celestial sphere, organizing largescale sky coverage into manageable sections for processing and analysis.

or visit—level, the main exception being the Calibration reference catalog.

Throughout this section, the data product names are indicated using monospace font. Data products are accessed via either the International Virtual Observatory Alliance (IVOA) Services (§6.2.1) or the Data Butler (§6.2.2), or both.

#### 3.1. Science Images

Science images are exposures of the night sky, as distinct from calibration images (§3.6.2). Although the release includes calibration images, allowing users to reprocess the raw images if needed, this is expected to be necessary only in rare cases. Users are strongly encouraged to start from the visit-level images provided. The data product names shown here are those used by the Data Butler, but the names used in the IVOA Services differ only slightly in that they are prepended by "1sst."

• raw images (NSF-DOE Vera C. Rubin Observatory 2025b) are unprocessed data received directly from the camera. Each raw corresponds to a single CCD from a single LSSTComCam exposure of 30 s duration. Each LSSTComCam exposure typically produces up to nine raws, one per sensor in the focal plane. However, a small number of exposures resulted in fewer than nine raw images due to temporary hardware issues or readout faults.

In total, DP1 includes 16125 raw images. Table 4 provides a summary by target and band. A raw contains  $4608 \times 4096$  pixels, including prescan and overscan, and occupies around 18 MB of disk space. The field of view of a single raw, excluding prescan and overscan regions, is roughly  $0^{\circ}23 \times 0^{\circ}22 \approx 0.051 \text{ deg}^2$ , corresponding to a plate scale of 0".2 per pixel.

visit\_images (NSF-DOE Vera C. Rubin Observatory 2025c) are fully-calibrated processed images. They have undergone instrument signature removal (§4.2.1) and all the single frame processing steps described in §4.2 which are, in summary: PSF modeling, background subtraction, and astrometric and photometric calibration. As with raws, a visit\_image contains processed data from a single CCD resulting from a single 30 s LSST-ComCam exposure. As a consequence, a single

**Table 4.** Number of raw images per field and band. Each raw image corresponds to a single 30-second LSSTComCam exposure on one CCD. Most exposures produce nine raw images, one per sensor in the focal plane, however some yield fewer due to occasional hardware or readout issues.

Field Code	Band						Total
-	u	g	r	i	z	$\overline{y}$	
47_Tuc	54	90	288	171	0	45	648
ECDFS	387	2070	2133	1455	1377	270	7692
$EDFS\_comcam$	180	549	783	378	378	180	2448
$Fornax\_dSph$	0	45	225	108	0	0	378
$Rubin\_SV\_095\25$	297	738	756	207	540	90	2628
$Rubin\_SV\_38\_7$	0	396	360	495	180	0	1431
Seagull	90	333	387	0	90	0	900
Total	1008	4221	4932	2814	2565	585	16125

LSSTComCam exposure typically results in nine visit\_images. The handful of exposures with fewer than nine raw images also have fewer than nine visit\_images, but there are an additional 153 raw that failed processing and for which there is thus no corresponding visit\_image. Almost all failures were due to challenges with astrometric fits or PSF models in crowded fields.

In total, there are 15972 visit\_images in DP1. Each visit\_image comprises three images: a calibrated science image, a variance image, and a pixel-level bitmask that flags issues such as saturation, cosmic rays, or other artifacts. Each visit\_image also contains a position-dependent PSF model, World Coordinate System (WCS) information, and various metadata providing information about the observation and processing. The science and variance images and the pixel mask each contain 4072 × 4000 pixels. In total, a single visit\_image, including all extensions and metadata, occupies around 110 MB of disk space.

deep\_coadds (NSF-DOE Vera C. Rubin Observatory 2025d) are the product of warping and coadding multiple visit\_images covering a given patch, as defined by the skymap. deep\_coadds are created on a per-band basis, meaning only data from exposures taken with a common filter are coadded. As such, there are up to six deep\_coadds covering each patch – one for each of the six LSSTComCam bands. The process of producing deep\_coadds is described in detail in §4.5 but, to summarize, it involves the selection of suitable

<sup>&</sup>lt;sup>87</sup> Each amplifier image contains 3 and 64 columns of serial prescan and overscan pixels, respectively, and 48 rows of parallel overscan pixels, meaning a raw contains 4072 ×4000 exposed pixels.

799

800

801

802

803

805

806

807

808

809

810

811

812

813

814

815

816

817

818

819

820

821

822

823

824

826

827

828

829

830

831

832

833

834

835

836

837

838

839

840

841

visit\_images (both in terms of patch coverage, band, and image quality), the warping of those visit\_images onto a common pixel grid, and the co-adding of the warped visit\_images. To be included in a DP1 deep\_coadd, a visit\_image needed to have a PSF FWHM smaller than 1".7. Of the 15972 visit\_images, 15375 satisfied this criterion and were therefore used to create deep\_-coadds.

844

845

846

848

849

850

851

852

853

856

857

861

862

865

869

870

871

872

873

875

876

877

878

879

880

881

882

883

887

888

There are a total of 2644 deep\_coadds in DP1. As mentioned above, a single deep\_coadd covers one patch, and includes a small amount of overlap with its neighboring patch. The skymap used for DP1 defines a patch as having an on-sky area of  $0.028 \text{ deg}^2$  excluding overlap, and  $0.036 \text{ deg}^2$ including overlap. A single deep\_coadd - including overlap – contains  $3400 \times 3400$  equal-sized pixels, corresponding to a platescale of 0".2 per pixel. Each deep\_coadd contains the science image (i.e., the coadd), a variance image, and a pixel mask; all three contain the same number of pixels. Each deep coadd also contains a positiondependent PSF model (which is the weighted sum of the PSF models of the input visit\_images), WCS information, plus various metadata.

Since coadds always cover an entire patch, it is common for a deep\_coadd to contain regions that were not covered by any of the selected visit\_images, particularly if the patch is on the outskirts of a field and was thus not fully observed. By the nature of how coadds are produced, such regions may contain seemingly valid flux values (i.e., not necessarily zeros or NaNs), but will instead be flagged with the NO\_DATA flag in the pixel mask. It is therefore crucial that the pixel mask be referred to when analyzing deep\_coadds.

• template\_coadds (NSF-DOE Vera C. Rubin Observatory 2025e) are those created to use as templates for difference imaging, i.e., the process of subtracting a template image from a visit\_image to identify either variable or transient objects. 88 As with deep\_coadds, template\_coadds are produced by warping and co-adding multiple visit\_images covering a given skymap-defined patch.

The process of building template\_coadds is the same as that for deep coadds, but the selection criteria differ between the two types of coadd. In the case of template\_coadds, one third of visit images covering the patch in question with the narrowest PSF FWHM are selected. If one third corresponds to fewer than twelve visit images (i.e., there are fewer than 36 visit\_images covering the patch), then the twelve visit\_images with the narrowest PSF FWHM are selected. Finally, if there are fewer than twelve visit\_images covering the patch, then all visit images are selected. Of the 15972 visit\_images, 13113 were used to create template\_coadds. This selection strategy is designed to optimize for seeing when a patch is well-covered by visit\_images, yet still enable the production of template coadds for poorly-covered patches.

DP1 contains a total of 2730 template\_coadds.<sup>89</sup> As with deep\_coadds, a single template\_coadd covers a single patch. Since the same skymap is used when creating both deep\_coadd and template\_coadds, the on-sky area and pixel count of template\_coadds are the same as that of a deep\_coadd (see above). Similarly, template\_coadds contain the science image (i.e., the coadd), a variance image, and a pixel mask; all three contain the same number of pixels. Also included are the PSF model, WCS information, and metadata. As is the case for deep\_coadd, those pixels within template coadds that are not covered by any of the selected visit\_images may still have seemingly valid values, but are indicated with the NO\_DATA flag within the pixel mask.

• difference\_images (NSF-DOE Vera C. Rubin Observatory 2025f) are generated by the subtraction of the warped, scaled, and PSF-matched template\_coadd from the visit\_image (see §4.6.1). In principle, only those sources whose flux has changed relative to the template\_coadd should be apparent (at a significant level) within a difference\_image. In practice, however, there are numerous spurious sources present in difference\_images due to unavoidably imperfect template matching.

In total, there are 15972 difference\_images in DP1, one for each visit\_image.

<sup>88</sup> It should be noted that template\_coadds are not themselves subtracted from visit\_images but are, instead, warped to match the WCS of a visit\_image. It is this warped template that is subtracted from the visit\_image to create a difference image. For storage space reasons, warped templates are not retained for DP1, as they can be readily and reliably recreated from the template\_coadds.

<sup>89</sup> The difference in the number of deep\_coadds and template\_coadds is due to the difference in the visit\_image selection criteria for each coadd.

Like visit\_images, difference\_images contain the science (i.e., difference) image, a variance image, and a pixel mask; all three contain the same number of pixels, which is the same as that of the input visit\_image. Also included is the PSF model, WCS information, and metadata.

• Background images contain the model background that has been generated and removed from a science image. visit\_images, deep\_coadds and template\_coadds all have associated background images. Background images contain the same number of pixels as their respective science image, and there is one background image for each visit\_image, deep\_coadd, and template\_coadd. Difference imaging analysis also measures and subtracts a background model, but the difference\_background data product is not written out by default and is not part of DP1.

Background images are not available via the IVOA Service; they can only be accessed via the Butler Data Service.

#### 3.2. Catalogs

Here we describe science-ready tables produced by the science pipelines. All but one of the catalogs described here contain data for detections in the images described in section 3.1, the exception being the Calibration catalog, which contains reference data obtained from previous surveys. Observatory-produced metadata tables are described in §3.5 Each type of catalog contains measurements for either Sources detected in visit\_images and difference\_images, or Objects detected in deep\_-coadds.

While the Source, <code>Object</code>, <code>ForcedSource</code>, <code>Dia-Source</code>, <code>DiaObject</code>, and <code>ForcedSourceOnDiaObject</code> catalogs described below each differ in terms of their specific columns, in general they each contain: one or more unique identification numbers, positional information, one or more types of flux measurements (e.g., aperture fluxes, <code>PSF</code> fluxes, Gaussian fluxes, etc.), and a series of boolean flags (indicating, for example, whether the source/object is affected by saturated pixels, cosmic rays, etc.) for each source/object. The Solar System catalogs <code>SSObject</code> and <code>SSSource</code> deviate from this general structure in that they instead contain orbital parameters for all known asteroids. Where applicable, all measured properties are reported with their associated  $1\sigma$  uncertainties.

Since DP1 is a preview, it doesn't include all the catalogs expected in a full LSST Data Release. Additionally, the catalogs it does include may be missing some columns planned for future releases. Where this is the case, we note what data are missing in the catalog descriptions that follow.

Catalog data are stored in the Qserv database (§6.5.1) and are accessible via Table Access Protocol (IVOA standard) (IVOA), and an online DP1 catalog schema is available at https://sdm-schemas.lsst.io/dp1.html. Catalog data are also accessible via the Data Butler (§6.2.2).

• The Source catalog (NSF-DOE Vera C. Rubin Observatory 2025g) contains data on all sources which are, prior to deblending (§4.5.2), detected with a greater than 5σ significance in each individual visit. The detections reported in the Source catalog have undergone deblending; in the case of blended detections, only the deblended sources are included in the Source catalog. It is important to note that while the criterion for inclusion in a Source catalog is a > 5σ detection in a visit\_image prior to deblending, the positions and fluxes are reported post-deblending. Hence, it is possible for the Source catalog to contain sources whose flux-to-error ratios – potentially of all types (i.e., aperture flux, PSF flux, etc.) – are less than 5.

In addition to the general information mentioned above (i.e., IDs, positions, fluxes, flags), the Source catalog also includes basic shape and extendedness information.

The Source catalog contains data for 46 million sources in DP1.

• The Object catalog (NSF-DOE Vera C. Rubin Observatory 2025h) contains data on all objects detected with a greater than  $5\sigma$  significance in the deep coadds. With coadd images produced on a per-band basis, a  $> 5\sigma$  detection in one or more of the bands will result in an object being included in the Object catalog. For cases where an object is detected at  $> 5\sigma$  in more than one band, a crossmatching has been performed between bands to associate an object in one band with its counterpart(s) in the other bands. As such, unlike the Source catalog, the Object catalog contains data from multiple bands. The objects reported in the Object catalog have also undergone deblending; in the case of blended detections, only the deblended child objects are included in the catalog. As with the Source catalog, the criterion for inclusion in

<sup>90</sup> In future data releases, background images may be included as part of their respective science image data product.

the Object catalog is a  $> 5\sigma$  detection in one of the deep\_coadds prior to deblending, yet the positions and fluxes of objects are reported post-deblending. Hence, it is possible for Object catalog to contain objects whose flux-to-error ratios — potentially of all types and in all bands — are less than 5.

In addition to the general information mentioned above (i.e., IDs, positions, fluxes, flags), the Object catalog also includes basic shape and extendedness information. While they may be included in future data releases, no photometric redshifts, Petrosian magnitudes (V. Petrosian 1976), proper motions or periodicity information are included in the DP1 object catalogs.

The Object catalog contains data for 2.3 million objects in DP1.

• The ForcedSource catalog (NSF-DOE Vera C. Rubin Observatory 2025i) contains forced PSF photometry measurements performed on both difference\_images (i.e., the psfDiffFlux column) and visit\_images (i.e., the psfFlux column) at the positions of all the objects in the Object catalog, to allow assessment of the time variability of the fluxes. We recommend using the psfDiffFlux column when generating light curves because this quantity is less sensitive to flux from neighboring sources than psfFlux. In addition to forced photometry PSF fluxes, a number of boolean flags are also included in the Forced-Source catalog.

The ForcedSource catalog contains a total of 269 million entries across 2.3 million unique objects.

• The DiaSource catalogs (NSF-DOE Vera C. Rubin Observatory 2025j) contains data on all the sources detected at a > 5σ significance — including those associated with known Solar System objects — in the difference\_images. Unlike sources detected in visit\_images, sources detected in difference images (hereafter, "DiaSources") have gone through an association step in which an attempt has been made to associate them into underlying objects called "DiaObject"s. The DiaSource catalog consolidates all this information across multiple visits and bands. The detections reported in the DiaSource catalog have not undergone deblending.

The DiaSource catalog contains data for 3.1 million DiaSources in DP1.

• The DiaObject catalog (NSF-DOE Vera C. Rubin Observatory 2025k) contains the astrophysical objects that DiaSources are associated with (i.e., the "DiaObjects"). The DiaObject catalog contains only non-Solar System Objects; Solar System Objects are, instead, recorded in the SSObject catalog. When a DiaSource is identified, the DiaObject and SSObject catalogs are searched for objects to associate it with. If no association is found, a new DiaObject is created and the DiaSource is associated to it. Along similar lines, an attempt has been made to associate DiaObjects across multiple bands, meaning the DiaObject catalog, like the Object catalog, contains data from multiple bands. Since DiaObjects are typically transient or variable (by the nature of their means of detection), the DiaObject catalog contains summary statistics of their fluxes, such as the mean and standard deviation over multiple epochs; users must refer to the ForcedSourceOnDiaObject catalog (see below) or the DiaSource catalog for single epoch flux measurements of DiaObjects.

The DIAObject catalog contains data for 1.1 million DiaObjects in DP1.

• The ForcedSourceOnDiaObject catalog (NSF-DOE Vera C. Rubin Observatory 20251) is equivalent to the ForcedSource catalog, but contains forced photometry measurements obtained at the positions of all the DiaObjects in the DiaObject catalog.

The ForcedSourceOnDiaObject catalog contains a total of 197 million entries across 1.1 million unique DiaObjects.

• The CcdVisit catalog (NSF-DOE Vera C. Rubin Observatory 2025m) contains data for each individual processed visit\_image. In addition to technical information, such as the on-sky coordinates of the central pixel and measured pixel scale, the CcdVisit catalog contains a range of data quality measurements, such as whole-image summary statistics for the PSF size, zeropoint, sky background, sky noise, and quality of astrometric solution. It provides an efficient method to access visit\_image properties without needing to access the image data.

The CcdVisit catalog contains entries summarizing data for all 16071 visit\_images.

• The SSObject catalog (NSF-DOE Vera C. Rubin Observatory 2025n), Minor Planet Center Orbit

database (MPCORB) and SSObject, carry information about solar system objects. The MPCORB table provides the Minor Planet Center-computed orbital elements for all known asteroids, including those that Rubin discovered. For DP1, the SSObject catalog serves primarily to provide the mapping between the International Astronomical Union (IAU) designation of an object (listed in MPCORB), and the internal ssObjectId identifier, which is used as a key to find solar system object observations in the DiaSource and SSSource tables.

The SSSource catalog (NSF-DOE Vera C. Rubin Observatory 2025o) contains data on all Dia-Sources that are either associated with previously-known Solar System Objects, or have been confirmed as newly-discovered Solar System Objects by confirmation of their orbital properties. As entries in the SSSource catalog stem from the DiaSource catalog, they have all been detected at > 5σ significance in at least one band. The SS-Source catalog contains data for 5988 Solar System Sources.

• The Calibration catalog is the reference catalog that was used to perform astrometric and photometric calibration. It is a whole-sky catalog built specifically for LSST, as no single prior reference catalog had both the depth and coverage needed to calibrate LSST data. It combines data from multiple previous reference catalogs and contains only stellar sources. Full details on how the Calibration catalog was built are provided in P. S. Ferguson et al. (2025) <sup>91</sup>. We provide a brief summary here.

For the grizy bands, the input catalogs were (in order of decreasing priority): Dark Energy Survey (DES) Y6 Calibration Stars (E. S. Rykoff et al. 2023); Gaia-B or R Photometry (Gaia) (XP) Synthetic Magnitudes (Gaia Collaboration et al. 2023a); the Panoramic Survey Telescope and Rapid Response System (Pan-STARRS)1 3PI Survey (K. C. Chambers et al. 2016); Data Release 2 of the SkyMapper survey (C. A. Onken et al. 2019); and Data Release 4 of the VLT Survey Telescope (VST) Asteroid Terrestrial-impact Last Alert System (ATLAS) survey (T. Shanks et al. 2015). For the u-band, the input catalogs

were (in order of decreasing priority): Standard Stars from Sloan Digital Sky Survey (SDSS) Data Release 16 (R. Ahumada et al. 2020); Gaia-XP Synthetic Magnitudes (Gaia Collaboration et al. 2023a); and synthetic magnitudes generated using Single Lens Reflex (SLR), which estimates the *u*-band flux from the *g*-band flux and *g-r* colors. This SLR estimates were used to boost the number of *u*-band reference sources, as otherwise the source density from the *u*-band input catalogs is too low to be useful for the LSST.

Only stellar sources were selected from each input catalog. Throughout, the Calibration catalog uses the DES bandpasses for the grizy bands and the SDSS bandpass for the u-band; color transformations derived from high quality sources were used to convert fluxes from the various input catalogs (some of which did not use the DES/SDSS bandpasses) to the respective bandpasses. All sources from the input catalogs are matched to Gaia-Data Release 3 (DR3) sources for robust astrometric information, selecting only isolated sources (i.e., no neighbors within 1").

After collating the input catalogs and transforming the fluxes to the standard DES/SDSS bandpasses, the catalog was used to identify sources within a specific region of the sky. This process generated a set of standard columns containing positional and flux information, along with their associated uncertainties.

#### 3.2.1. Source and Object Designations

To refer to individual sources or objects from the DP1 catalogs, one should follow the LSST DP1 naming convention that has been registered with the International Astronomical Union. Because the Source, Object, DiaSource, DiaObject, and SSObject tables each have their own unique IDs, their designations should differ. In general, source designations should begin with the string "LSST-DP1" (denoting the Legacy Survey of Space and Time, Data Preview 1), followed by a string specifying the table from which the source was obtained. These strings should be "O" (for the Object table), "S" (Source), "DO" (DiaObject), "DS" (DiaSource), or "SSO" (SSObject). Following the table identifier, the designation should contain the full unique numeric identifier from the specified table (i.e., the objectId, sourceId, diaObjectId, diaSourceId, or ssObjectId). Each component of the identifier should be separated by dashes, resulting in a designation such as "LSST-DP1-TAB-123456789012345678". In summary,

<sup>&</sup>lt;sup>91</sup> In P. S. Ferguson et al. (2025), the calibration reference catalog is referred to as "The Monster". This terminology is also carried over to the DP1 Butler.

source designations should adhere to the formats listed below: 1229

 Object: LSST-DP1-O-609788942606161356 (for objectId 609788942606161356) 

- Source: LSST-DP1-S-600408134082103129 (for sourceId 600408134082103129)
- DiaObject: LSST-DP1-DO-609788942606140532 (for diaObjectId 609788942606140532)
- DiaSource: LSST-DP1-DS-600359758253260853 (for diaSourceId 600359758253260853)
- SSObject: LSST-DP1-SSO-21163611375481943 (for ssObjectId 21163611375481943)

Tables that were not explicitly mentioned in the description above do not have their own unique IDs, but are instead linked to one of the five tables listed above via a unique ID. For example, the ForcedSource table is keyed on objectId, ForcedSourceOnDiaObject uses diaObjectId, SSSource is linked to diaSourceId and ssObjectId, and MPCORB uses ssObjectId.

#### 3.3. Survey Property Maps

Maps are two-dimensional visualizations of survey In DP1, these fall into two categories: Survey Property Maps and Hierarchical Progressive Survev (HiPS) Maps (P. Fernique et al. 2015). Survey Property Maps (NSF-DOE Vera C. Rubin Observatory 2025p) summarize how properties such as observing conditions or exposure time vary across the observed sky. Each map provides the spatial distribution of a specific quantity at a defined sky position for each band by aggregating information from the images used to make the deep\_coadd. Maps are initially created pertract and then combined to produce a final consolidated map. At each sky location, represented by a spatial pixel in the Hierarchical Equal-Area iso-Latitude Pixelisation (HEALPix)(K. M. Górski et al. 2005) grid, values are derived using statistical operations, such as minimum, maximum, mean, weighted mean, or sum, depending on the property.

DP1 contains 14 survey property maps. The available maps describe total exposure times, observation epochs, PSF size and shape, PSF magnitude limits, sky background and noise levels, as well as astrometric shifts and PSF distortions due to wavelength-dependent atmospheric Differential Chromatic Refraction (DCR) effects. They all use the dataset type format deep\_coadd\_<PROPERTY>\_consolidated\_map\_-<STATISTIC>. For example, deep\_coadd\_exposure\_-time\_consolidated\_map\_sum provides a spatial map of

the total exposure time accumulated per sky position in units of seconds. All maps are stored in HealSparse<sup>92</sup> format. Survey property maps are only available via the Data Butler (§6.2.2) and have dimensions band and skymap.

Figure 8 presents three survey property maps for exposure time, PSF magnitude limit, and sky noise, computed for representative tracts and bands. Because full consolidated maps cover widely separated tracts, we use clipped per-tract views here to make the spatial patterns more discernible. Many more survey property maps are available in the DP1 repository.

#### 3.4. HiPS Maps

HiPS Maps (P. Fernique et al. 2015), offer an interactive way to explore seamless, multi-band tiles of the sky regions covered by DP1, allowing for smooth panning and zooming. DP1 provides multi-band HiPS images created by combining data from individual bands of deep\_coadd and template\_coadd images. These images are false-color representations generated using various filter combinations for the red, green, and blue channels. The available filter combinations include gri, izy, riz, and ugr for both deep\_coadd and template\_coadd. Additionally, for deep\_coadd only, we provide color blends such as uug and grz. Post-DP1, we plan to also provide single-band HiPS images for all ugrizy bands in both Portable Network Graphics (PNG) and Flexible Image Transport System (FITS) formats.

HiPS maps are only accessible through the HiPS viewer in the Rubin Science Platform (RSP) Portal (§6.3) and cannot be accessed via the Data Butler (§6.2.2). All multi-band HiPS images are provided in PNG format.

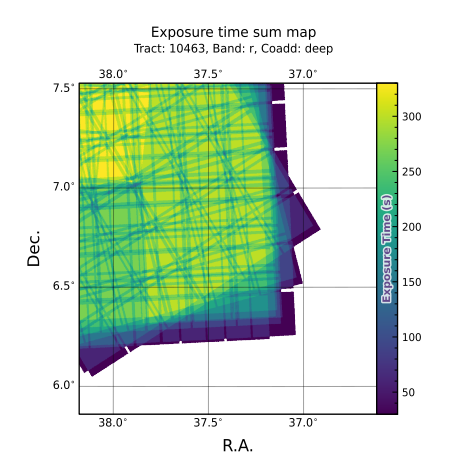
#### $3.5.\ Metadata$

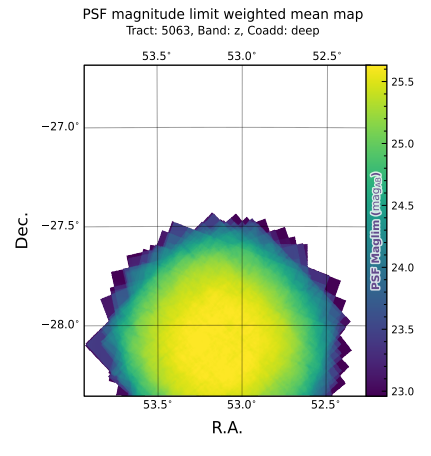
DP1 also includes metadata about the observations, which are stored in the Visit table. The data it contains was produced by the observatory directly, rather than the science pipelines. It contains technical data for each visit, such as telescope pointing, camera rotation, airmass, exposure start and end time, and total exposure time.

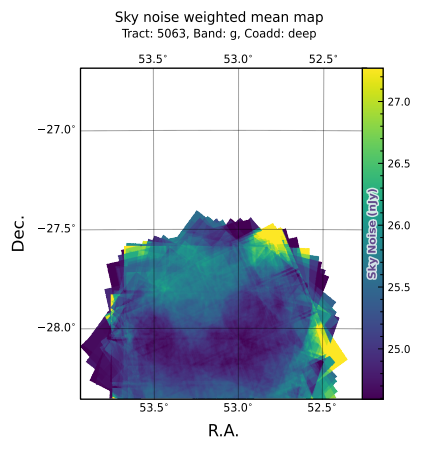
#### 3.6. Ancillary Data Products

DP1 also includes several ancillary data products. While we do not expect most users to need these, we describe them here for completeness. All the Data Prod-

<sup>&</sup>lt;sup>92</sup> A sparse HEALPix representation that efficiently encodes data values on the celestial sphere. https://healsparse.readthedocs.







(a) Exposure time sum map for deep\_coadd tract 10463, r-band in field Rubin\_SV\_38\_7

1276

1277

1278

1279

1280

1282

1283

1284

1285

1286

1287

1288

1289

1291

1292

1293

1295

1296

1298

1299

1300

1301

1302

1303

(b)  $5\sigma$  PSF magnitude limit weighted mean map for deep\_coadd tract 5063, z-band in field ECDFS

(c) Sky noise weighted mean map for deep\_coadd tract 5063, z-band in field ECDFS

Figure 8. Examples of survey property maps from Rubin DP1 across different bands, clipped to the boundary of a single tract for visual clarity.

1314

1315

1316

1317

1325

ucts described in this section can only be accessed via the Data Butler (§6.2.2).

#### 3.6.1. Task configuration, log, and metadata

DP1 includes provenance-related data products such as task logs, configuration files, and task metadata. Configuration files record the parameters used in each processing task, while logs and metadata contain information output during processing. These products help users understand the processing setup and investigate potential processing failures.

### 3.6.2. Calibration Data Products

Calibration data products include a variety of images and models that are used to characterize and correct the performance of the camera and other system components. These include bias, dark, and flat-field images, Photon Transfer Curve (PTC) gains, brighter-fatter kernels (P. Antilogus et al. 2014), charge transfer inefficiency (CTI) models, linearizers, and illumination corrections. For flat-field corrections, DP1 processing used combined flats, which are averaged from multiple individual flat-field exposures to provide a stable calibration. These calibration products are essential inputs to Instrument Signal Removal (ISR) (§4.2.1). these products are included in DP1 for transparency and completeness, users should not need to rerun ISR for their science and are advised to start with the processed visit\_image.

#### 4. DATA RELEASE PROCESSING

Data Release Processing (DRP) is the systematic processing of all Rubin Observatory data collected up to

a certain date to produce the calibrated images, catalogs of detections, and derived data products described in Section 3. DP1 was processed entirely at the United States Data Facility (USDF) at SLAC using 17,024 CPU hours.  $^{93}$ 

This section describes the pipeline algorithms used to produce DP1 and how they differ from those planned for full-scale LSST data releases. Data Release Production consists of four major stages: (1) single-frame processing, (2) calibration, (3) coaddition, and (4) difference image analysis (DIA).

#### 4.1. LSST Science Pipelines Software

The LSST Science Pipelines software (Rubin Observatory Science Pipelines Developers 2025; J. Swinbank et al. 2020) will be used to generate all Rubin Observatory and LSST data products. It provides both the algorithms and middleware frameworks necessary to process raw data into science-ready products, enabling analysis by the Rubin scientific community. Version v29.1 of the pipelines was used to produce DP1<sup>94</sup>.

### 4.2. Single Frame Processing

#### 4.2.1. Instrument Signature Removal

The first step in processing LSSTComCam images is to correct for the effects introduced by the telescope and detector. Each sensor and its readout amplifiers can

<sup>93</sup> For future Data Releases, data processing will be distributed across the USDF, the French (FrDF)and UK (UKDF) data facilities.

 $<sup>^{94}</sup>$  Documentation for this version is available at: https://pipelines.lsst.io/v/v29  $\,1\,$  1

1331

1332

1333

1334

1335

1337

1338

1339

1340

1341

1342

1344

1345

1347

1348

1349

1351

1352

1353

1354

1355

1356

1357

1358

1359

1360

1362

1363

1365

1366

1367

1368

1369

1370

1371

1372

vary slightly in performance, causing images of even a 1374 uniformly illuminated focal plane to exhibit discontinuities and shifts due to detector effects. The ISR pipeline aims to recover the original astrophysical signal as best as possible and produce science-ready single-epoch images for source detection and measurement. A detailed description of the ISR procedures can be found in P. Fagrelius & E. S. Rykoff (2025); A. A. Plazas Malagón et al. (2025). Figure 9 illustrates the model of detector components and readout electronics and their impact on the signal, tracing the process from photons incident on the detector surface to the final quantized values<sup>95</sup> recorded in the image files. The ISR pipeline essentially "works backward" through the signal chain, correcting the integer analog-to-digital units (ADU) raw camera output back to a floating-point number of photoelectrons created in the silicon. The physical detector, shown on the left in Figure 9, is the source of effects that arise from the silicon itself, such as the dark current and the brighterfatter effect (A. A. Plazas et al. 2018; A. Broughton et al. 2024). After the integration time has elapsed, the charge is shifted to the serial register and read out, which can introduce charge transfer inefficiencies and a clockinjected offset level. The signals for all amplifiers are transferred via cables to the Readout Electronics Board (REB), during which crosstalk between the amplifiers may occur. The Analog Signal Processing Integrated Circuit (ASPIC) on the REB converts the analog signal from the detector into a digital signal, adding both quantization and a bias level to the image. Although the signal chain is designed to be stable and linear, the presence of numerous sources of non-linearity indicates otherwise.

The ISR processing pipeline for DP1 performs, in the following order: Analogue-to-Digital Unit (ADU) dithering to reduce quantization effects, serial overscan subtraction, saturation masking, gain normalization, crosstalk correction, parallel overscan subtraction, linearity correction, serial CTI correction, image assembly, bias subtraction, dark subtraction, brighter-fatter correction, defect masking and interpolation, variance plane construction, flat fielding, and amplifier offset (amp-offset) correction<sup>96</sup>. Flat fielding for DP1 was performed using combined flats produced from twilight flats

acquired with sufficient rotational dithering to mitigate artifacts from print-through stars, as described in §2.3.

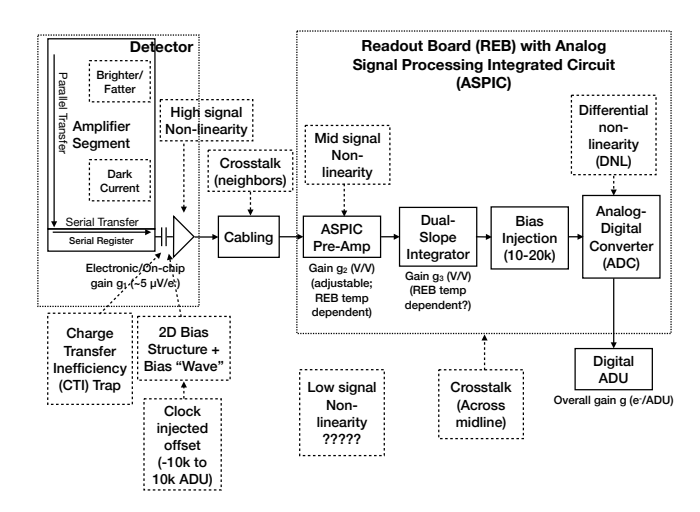


Figure 9. The model of the detector and REB components, labeled with the effects that they impart on signal.

#### 4.2.2. Background Subtraction

1377

1378

1382

1383

1396

1403

The background subtraction algorithms in the LSST Science Pipelines estimate and remove large-scale background signals from science imaging. Such signals may include sky brightness from airglow, moonlight, scattered light instrumental effects, zodiacal light, and diffuse astrophysical emission. In so doing, true astrophysical sources are isolated to allow for accurate detection and measurement.

To generate a background model, each post-ISR image is divided into superpixels of  $128 \times 128$  pixels. Pixels with a mask flag set that indicates that they contain no useful science data or that they contain flux from a preliminary source detection are masked. The iterative  $3\sigma$  clipped mean of the remaining pixels is calculated for each superpixel, constructing a background statistics image. A sixth-order Chebyshev polynomial is fit to these values on the scale of a single detector to allow for an extrapolation back to the native pixel resolution of the post-ISR image.

#### 4.3. Calibration

Stars are detected in each post-ISR image using a  $5\sigma$ threshold. Detections of the same star across multiple images are then associated to identify a consistent set of isolated stars with repeated observations suitable for use in PSF modeling, photometric calibration, and astrometric calibration.

Initial astrometric and photometric solutions are derived using only the calibration reference catalogs (see §3.2), and an initial PSF model is fit using PSFEx (E.

 $<sup>^{95}</sup>$  The images written to disk by the camera have values that are integers that come from the ADC converting an analog voltage.  $^{96}$  Amp-offset corrections are designed to address systematic discontinuities in background sky levels across amplifier boundaries. The implementation in the LSST Science Pipelines is based on the Pan-STARRS Pattern Continuity algorithm (C. Z. Waters et al. 2020).

1463

1464

1465

1471

1474

1475

1476

1482

1488

1499

Bertin 2011). These preliminary solutions provide approximate source positions, fluxes, and PSF shapes that serve as essential inputs to the calibration process, enabling reliable source matching, selection of high-quality stars, and iterative refinement of the final astrometric, photometric, and PSF models. These preliminary solutions are subsequently replaced by more accurate fits, as described in the following sections.

1406

1407

1409

1410

1411

1413

1414

1415

1416

1417

1418

1419

1420

1421

1422

1423

1425

1426

1427

1428

1429

1430

1431

1432

1433

1434

1436

1437

1438

1439

1440

1441

1442

1443

1444

1445

1447

1448

1450

1451

1452

1453

1454

1455

1456

#### 4.3.1. PSF Modeling

PSF modeling in DP1 uses the Piff (M. Jarvis et al. 2021) package. Our configuration of Piff utilizes its PixelGrid model with a fourth-order polynomial interpolation per CCD, except in the u-band, where star counts are insufficient to support a fourth-order fit. In this case, a second-order polynomial is used instead. Details on the choice of polynomial order, overall PSF modeling performance, and known issues are discussed in  $\S 5.2$ .

#### 4.3.2. Astrometric Calibration

Starting from the astrometric solution calculated in single frame processing (§4.2), the final astrometric solution is computed using the ensemble of visits in a given band that overlap a given tract. This allows the astrometric solution to be further refined by using all of the isolated point sources of sufficient signal-to-noise ratio in an image, rather than only those that appear in the reference catalog, as is done in single frame processing. Using multiple whole visits rather than a single detector also allows us to account for effects that impact the full focal plane, and for the proper motion and parallax of the sources.

In order to perform the fit of the astrometric solution, isolated point sources are associated between overlapping visits and with the Gaia DR3 (Gaia Collaboration et al. 2023b) reference catalog where possible. The model used for DP1 consists of a static map from pixel space to an intermediate frame (the per-detector model), followed by a per-visit map from the intermediate frame to the plane tangent to the telescope boresight (the per-visit model), then finally a deterministic mapping from the tangent plane to the sky. The fit is done using the gbdes package (G. M. Bernstein et al. 2017), and a full description is given in C. Saunders (2024).

The per-detector model is intended to capture quasistatic characteristics of the telescope and camera. During Rubin Operations, the astrometric solution will allow for separate epochs with different per-detector models, to account for changes in the camera due to warming and cooling and other discrete events. However, for DP1, LSSTComCam was assumed to be stable enough that all visits use the same per-detector model. The model itself is a separate two-dimensional polynomial for each detector. For DP1, a degree 4 polynomial was used; the degree of the polynomial mapping is tuned for each instrument and may be different for LSSTCam. Further improvements may be made by including a pixel-based astrometric offset mapping, which would be fit from the ensemble of astrometric residuals, but this is not included in the DP1 processing.

The per-visit model attempts to account for the path of a photon from both atmospheric sources and those dependent on the telescope orientation. This model is also a polynomial mapping, in this case a degree 6 two-dimensional polynomial. Correction for DCR (§5.4) was not done for DP1, but will be included in LSSTCam processing during Rubin Operations. Future processing will also likely include a Gaussian Process fit to better account for atmospheric turbulence, as was demonstrated by W. F. Fortino et al. (2021) and P. F. Léget et al. (2021).

The final component of the astrometric calibration involves the positions of the isolated point sources included in the fit, which are described by five parameters: sky coordinates, proper motion, and parallax. While proper motions and parallaxes are not released for DP1, they are fitted for these sources in the astrometric solution to improve the astrometric calibration.

#### 4.3.3. Photometric Calibration

Photometric calibration of the DP1 dataset is based on the Forward Global Calibration Method (FGCM) (FGCM D. L. Burke et al. 2018), adapted for the LSST Science Pipelines (H. Aihara et al. 2022; P. Fagrelius & E. S. Rykoff 2025). We used the FGCM to calibrate the full DP1 dataset with a forward model that uses a parameterized model of the atmosphere as a function of airmass along with a model of the instrument throughput as a function of wavelength. The FGCM process typically begins with measurements of the instrumental throughput, including the mirrors, filters, and detectors. However, because full scans of the LSSTComCam asbuilt filters and individual detectors were not available, we instead used the nominal reference throughputs for the Simonyi Survey Telescope and LSSTCam.<sup>97</sup> These nominal throughputs were sufficient for the DP1 calibration, given the small and homogeneous focal plane consisting of only nine ITL detectors. The FGCM atmosphere model, provided by MODTRAN (A. Berk et al. 1999), was used to generate a look-up table for atmospheric throughput as a function of zenith distance at Cerro Pachón. This model accounts for absorption and scattering by molecular constituents of the atmosphere,

<sup>97</sup> Available at: https://github.com/lsst/throughputs/tree/1.9

1507

1508

1509

1510

1511

1513

1514

1515

1516

1517

1518

1519

1520

1521

1522

1523

1524

1525

1526

1527

1528

1529

1530

1531

1532

1533

1534

1535

1536

1537

1538

1539

1540

1541

1542

1543

1544

1545

1546

1547

1549

1550

1551

1552

1553

1554

1555

including  $O_2$  and  $O_3$ ; absorption by water vapor; and 1556 Mie scattering by airborne aerosol particulates. Nightly variations in the atmosphere are modeled by minimizing the variance in repeated observations of stars with a Signal to Noise Ratio (SNR) greater than 10, measured using "compensated aperture fluxes". These fluxes include a local background subtraction (see §4.2.2) to mitigate the impact of background offsets. The model fitting process incorporates all six bands (ugrizy) but does not include any gray (achromatic) terms, except for a linear assumption of mirror reflectance degradation, which is minimal over the short duration of the DP1 observation campaign. As an additional constraint on the fit, we use a subset of stars from the reference catalog (P. S. Ferguson et al. 2025), primarily to constrain the system's overall throughput and establish the "absolute" calibration.

#### 4.4. Visit Images and Source Catalogs

With the final PSF models, WCS solutions, and photometric calibrations in place, we reprocess each singleepoch image to produce a final set of calibrated visit images and source catalogs. Source detection is performed down to a  $5\sigma$  threshold using the updated PSF models, followed by measurement of PSF and aperture fluxes. These catalogs represent the best single-epoch source characterization, but they are not intended for constructing light curves. For time-domain analysis, we recommend using the forced photometry tables described in §4.6.2.

## 4.5. Coaddition Processing 4.5.1. Coaddition

Only exposures with a seeing better than 1.7 arcseconds FWHM are included in the deep coadded images. For the template coadds, typically only the top third of visits with the best seeing are used (although see §3.1 for more details), resulting in an even tighter image quality cutoff for the template coadds. Exposures with poor PSF model quality, identified using internal diagnostics, are excluded to prevent contamination of the coadds with unreliable PSF estimates. The remaining exposures are combined using an inverse-variance weighted mean stacking algorithm.

To mitigate transient artifacts before coaddition, we apply the artifact rejection procedure described in Y. Al-Sayyad (2018) that identifies and masks features such as satellite trails, optical ghosts, and cosmic rays. It operates on a time series of PSF-matched images resampled onto a common pixel grid ("warps") and leverages their temporal behavior to distinguish persistent astrophysical sources from transient artifacts.

Artifact rejection uses both direct (where no PSFmatching is performed) and PSF-matched warps, homogenized to a standard PSF of 1.8 arcseconds FWHM, broadly consistent with the 1.7 arcsecond FWHM seeing threshold used in data screening. A sigma-clipped mean of the PSF-matched warps serves as a static sky model, against which individual warps are differenced to identify significant positive and negative residuals. Candidate artifact regions are classified as transient if they appear in less than a small percentage of the total number of exposures, with the threshold based on the number of visits, N, as follows:

- N=1 or 2: threshold = 0 (no clipping).
- N=3 or 4: threshold = 1.
- N=5: threshold = 2.

1570

1571

1575

1579

1583

1584

1596

• N > 5: threshold = 2 + 0.03N.

Identified transient regions are masked before coaddition, improving image quality and reducing contamination in derived catalogs.

#### 4.5.2. Detection, Deblending and Measurement

After constructing coadded images, sources are detected in each band, merged across bands, deblended, and measured to generate the final object catalogs For each coadd in all six bands, we perform source detection at a  $5\sigma$  detection threshold and then adjust the background with a per-patch constant (coadds are built from background-subtracted images, but the deeper detection on coadds redefines what is considered source versus background). Detections across bands are merged in a fixed priority order, *irzygu*, to form a union detection catalog, which serves as input to deblending.

Deblending is performed using the Scarlet Lite algorithm, which implements the same model as Scarlet (P. Melchior et al. 2018), but operates on a single pixel grid. This allows the use of analytic gradients, resulting in greater computational speed and memory efficiency.

Object measurement is then performed on the deblended detection footprints in each band. Measurements are conducted in three modes: independent perband measurements, forced measurements in each band, and multiband measurements.

Most measurement algorithms operate through a single-band plugin system, largely as originally described in J. Bosch et al. (2018). The same plugins are run separately for each object on a deblended image. which uses the Scarlet model as a template to re-weight the original noisy coadded pixel values. This effectively

preserves the original image in regions where objects are not blended, while dampening the noise elsewhere.

1604

1605

1606

1607

1608

1609

1611

1612

1613

1614

1615

1616

1617

1618

1619

1620

1621

1622

1623

1625

1626

1627

1628

1629

1630

1631

1632

1633

1634

1635

1636

1637

1639

1640

1641

1642

1643

1644

1645

1646

1647

1648

1650

1651

1652

1653

1654

A reference band is chosen for each object based on detection significance and measurement quality using the same priority order as detection merging (irzygu) and a second round of measurements is performed in forced mode using the shape and position from the reference band to ensure consistent colors (J. Bosch et al. 2018).

Measurement algorithm outputs include object fluxes, centroids, and higher-order moments thereof like sizes and shapes. A variety of flux measurements are provided, from aperture fluxes and forward modeling algorithms.

1666

1660

1700

1701

1702

Composite model (CModel) magnitudes (K. Abazajian et al. 2004; J. Bosch et al. 2018) are used to calculate the extendedness parameter, which functions as a star-galaxy classifier. Extendedness is a binary classifier that is set to 1 if the PSF model flux is less than 98.5% of the (free, not forced) CModel flux in a given band. Additionally, the extendedness in the reference band is provided as a separate column for convenience as a multiband star-galaxy classification, and is recommended generally but also specifically for objects with low signal-to-noise ratio in some bands.

Gaussian-Aperture-and-PSF (Gaussian Aperture and PSF (GAaP) K. Kuijken 2008; A. Kannawadi 2025) fluxes are provided to ensure consistent galaxy colors across bands. Sérsic model (J. L. Sérsic 1963; J. L. Sersic 1968) fits are run on all available bands simultaneously (MultiProFit, D. S. Taranu 2025). The resulting Sérsic model fluxes are provided as an alternative to CModel and are intended to represent total galaxy fluxes. Like CModel, the Sérsic model is a Gaussian mixture approximation to a true Sérsic profile, convolved with a Gaussian mixture approximation to the PSF. CModel measurements use a double "shapelet" (A. Refregier 2003) PSF with a single shared shape, while the Sérsic fits use a double Gaussian with independent shape parameters for each component. Sérsic model fits also include a free centroid, with all other structural parameters shared across all bands. That is, the intrinsic model has no color gradients, but the convolved model may have color gradients if the PSF parameters vary significantly be-

Further details on the performance of these algorithms are found in §5.7.

4.6. Variability Measurement

4.6.1. Difference Imaging Analysis

Difference Image Analysis (DIA) uses the decorrelated Alard & Lupton image differencing algorithm (D. J. Reiss & R. H. Lupton 2016). We detected both positive and negative DIASources at  $5\sigma$  in the difference image. Sources with footprints containing both positive and negative peaks due to offsets from the template position or blending were fit with a dipole centroid code, , which simultaneously fits offset positive and negative PSFs.

We filter a subset of DIASources that have pixel flags characteristic of artifacts, non-astrophysical trail lengths, and unphysically negative direct fluxes. We performed a simple spatial association of DIASources into DIAObjects with a one arcsecond matching radius.

The Machine Learning reliability model applied to DP1 was developed with the aim to meet the latency requirements for Rubin Alert Production when executed on CPUs. Accordingly we developed a relatively simple model: a Convolutional Neural Network with three convolutional layers, and two fully connected layers. The convolutional layers have a  $5 \times 5$  kernel size, with 16, 32, and 64 filters, respectively. A max-pooling layer of size 2 is applied at the end of each convolutional layer, followed by a dropout layer of 0.4 to reduce overfitting. The last fully connected layers have sizes of 32 and 1. The ReLU activation function is used for the convolutional layers and the first fully connected layer, while a sigmoid function is used for the output layer to provide a probabilistic interpretation. The cutouts are generated by extracting postage stamps of 51×51 pixels centered on the detected sources. The input data of the model consist of the template, science, and difference image stacked to have an array of shape (3, 51, 51). The model is implemented using PyTorch (J. Ansel et al. 2024). The Binary Cross Entropy loss function was used, along with the Adaptive Moment Estimation (Adam) optimizer with a fixed learning rate of  $1 \times 10^{-4}$ , weight decay of  $3.6 \times 10^{-2}$ , and a batch size of 128. The final model uses the weights that achieved the best precision/purity for the test set. Training was done on the SLAC Shared Scientific Data Facility (S3DF) with an NVIDIA model L40S GPU.

The model was initially trained using simulated data from the second DESC Data Challenge (DC2; (LSST Dark Energy Science Collaboration (LSST DESC) et al. 2021)) plus randomly located injections of PSFs to increase the number of real sources, for a total of 89,066 real sources. The same number of bogus sources were selected at random from non-injected DIASources. Once the LSSTComCam data were available, the model was fine-tuned on a subset of the data containing 183,046 sources with PSF injections. On the LSSTComCam test set, the model achieved an accuracy of 98.06%, purity of 97.87%, and completeness of 98.27%. As discussed in §5.8, the injections used to train this model version do not capture all types of astrophysical variability, so

1710

1711

1712

1713

1715

1716

1717

1718

1719

1720

1721

1722

1723

1724

1725

1727

1728

1729

1730

1731

1732

1733

1734

1735

1736

1737

1738

1739

1740

1741

1742

1743

1744

1745

1747

1748

performance on the test set will not be representative for variable stars, comets, and other types of variable objects.

#### 4.6.2. Light Curves

1753

1754

1768

1769

1786

1787

1794

To produce light curves, we perform multi-epoch forced photometry on both the direct visit images and the difference images. For light curves we recommend the forced photometry on the difference images (psDiffFlux on the ForcedSource Table), as it isolates the variable component of the flux and avoids contamination from static sources. In contrast, forced photometry on direct images includes flux from nearby or blended static objects, and this contamination can vary with seeing. Centroids used in the multi-epoch forced photometry stage are taken either from object positions measured on the coadds or from the DIAObjects (the associated DIASources detected on difference images).

#### 4.6.3. Solar System Processing

Solar system processing in DP1 consists of two key components: the association of observations (sources) with known solar system objects, and the discovery of previously unknown objects by linking sets of *tracklets*<sup>98</sup>.

To generate expected positions, ephemerides are computed for all objects found in the Minor Planet Center orbit catalog using the Sorcha survey simulation toolkit (Merritt et al., in press)<sup>99</sup>. To enable fast lookup of objects potentially present in an observed visit, we use the mpsky package (M. Juric 2025). In each image, the closest DiaSource within 1 arcsecond of a known solar system object's predicted position is associated to that object.

Solar system discovery uses the heliolinx package of asteroid identification and linking tools (A. Heinze et al. 2023). The suite consists of the following tasks:

- Tracklet creation with make\_tracklets
- Multi-night tracklet linking with heliolinc
- Linkage post processing (orbit fitting, outlier rejection, and de-duplication) with link\_purify

The inputs to the heliolinx suite included all sources detected in difference images produced by an early processing of the LSSTComCam commissioning data, including some that were later rejected as part of DP1 processing and hence are not part of DP1.

About 10% of all commissioning visits targeted the near-ecliptic field Rubin\_SV\_38\_7 chosen to facilitate asteroid discovery. Rubin\_SV\_38\_7 produced the vast majority of asteroid discoveries in DP1, as expected, but a few were found in off-ecliptic fields as well.

Tracklet creation with make\_tracklets used an upper limit angular velocity of 1.5 deg/day, faster than any main belt asteroid and in the range of many Near-Earth Object (NEO) discoveries. To minimize false tracklets from fields observed multiple times per night, the minimum tracklet length was set to three detections, and a minimum on-sky motion of five arcseconds was required for a valid tracklet.

The heart of the discovery pipeline is the heliolinc task, which connects ("links") tracklets belonging to the same object over a series of nights. It employs the HelioLinC3D algorithm (S. Eggl et al. 2020; A. Heinze et al. 2022), a refinement of the original HelioLinC algorithm of M. J. Holman et al. (2018).

The heliolinc run tested each tracklet with 324 different hypotheses spanning heliocentric distances from 1.5 to 9.8 astronomical unit (au) and radial velocities spanning the full range of possible bound orbits (eccentricity 0.0 to nearly 1.0). This range of distance encompasses all main belt asteroids and Jupiter Trojans, as well as many comets and Mars-crossers and some NEOs. Smaller heliocentric distances were not attempted here because nearby objects move rapidly across the sky and hence were not likely to remain long enough in an LSSTComCam field to be discovered. Candidate linkages, groups of tracklets whose propagated orbits cluster within a radius of  $1.33 \times 10^3$  AU at 1 AU, are identified, then post-processed via link purify to yeild a final, non-overlapping set of high-confidence asteroid candidates, ranked by orbit-fit residuals and related metrics.

# 5. PERFORMANCE CHARACTERIZATION AND KNOWN ISSUES

In this section, we provide an assessment of the DP1 data quality and known issues.

#### 5.1. Sensor Anomalies and ISR

In addition to the known detector features identified before LSSTComCam commissioning, most of which are handled by the ISR processing (see §4.2.1), we discovered a number of new types of anomalies in the DP1 data. Since no corrections are currently available for these anomalies, they are masked and excluded from downstream data products.

<sup>&</sup>lt;sup>98</sup> A tracklet is defined as two or more detections of a moving object candidate taken in close succession in a single night.

<sup>&</sup>lt;sup>99</sup> Available at https://github.com/dirac-institute/sorcha

#### 5.1.1. Vampire Pixels

"Vampire" pixels are visible on the images as a bright defect surrounded by a region of depressed flux, as though the defect is stealing charge from its neighboring pixels. Figure 10 shows an example of a vampire pixel near the center of R22\_S11 on an r-band flat.

From studies on evenly illuminated images, vampires appear to conserve charge. Unfortunately, no unique optimum way exists to redistribute this stolen flux so, following visual inspection, a defect mask was created to exclude them from processing. We have found some similar features on the ITL detectors on LSSTCam, and will use the same approach to exclude them.

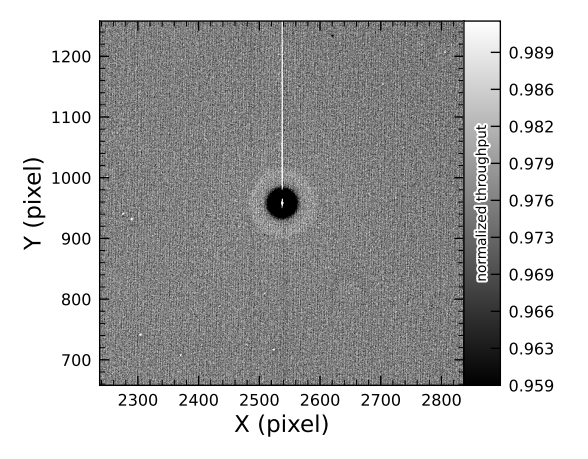


Figure 10. A large vampire pixel near the center of R22\_S11, as seen on the r-band flat. This clearly shows the central hot "vampire" pixels, surrounded by a region of depressed signal, with a brighter ring surrounding that caused by the local electric field effects. The charge contained in the central pixels is incompletely shifted as the image is read, and that charge leaks out into subsequent rows as they are shifted through the remnant charge. The columns that contain the hot pixels are masked as defects in all processing, as this feature cannot be otherwise corrected.

#### 5.1.2. Phosphorescence

Some regions of the LSSTComCam CCD raft were seen to contain large numbers of bright defects. An example is shown in Figure 11 in a g-band flat. On further investigation, it appears that on some detectors a layer of photoresist wax was incompletely removed from the detector surface during production. As this wax is now trapped below the surface coatings, there is no way to physically clean these surfaces. If this wax responded to all wavelengths equally, then it would likely result in quantum efficiency dips, which might be removable during flat correction. However, it appears that this wax is slightly phosphorescent, with a decay time on the order

of minutes, resulting in the brightness of these defects being dependent on the illumination of prior exposures. The worst of these regions were excluded with manual masks.

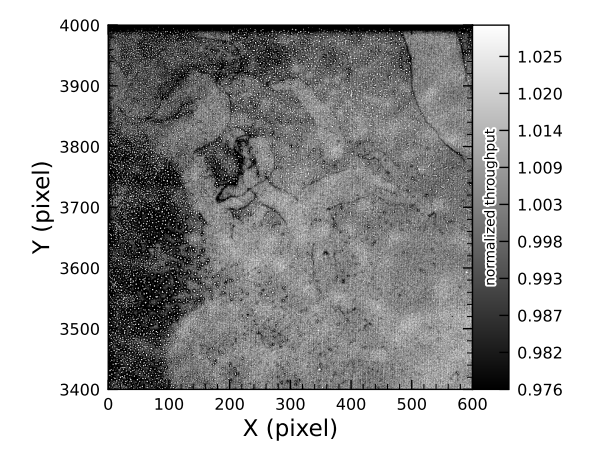


Figure 11. The top left corner of R22\_S01 in the g-band flat, showing the many small defect features that are caused by the remnant photoresist wax. A single large defect box masks this region from further analysis to prevent these features from contaminating measurements.

#### 5.1.3. Crosstalk

Crosstalk refers to unwanted signal interference between adjacent pixels or amplifiers. We use an average inter-amp crosstalk correction based on laboratory measurements with LSSTCam. These average corrections proved satisfactory, and so have been used as-is for DP1 processing. There are, however, some residual crosstalk features present post-correction, with a tendency towards over-subtraction. Figure 12 shows an example of a bright star with over-subtracted crosstalk residuals visible on neighboring amplifiers to both sides on exposure 2024120600239, detector R22 S02.

## 5.1.4. Bleed Trails

Bleed trails are produced when charge from saturated pixels spills into adjacent pixels. Bleed trails were anticipated on LSSTComCam sensors, but they appear in more dramatic forms than had been expected. As a bleed trail nears the serial register, it fans out into a "trumpet" shaped feature. Although bright, these features do not have consistently saturated pixels. In DP1 these "edge bleeds" were identified and masked.

Saturated sources can create a second type of bleed, where the central bleed drops below the background level. The depressed columns along these trails extend across the entire readout column of the detector, crossing the detector mid-line. We developed a model for

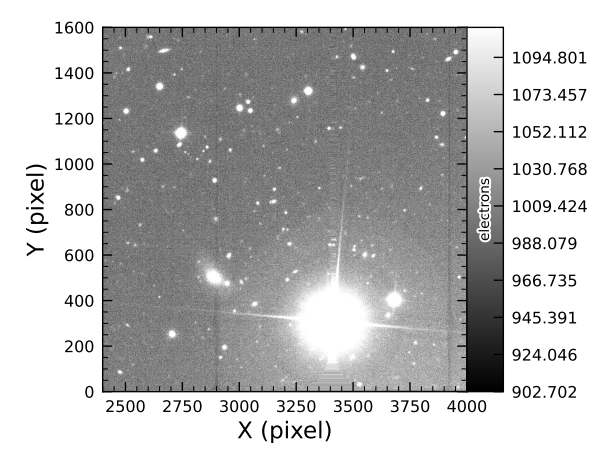


Figure 12. An example of a bright star with over-subtracted crosstalk residuals visible on neighboring amplifiers to both sides (exposure 2024120600239, detector R22\_S02). The horizontal banding stretching from the center of the star shows the interpolation pattern covering the saturated core and the ITL edge bleed near the serial register.

these to identify which sources are sufficiently saturated to result in such a trail, which is then masked. As this kind of trail appears only on the ITL detectors, we've named these features "ITL dips". Figure 13 shows an example of a bright star exhibiting the "ITL dip" phenomenon on exposure: 2024121000503, detector: R22\_-S21.

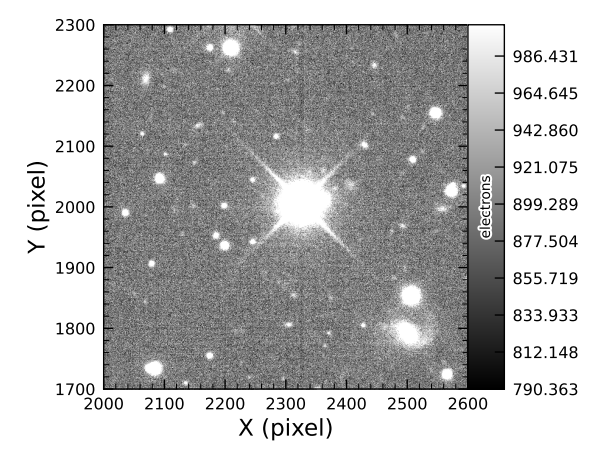


Figure 13. A bright star showing the "ITL dip" phenomenon, in which a dark trail extends out from the star to the top and bottom edges of the detector (exposure: 2024121000503, detector: R22\_S21).

#### 5.2. PSF Models

To characterize PSF performance, we use adaptive second moments (G. M. Bernstein & M. Jarvis 2002)

**Table 5.** Observed mean values and comparison of model residuals, across all visits and filters

Quantity	Observed	Piff O2	Piff O4
		$\times 10^{-4}$	$\times 10^{-4}$
$\langle T \rangle \text{ (pixel}^2)$	$11.366 \pm 0.003$		
$\langle e^1 \rangle$	$(-6.07 \pm 0.05) \times 10^{-3}$		
$\langle e^2 \rangle$	$(-4.57 \pm 0.05) \times 10^{-3}$		
$\langle e \rangle$	$(8.794 \pm 0.004) \times 10^{-2}$		
$\langle \delta T/T \rangle$		$-4.0\pm0.2$	$-5.0\pm0.2$
$\langle \delta e^1 \rangle$		$0.6\pm0.1$	$0.5 \pm 0.1$
$\langle \delta e^2 \rangle$		$0.0 \pm 0.1$	$0.0 \pm 0.1$

measured on PSF stars and on the PSF model using the HSM implementation (C. Hirata & U. Seljak 2003; R. Mandelbaum et al. 2005). All measurements are expressed in the pixel coordinate frame of each detector. We characterize the performance of the PSF using the classical trace of the second moment matrix T, along with the ellipticity parameters  $e^1$  and  $e^2$ . Measurements on the observed PSF stars are are denoted as  $T_{\rm PSF}$ ,  $e^1_{\rm PSF}$ , while those from PSF models are denoted as  $T_{\rm model}$ ,  $e^1_{\rm model}$ ,  $e^2_{\rm model}$ . We compare two PSF modeling approaches:

- Piff with second-order polynomial interpolation (Piff O2), the pipeline's default, and
- Piff with fourth-order polynomial interpolation (Piff O4), which serves as the final DP1 PSF model.

Table 5 summarizes each model's ability to reconstruct the mean T,  $e^1$ , and  $e^2$  on LSSTComCam. Both models exhibit a negative residual bias in the reconstructed PSF size, with Piff O4 providing improved performance over Piff O2.

An alternative approach to evaluating the performance of the PSF model is to examine the average  $\delta T/T$ , where  $\delta T$  is  $T_{\rm PSF}$  -  $T_{\rm model}$ , across visits, projected onto focal-plane coordinates, as shown in Figure 14. Piff reveals strong spatial correlations in the residuals, including a systematic offset consistent with the results presented in Table 5. The presence of these spatial structures motivated the adoption of fourth-order polynomial interpolation in all bands except u-band. Although not shown in Figure 14, residual patterns persist even with third-order interpolation, indicating that it is insufficient to capture the complexity of the PSF variation. Increasing the interpolation order to five would nominally reduce the residuals further, but the limited num-

ber of stars available on some CCDs would not provide
adequate constraints for such a model, while the resulting improvement would likely be minimal. Preliminary
analysis of LSSTCam data in the laboratory at SLAC
National Accelerator Laboratory (SLAC) shows that the
ITL sensors exhibit the same pattern as ITL sensors on
LSSTComCam.

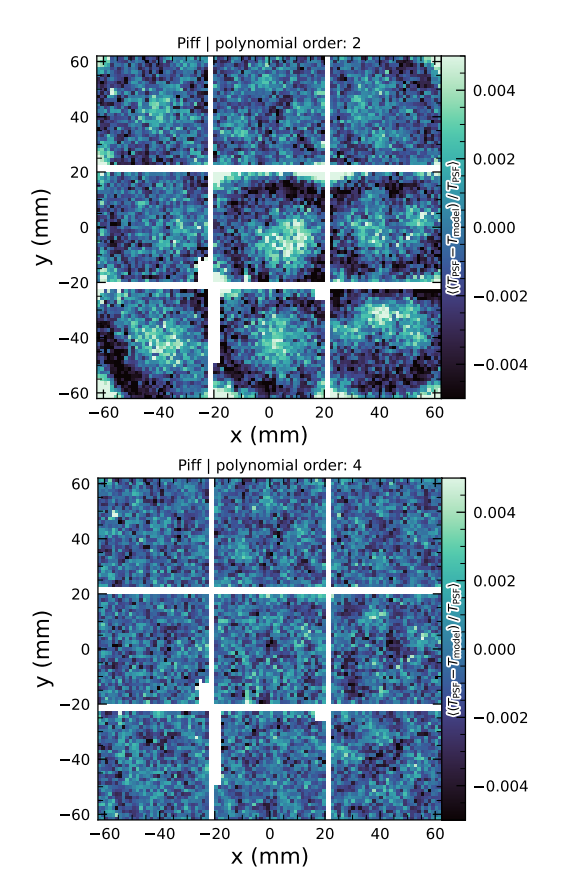


**Figure 14.** Average across all visits of  $\delta T/T$  for Piff O2 and Piff O4 modeling on LSSTComCam. Averages are computed using a  $120 \times 120$  binning.

Another way to look at the PSF modeling quality is via whisker plots of the PSF second and fourth moments and their modeling residuals projected on a part of the sky. In addition to the second moment, the spin-2 fourth moments,  $e^{(4)}$ , are defined as:

$$\begin{split} e_1^{(4)} &= M_{40} - M_{04} \\ e_2^{(4)} &= 2 \left( M_{31} - M_{13} \right), \end{split}$$

where  $M_{\rm pq}$  are the standardized higher moments as defined in T. Zhang et al. (2023) measured on stars and PSF models. Figure 15 shows the whisker plots of e,  $e^{(4)}$  (top rows), and  $\delta e$ ,  $\delta e^{(4)}$  in the Extended Chandra Deep Field-South Survey (ECDFS) field. The direction of a

whisker represents the orientation of the shape, while the length represents the amplitude |e| or  $|e^{(4)}|$ . We observe coherent patterns in both the PSF moments and the residuals, the latter of which warrants further investigation if it persists in future data releases.

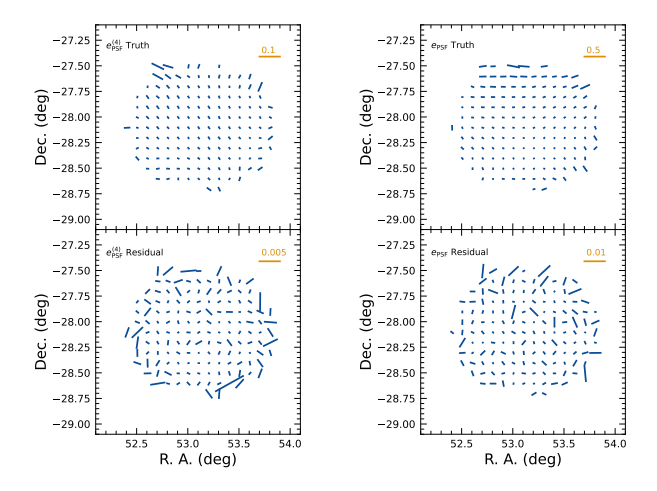


**Figure 15.** Whisker plots for the ECDFS field for e,  $e^{(4)}$  and  $\delta e$ ,  $\delta e^{(4)}$ .

Figure 16 shows a plot of  $\delta T/T$  versus stellar magnitude, which can reveal any dependencies between PSF size and flux. We also repeat this analysis in color bins to probe chromatic effects. Binning by color uncovers a clear color dependence, as was also seen in DES (M. Jarvis et al. 2021). The residual is consistent with Table 5 and its cause is unknown. DP1 does not include the color correction implemented in the DES Year 6 analysis, T. Schutt et al. (2025). This will be included in processing of future data releases.

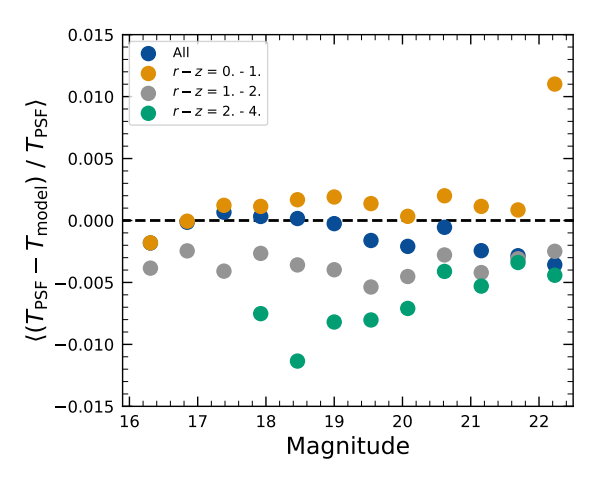


Figure 16. Binned  $\delta T/T$  as a function of magnitude across all visits and filters and in bins of stellar colors.

1948

1949

1950

1951

1952

1953

1954

1955

1956

1957

1959

1960

1962

1963

1964

1965

1966

1967

1968

1969

1970

1971

1972

1973

1974

1976

1978

1979

1980

As noted in Rubin Observatory Science Pipelines Developers (2025), two key Piff features were not used in the DP1 processing. PSF color dependence was not implemented, and, while Rubin software allows Piff to work with sky coordinates (including WCS transformations), it does not yet correct for sensor-induced astrometric distortions such as tree rings (H. Y. Park et al. 2017). Both features are planned for upcoming releases.

#### 5.3. Astrometry

To characterize astrometric performance, we evaluate both internal consistency and agreement with an external reference. The primary measure of internal consistency is the repeatability of position measurements for the same object, defined as the RMS of the astrometric distance distribution for stellar pairs having a specified separation in arcminutes. We associate isolated point sources across visits and compute the rms of their fitted positions, rejecting any stars with another star within 2". Figure 17 shows the median per-tract rms astrometric error in RA for all isolated point sources, both after the initial calibration and after the final calibration, which includes proper motion corrections. The results indicate that the astrometric solution is already very good after the initial calibration. Global calibration yields only modest improvement, likely due to the short time span of DP1 and the minimal distortions in the LSSTComCam. In the main survey, the longer time baseline and greater distortions near the LSSTCam field edges will make global calibration more impactful. An additional measure of internal consistency is the re-

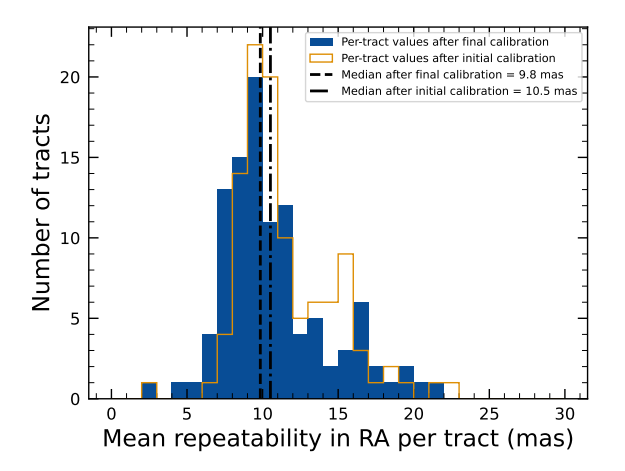
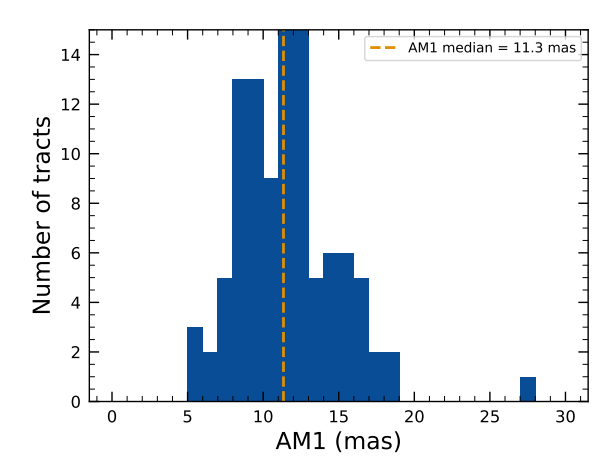


Figure 17. Mean per-tract astrometric repeatability of measurements of isolated point sources in RA in visits across all bands.

peatability of separations between objects at a given distance. To compute this, we identify pairs of objects that

are separated by a specified distance and measure their precise separation during each visit in which both objects are observed. The scatter in these separation measurements provides an indication of the internal consistency of the astrometric model. Figure 18 shows the median separation for pairs of objects separated by approximately 5 arcminutes, computed per tract after the final calibration. These values are already approaching the design requirement of 10 mas.



**Figure 18.** Median per-tract repeatability in separations between isolated point sources 5 arcmin apart in visits across all bands.

1991

1992

1995

1996

1997

1998

2000

2001

2002

2003

2004

2005

2006

2007

2008

2009

2010

2014

2016

To assess external consistency, we consider the median separation between sources not included in the astrometric fit and associated objects from a reference catalog. For this, we use the Gaia DR3 catalog, with the object positions shifted to the observation epoch using the Gaia proper motion parameters. Figure 19 shows the median separation for each visit in the r-band in tract 4849 in the ECDFS fields (Table 3). The calculated values are almost all within 5 mas, well below the design requirement of 50 mas for the main survey. By examining the astrometric residuals, we can assess whether there are distortions not accounted for by the astrometric model. In some cases, residuals from a single visit exhibit behavior consistent with atmospheric turbulence, as shown in Figure 20, which is characterized by a curl-free gradient field in the two-point correlation function of the residuals (E-mode), P. F. Léget et al. (2021) and W. F. Fortino et al. (2021). However, as seen in Figure 21, the residuals in many visits also have correlation functions with a non-negligible divergence-free B-mode, indicating that some of the remaining residuals are due to unmodeled instrumental effects, such as rotations between visits.

We can see unmodeled camera distortions by stacking the astrometric residuals over many visits as a function

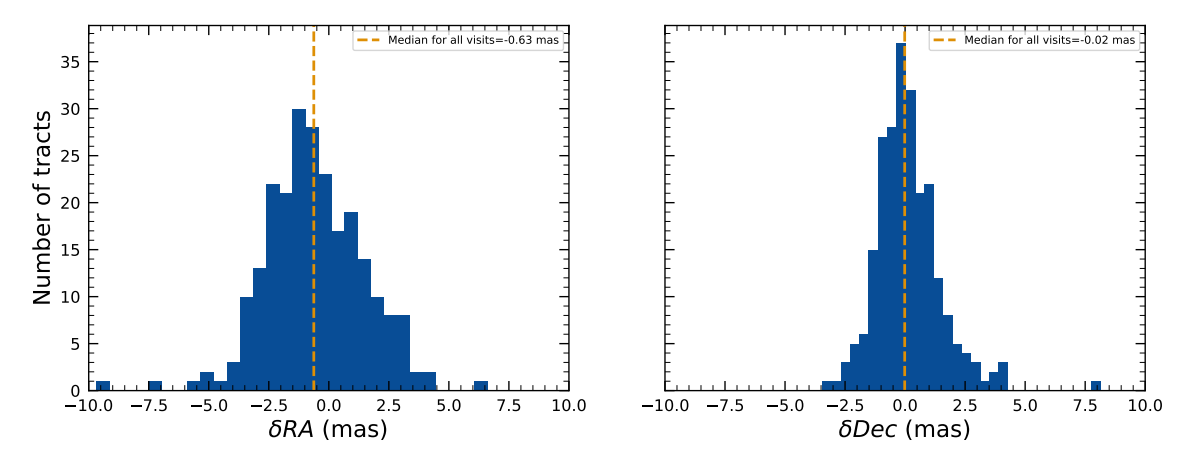


Figure 19. Median absolute offset for all visits in r-band in tract 4849 in the ECDFS field. The offset is the difference between the positions of isolated point sources that were reserved from the astrometric fit and matched objects from the Gaia DR3 catalog.

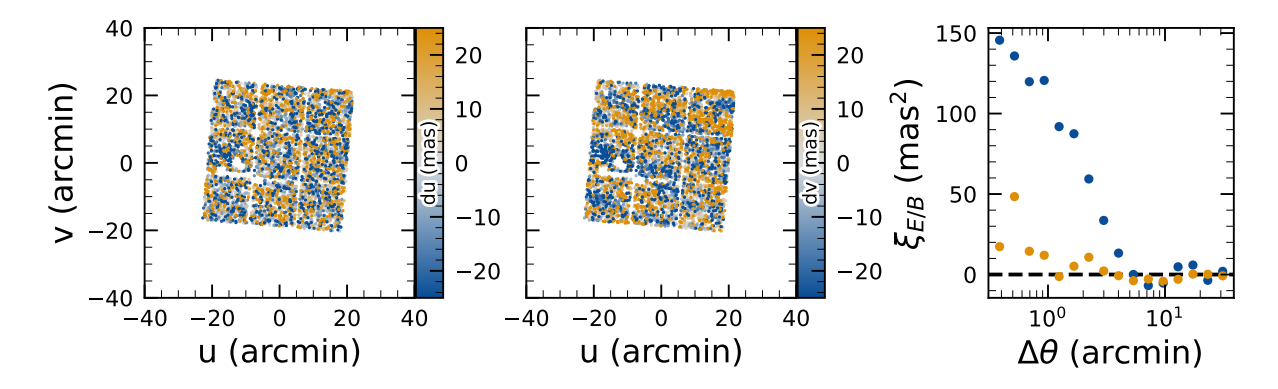


Figure 20. Astrometric residuals in u (left panel) and v (center panel) directions with the E (blue) and B (orange) modes of the two-point correlation function (right panel) seen in visit 2024120200359 in tract 2393 in u band. The residuals show a wave-like pattern characteristic of atmospheric turbulence, and there is significant E-mode and negligible B-mode in the correlation function.

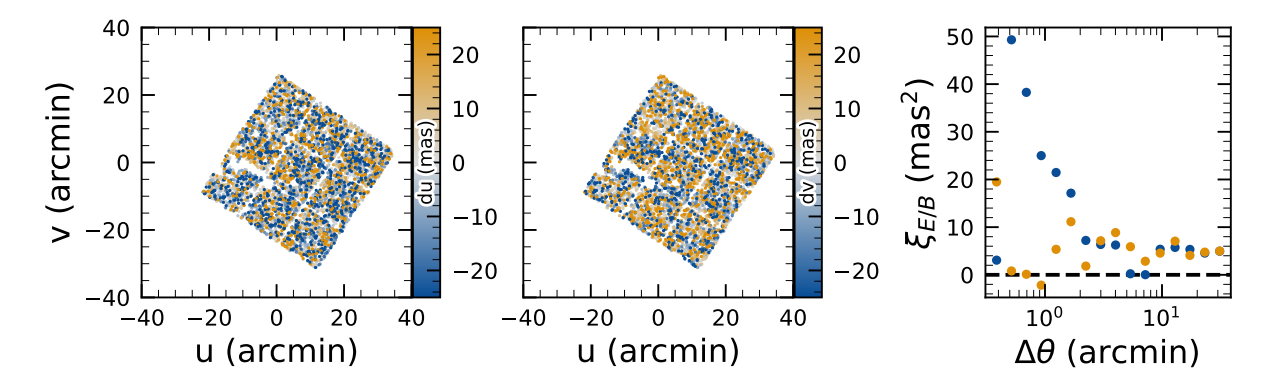


Figure 21. Astrometric residuals in u (left panel) and v (center panel) directions, with the E (blue) and B (orange) modes of the two-point correlation function (right panel) seen in visit 2024120700527 in tract 2393 in u band. There are coherent residuals, but without the wave-like pattern seen in Figure 20, and the correlation function has significant values for both E and B-modes.

of the focal plane position. Figure 22 shows the median 2020 residuals in x and y directions for 1792 visits. Spatial

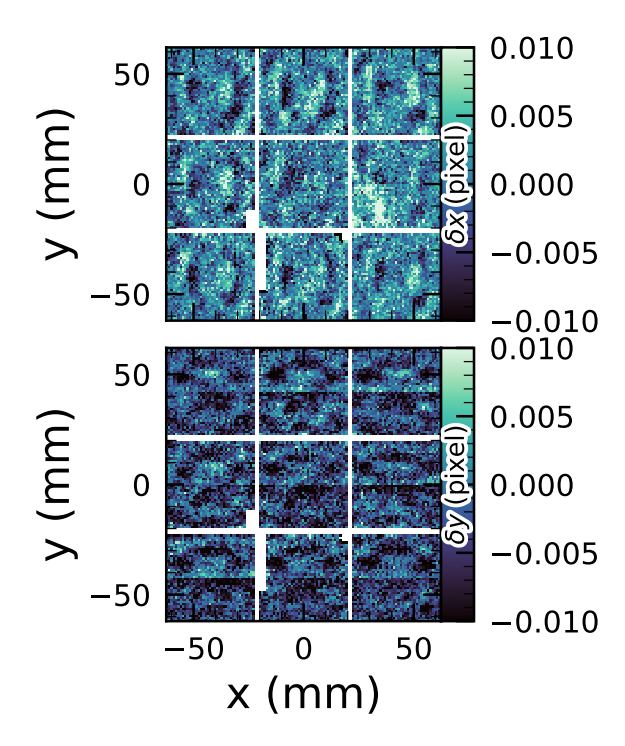
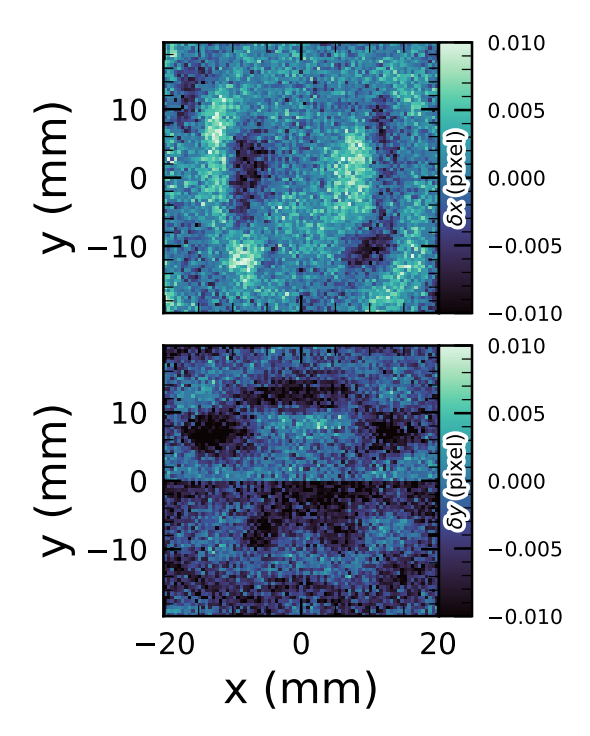


Figure 22. Median astrometric residuals as a function of focal plane position, shown in the left panel for the x direction and in the right panel for the y direction, for all nine LSSTComCam CCDs independently. The range of the color scale is  $\pm$  0.01 pixels, corresponding to 2 mas, showing that the effect is small.

structures are evident at the CCD level, as well as at the mid-line break, the discontinuity between the two rows of amplifiers, in the y-direction residuals. Further stacking all the detectors makes certain effects particularly clear. Figure 23 shows distortions very similar to those measured for an LSSTCam ITL sensor in a laboratory setting in J. H. Esteves et al. (2023).

#### 5.4. Differential Chromatic Refraction

Differential Chromatic Refraction (DCR) occurs when light passes through Earth's atmosphere, refracting more for shorter wavelengths, which causes blue light to appear shifted closer to the zenith. This wavelength-dependent effect results in the smearing of point sources along the zenith direction, specifically parallel to the parallactic angle. The DCR effect is observable in LSSTComCam data, particularly in the angular offset versus g-i band magnitude difference plots, as shown in Figure 24. These plots contain 228 visits chosen to maximize the range of observed airmass. When looking at data perpendicular to the parallactic angle, sources exhibit no discernible DCR effect, which is expected, and



**Figure 23.** Median residuals as a function of pixel position, shown in the left panel for the x direction and in the right panel for the y direction. These residuals are aggregated across all nine CCDs that comprise the central LSSTCom-Cam raft. The range of the color scale is  $\pm$  0.01 pixels, corresponding to 2 mas, showing that the effect is small.

form a clear vertical distribution on the two-dimensional density plots in Figure 24.

In contrast, sources aligned with the parallactic angle exhibit a tilted, linear distribution, clearly demonstrating that the relationship between angular offset and the g-i band magnitude difference, thereby providing a visual indication of the DCR effect. The DCR effect will be addressed in future releases.

#### 5.5. Stellar Photometry

The photometric repeatability for isolated bright unresolved sources following the FGCM fits was excellent. For the 10% of unresolved sources withheld from the fit and having signal-to-noise ratios greater than 100, the photometric repeatability after applying chromatic correction was 7.1, 5.4, 5.4, 5.1, 5.9, and 6.5 mmag in the ugrizy bands respectively, across all fields. After accounting for photometric noise, the intrinsic photometric repeatability was approximately 4.8, 2.7, 1.7, 1.0, 2.0, and 1.1 mmag in ugrizy. The DP1 processing does not yet include chromatic corrections in the final photometry. In this case the delivered photometric repeatability was 3–8 mmag for grizy.

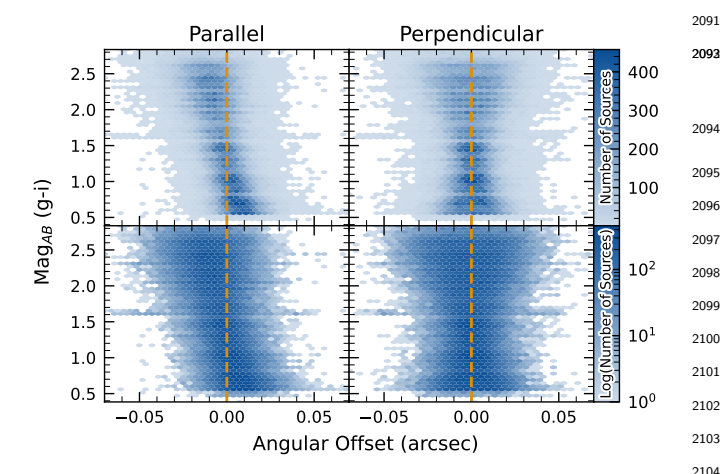


Figure 24. Visualization of Differential Chromatic Refraction (DCR) observed in the LSSTComCam commissioning campaign. The g-i color is computed for every source in the reference catalog that is matched to a direct source in the science image, and the binned density for the full survey is plotted against the angular offset between the reference and detected positions. The angular offset is projected along coordinates parallel and perpendicular to the parallactic angle of the observation, and shows a characteristic correlation along the parallel axis with no correlation along the perpendicular axis. The orange vertical dashed line indicates the expected q-i magnitude distribution at zero angular offset.

2112

2115

In Figure 25, we show the stellar loci for ugriz for unresolved sources in the DP1 Object table (§3.2). These unresolved sources were selected using the extendedness parameter (§3.2) in the Object catalog. This parameter is assigned a value of 0 (unresolved) or 1 (resolved) in each band based on the difference between the PSF and CModel magnitudes. The extendedness is set to 1 when this magnitude difference exceeds 0.016 mag, as the PSF flux for extended sources is biased low relative to the CModel flux. This method has been previously employed by the SDSS pipelines, and its statistical properties, including the optimal combination of information from different bands and repeated measurements, are discussed in C. T. Slater et al. (2020).

2066

2067

2068

2070

2071

2072

2073

2074

2076

2077

2078

2079

2080

2081

2082

2083

2084

2085

2087

2088

2090

Figure 26 illustrates the behavior of the extendness parameter. Its behavior in the g and r bands is similar, with unresolved sources scattered around the vertical line centered on zero. The width of the distribution increases towards fainter magnitudes. Resolved sources are found to the right and the dashed lines in the top panels show the adopted "star-galaxy" separation boundary. The morphology of the two color-magnitude diagrams in the bottom panels suggest that the unresolved sample suffers from increasing contamination by galaxies for r > 24. This behavior is consistent with

simulation-based predictions from C. T. Slater et al. (2020).

#### 5.6. Detection Completeness on Coadds

We characterize completeness by injecting synthetic sources into coadded images, and by comparing source detections to external catalogs. In both cases, we use a greedy, probabilistic matching algorithm that matches reference objects, in order of descending brightness, to the most likely target within a 0.5'' radius.

We inject sources in 12 of the patches of the ECDFS region with the deepest coverage. The input catalog contains stars and galaxies from part of the Data Challenge 2 (DC2) simulations (LSST Dark Energy Science Collaboration (LSST DESC) et al. 2021), where the galaxies consist of an exponential disk and de Vaucouleurs (G. de Vaucouleurs 1948, 1953) bulge. To avoid deblender failures from excessive increases in object density, stars with a total flux (i.e., summed across all six bands) brighter than 17.5 mag are excluded, as are galaxies whose total flux is brighter than 15 mag or fainter than 26.5 mag. Half of the remaining objects are selected for injection. Afterwards, individual bulge and disk components fainter than 29 mag are also excluded, both for computational expediency and because their structural properties are less likely to be representative of real galaxies.

Figure 27 shows completeness as a function of magnitude for these injected objects in the ECDFS field. These completeness estimates are comparable to results from matching external catalogs. Matching to the Hubble Legacy Field catalog (G. Illingworth et al. 2016; K. E. Whitaker et al. 2019) reaches 50% completeness at F775W = 26.13, or about i = 25.83 from differences in matched object magnitudes. Similarly, completeness drops below 90% at VIS = 23.80 from matching to Euclid Q1 (Euclid Collaboration et al. 2025) objects, equivalent to roughly i = 23.5. The Euclid imaging is of comparable or shallower depth, so magnitude limits at lower completeness percentages than 90% are unreliable, whereas the HST images cover too small and irregular of an area to accurately characterize 80-90% completeness limits.

At the 80% completeness limit, nearly 20% of objects, primarily injected galaxies, are incorrectly classified as stars based on their reference band extendedness. Similarly, the fraction of correctly classified injected stars drops to about 50% at i=23.8 (corresponding to 90% completeness).

This analysis has several caveats. The selection of objects for matching in any catalog is not trivial. Some fraction of the detections are spurious, particularly close

2146

2147

2148

2149

2150

2151

2152

2153

2155

2156

2157

2158

2159

2160

2161

2162

2163

2164

2165

2166

2167

2168

2169

2170

2171

2172

2173

2174

2175

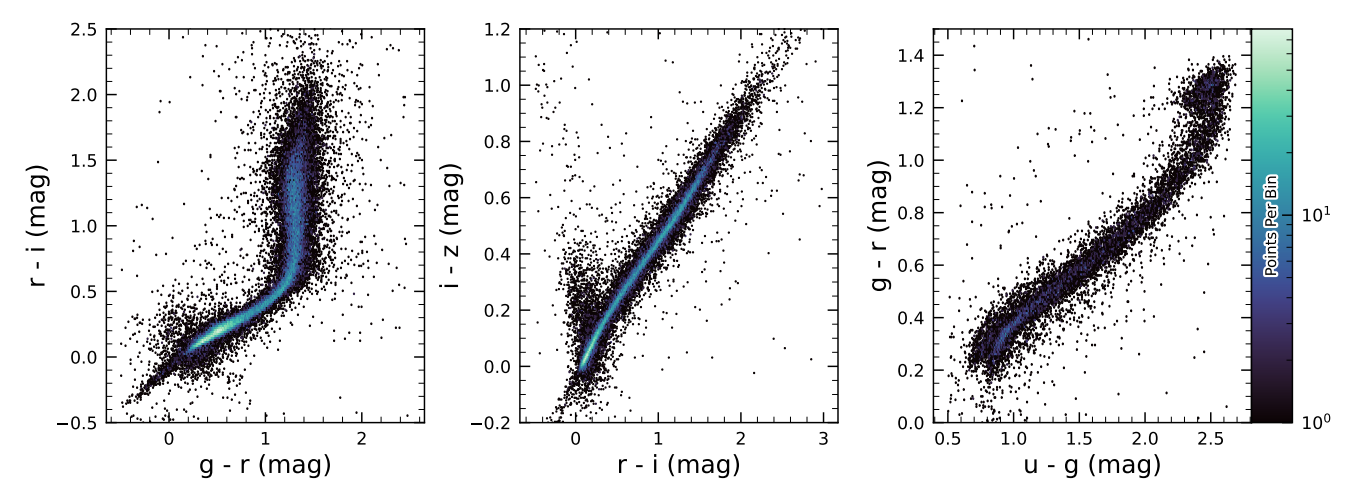


Figure 25. Examples of stellar loci for unresolved sources from the DP1 dataset. From left to right: qri stellar locus containing 63,236 stars with signal-to-noise ratio > 200 in the i band; riz stellar locus containing 46,760 stars with signal-to-noise ratio > 200200 in the i band ugr stellar locus containing 12,779 stars with signal-to-noise ratio > 50 in the u band.

2188

2190

2191

2194

2205

to bright stars and their diffraction spikes. Addition- 2176 ally, some objects lie in masked regions of one survey 2177 but not another, which has not been accounted for. For injected source matching, the reference catalog does not include real on-sky objects. Based on prior analyses of the DC2 simulations, purity is generally greater than completeness at any given magnitude. Similarly, for bright (i < 23) objects classified as stars by reference band extendedness, < 5% are either unmatched to a Euclid or HST object, or misclassified - that is, selecting on extendedness alone yields a fairly pure but incomplete sample of stars. We expect to remedy some of these shortcomings in future releases.

#### 5.7. Model Flux and Shape Measurement

Figure 28 shows i-band magnitude residuals for CModel and Sérsic measurements using the matched injected galaxies described in §5.6. Similar behavior is seen in other bands. Sérsic fluxes show reduced scatter for galaxies with i < 22.5, though CModel fluxes are less biased, with median residuals closer to zero and less magnitude-dependent. For fainter objects, Sérsic fluxes are more biased and less accurate. The magnitude of this bias is considerably larger than previously seen in simulated data and is being investigated. Aperture fluxes - including Kron and GAaP - are not shown as they are not corrected to yield total fluxes. The correction for Kron fluxes can be derived from the Sérsic index (A. W. Graham & S. P. Driver 2005), but this correction is not provided in object tables.

Figure 29 shows q - i color residuals versus r-band magnitude for the same sample of galaxies as Figure 28. For this and most other colors, GAaP (with a 1" aperture) and Sérsic colors both yield lower scatter; however, the CModel colors have the smallest bias. Curiously, the GAaP bias appears to be magnitude-dependent, whereas the Sérsic bias remains stable from 19 < r < 26. Any of these color measurements are suitable for use for deriving quantities like photometric redshifts, stellar population parameters, etc.

In addition to photometry, some algorithms include measurements of structural parameters like size, ellipticity, and Sérsic index. One particular known issue is that many (truly) faint objects have significantly overestimated sizes and fluxes. This was also seen in the Dark Energy Survey (K. Bechtol et al. 2025), who dubbed such objects "super-spreaders". These super-spreaders contribute significantly to overestimated fluxes at the faint end (see e.g. Figure 28), and are particularly problematic for the Kron algorithm (R. G. Kron 1980), which should only be used with caution.

As mentioned in §4.5, the Sérsic fits include a free centroid, which is initialized from the fiducial centroid of the object. Preliminary analyses of matched injected objects suggest that the Sérsic model galaxy astrometry residuals are somewhat smaller than for the standard centroids used in other measurements, and so users of the Sérsic photometry should also use these centroid values. One caveat is that for faint objects and/or in crowded regions with unreliable deblending, free centroids can drift significantly and potentially towards other objects, so objects with large differences between the fiducial and Sérsic astrometry should be discarded or used with caution.

Sérsic model parameter uncertainties are estimated by computing and inverting the Hessian matrix with

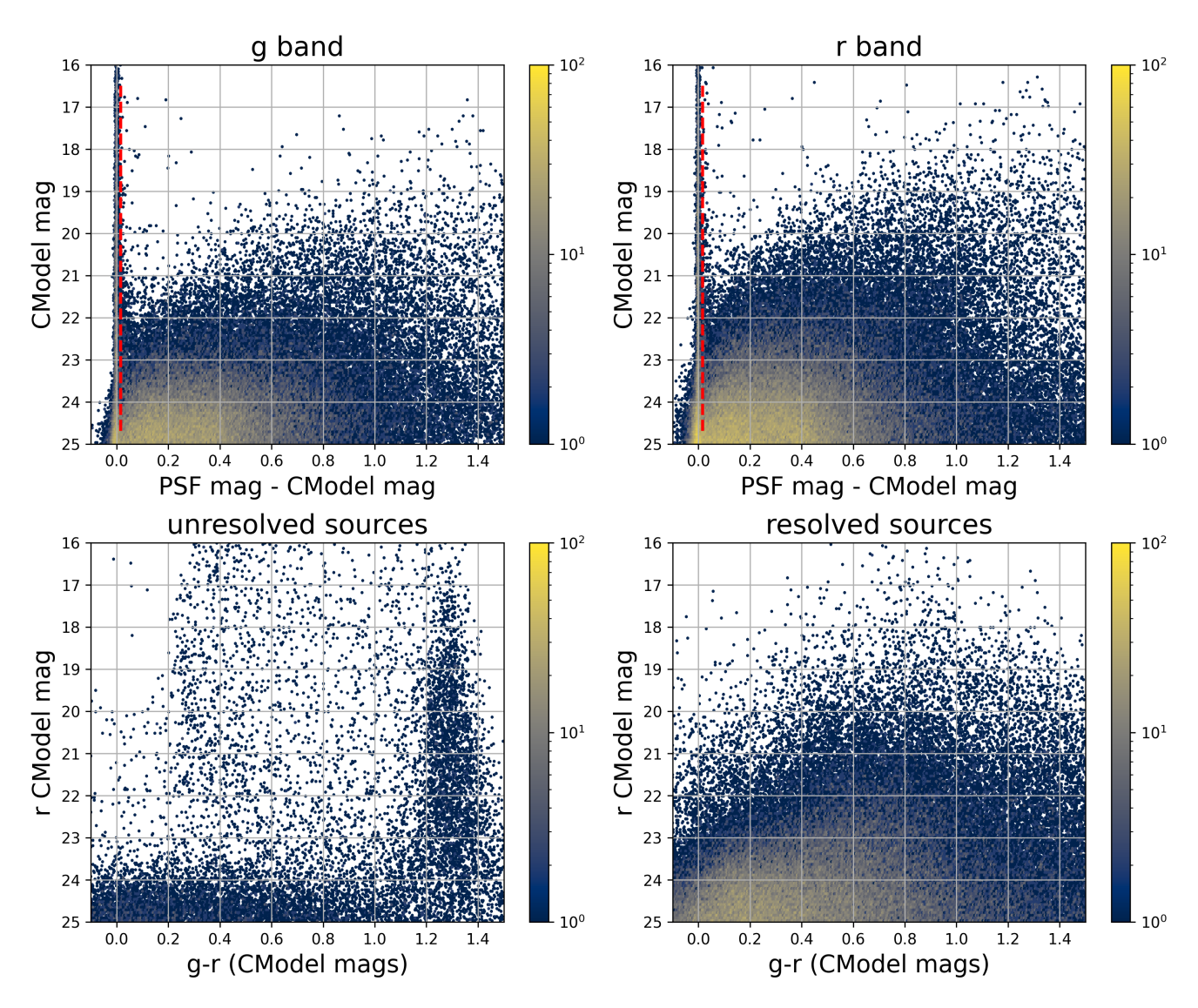


Figure 26. The top two panels shows the difference between the PSF and CModel magnitudes as a function of CModel magnitude in the g and r bands for 178,547 sources with  $CModel_r < 25$  from the ECDFS field. The vertical dashed line in each panel marks the minimum value (0.016 mag) for setting the extendedness parameter to 1. The bottom two panels show the r vs. g-r color-magnitude diagrams for 14,701 unresolved (left) and 163,666 resolved (right) sources. Note the unresolved sample suffers from increasing contamination by galaxies for r > 24.

the best-fit parameter values, after replacing the pixel data (but not uncertainties) by the best-fit model values. Currently, only the on-diagonal dispersion term (square root of the variance) is provided as an error estimate for each parameter. Future releases may provide more off-diagonal terms of the covariance matrix - particularly for the structural parameters, which are known to be correlated.

A major outstanding issue is that many parameter uncertainties - including but not limited to those for fluxes - are underestimated. This is at least partly (but not wholly) due to the fact that coaddition introduces 2231

covariance between pixels, which is not captured in perpixel variances.

The degree to which uncertainties are underestimated can depend on the parameter in question and on the brightness of the object. In plots of uncertainty-scaled residuals, the ideal behavior is for the median (i.e. the bias) to lie close to zero, and for the  $\pm 1\sigma$  lines to lie at  $\pm 1$ , without any dependence on magnitude. Figure 30 shows that flux and color uncertainties for PSF model magnitudes of injected stars are both underestimated, but by a factor of approximately 1.7-2 that is not very sensitive to SNR. This holds for astrometric/centroid parameters as well.

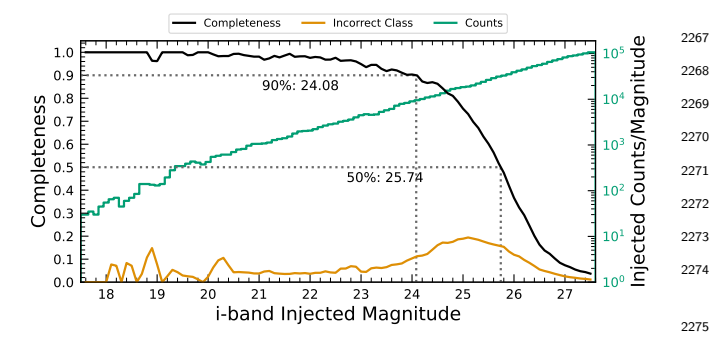


Figure 27. Completeness and incorrect classification fraction as a function of *i*-band CModel magnitude (Reference Magnitude) for DC2-based injected objects into a portion of the ECDFS field. The "Incorrect Class" line shows the proportion of objects that are matched but classified incorrectly by their reference-band extendedness, i.e. stars with extendedness of 1 or galaxies with extendedness of 0 in the reference band.

In turn, Figure 31 shows that CModel color uncertainties of galaxies are underestimated by a similar factor at the faint end, but with appreciable scaling with magnitude (and thereby SNR). Flux error underestimation is both larger than for colors and scales more strongly with SNR. This indicates that systematic effects dominate the errors in fluxes, particularly for bright galaxies. This is also at least partly but not wholly due to so-called model inadequacy - that is, the fact that galaxy models, parameteric or otherwise, are insufficiently complex to capture the structure of real galaxies.

Figure 32 shows that Sérsic model fluxes and colors have similar behavior as CModel, but with a greater degree of overestimation. This may be partly due to the fact that Sérsic parameter uncertainties are estimated along with the free centroid and structural (shape and Sérsic index) parameters, whereas the forced CModel fluxes and errors are derived from linear flux fits with a fixed shape and centroid.

Efforts are underway to investigate and quantify the origin of uncertainty underestimates and future releases will, at the least, provide recommendations for mitigations.

#### 5.8. Difference Imaging Purity

We assessed the performance of image differencing using human vetting and source injection (§5.9). Members of the DP1 team labeled more than 9500 DIASource image triplets consisting of cutouts from the science, template, and difference images. We classified these into various real and artifact categories. The raw artifact to real ratio without filtering was roughly 9:1. Bright stars are the main source of artifacts. Correlated noise, primarily in u and g bands, also leads to spurious detec-

tions near the flux threshold. We expect to be able to mitigate these effects for LSSTCam.

Applying a reliability threshold improves the purity of transients but not variable stars; technical limitations at the time of model training prevented injection of variable stars into the synthetic training set. Reliability models, described in §4.6.1, for LSSTCam data will be trained on a wider range of input data.

#### 5.9. Difference Imaging Detection Completeness

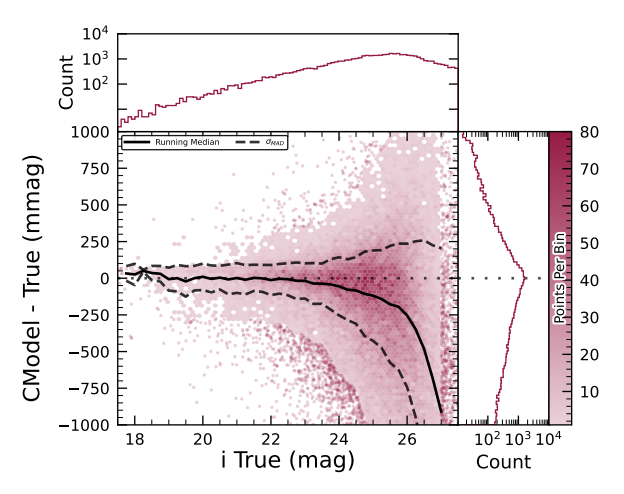
We assess the performance of our difference imaging pipeline using synthetic source injection on the science images prior to differencing. We construct a catalog of injected sources by joining two different samples of point sources, a set of hosted sources to emulate transients in galaxies and second set of hostless sources. The hosts are selected from the pipeline source catalog that is produced upstream by imposing a cut on their extendedness measurement and selecting  $N_{\rm src} = \min(100, N \times 0.05)$  of the N available sources per detector. For each host we pick a random position angle and radius using its light profile shape to decide where to place the source, and also a random value of brightness for the injected source, with magnitudes higher than the host source.

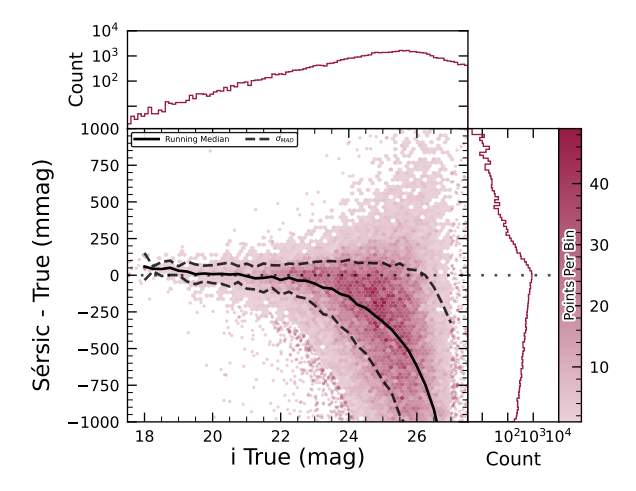
The hostless sources instead have random positions in the CCD focal plane, and magnitudes chosen from a random uniform distribution with  $20 \ge m \ge m_{lim} + 1$ , where  $m_{lim}$  is the limiting magnitude of the image. We used the LSST source\_injection package<sup>100</sup> to include these sources in our test images. We performed a coordinate cross-match task, with a threshold of 0.5 to find which of these sources were detected and which were lost, enabling the calculation of a set of performance metrics

In Figure 33 we show the detection completeness as a function of the SNR, for sources in the ECDFS field, for filters griz. We observe a completeness > 95% for sources with SNR> 6, with mean completeness  $\simeq 99\%$  and standard deviation of  $\simeq 0.7\%$ . In Figure 34 we show the distribution of the residuals of the recovered sky coordinates for the detected synthetic sources. The marginal distributions are both centered at zero, and for sources of SNR > 20 the residuals are compatible with normal distributions  $\mathcal{N}(\mu = 0, \sigma^2 = (0''.02)^2)$ . In Figure 35 we show photometry results for our detected synthetic sources in the i filter, using PSF photometry on the difference images. We include both the magnitude residuals as well as the flux pulls, defined as  $f_{PSF} - f_{True})/\sigma_{f_{PSF}}$  for PSF flux  $f_{PSF}$  and error

<sup>100</sup> https://pipelines.lsst.io/modules/lsst.source.injection/index. html

Rubin DP1 35

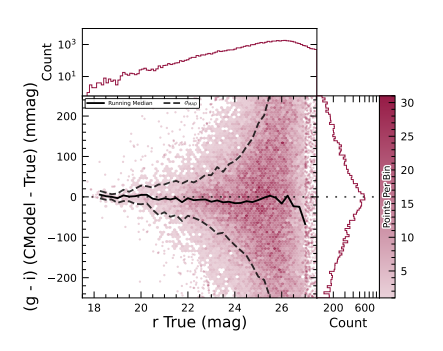


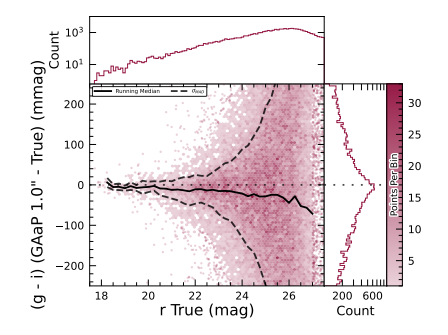


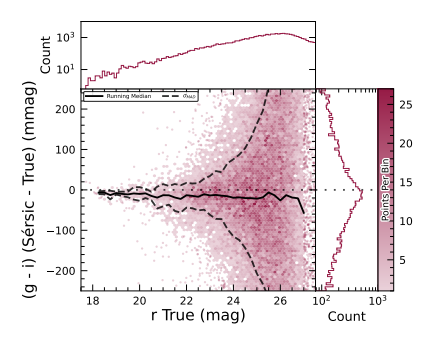
(a) i-band magnitude residuals for CModel measurements of injected galaxies.

(b) i-band magnitude residuals for Sérsic model measurements of injected galaxies.

Figure 28. i-band magnitude residuals for matched injected DC2 galaxies with the CModel and Sérsic algorithms in a portion of the ECDFS region, including the median and scatter thereof. The black line is the median.







(a) q-i color residuals for CModel measurements of injected galaxies.

2317

2318

2319

2320

2321

2322

2323

2324

2325

2326

2328

2329

2330

2331

2332

2333

2334

(b) q - i color residuals for GAaP measurements of injected galaxies.

(c) g - i color residuals for Sérsic model measurements of injected galaxies.

Figure 29. g-i color residuals versus true r-band magnitude for matched injected DC2 galaxies with the CModel, GAaP and Sérsic algorithms in a portion of the ECDFS region.

2345

2350

 $\sigma_{f_{PSF}}$ , as a function of the true magnitude of the synthetic sources, including the running median and median absolute deviation (MAD) for the whole brightness range. We also include the true magnitude distribution 2338 as well as the detection completeness on the top panel, and for reference the 90% and 50% completeness magnitude values in vertical lines. On the right panels we include the marginal distribution for sources brighter 2342 than mag < 22.5, splitting the data into hosted and hostless, as well as the robust mean and standard deviation. From this figure we can see that our flux measurements are accurate within a wide range of magnitudes, for both hosted and hostless synthetic sources. We find that the median offset is below 0.002 mag for true magnitudes below 21, and with a maximum  $\sigma_{MAD}$  scatter of about 0.02 mag in this range. For true  $m_i < 22.5$ , the robust running median PSF magnitudes residuals are < 0.02 mag, and when splitting into hosted and hostless

both robust median are well below 0.01, and robust  $\sigma$ , i.e.  $\sigma_{MAD}$  are also well below 0.05. For all sources with  $m_i < 21.5$  the running median is always  $|\langle \delta \rangle| < 0.1$ , and MAD  $\sigma_{\delta} < 1$ . Extending to sources with  $m_i < 22.5$  then hostless sources have a robust mean pull below 0.02, with a robust standard deviation < 1.15, while these parameters increase to 0.2 and 1.2 for hosted sources, suggesting that we might have contamination from host background sources potentially biasing our fluxes.

## 5.10. Solar System

## 5.10.1. Asteroid Linking Performance

The evaluation of asteroid linking performance in DP1 focused on demonstrating discovery capability. The solar system discovery pipeline produced 269,581 tracklets, 5,691 linkages, and 281 post-processed candidates.

As described in §4.6.3, post-processing of the heliolinc output with link\_purify produced a final set of

2355

2356

2358

2359

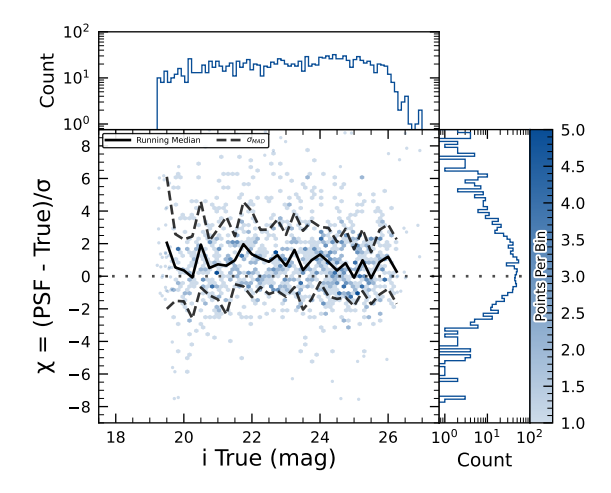
2360

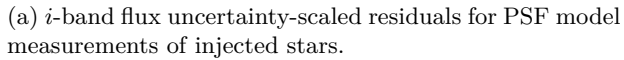
2361

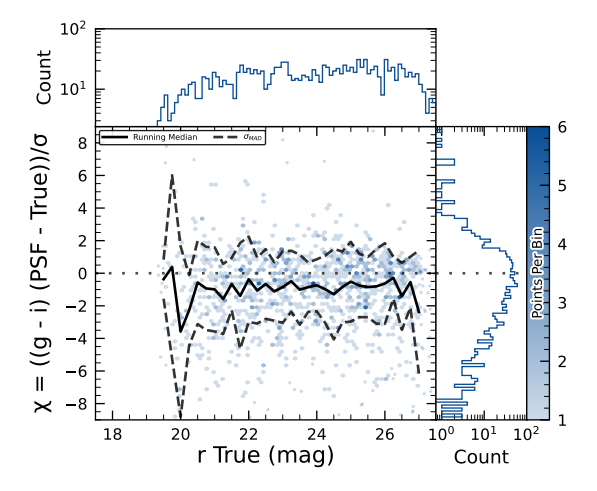
2362

2363

2365

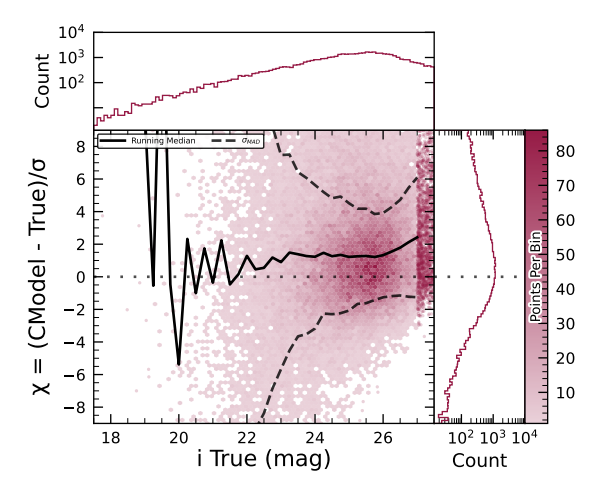




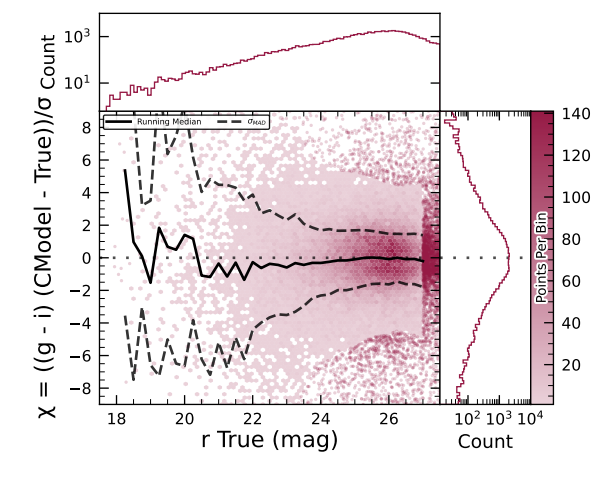


(b) g-i color uncertainty-scaled residuals for PSF model measurements of injected stars.

Figure 30. Color and flux uncertainty-scaled residuals for matched injected DC2 stars' PSF model measurements in a portion of the ECDFS region.



(a) *i*-band flux uncertainty-scaled residuals for CModel measurements of injected galaxies.

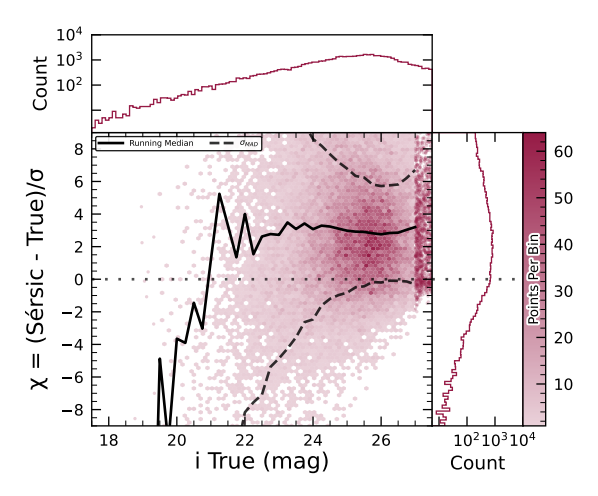


(b) g-i color uncertainty-scaled residuals for CM odel measurements of injected galaxies.

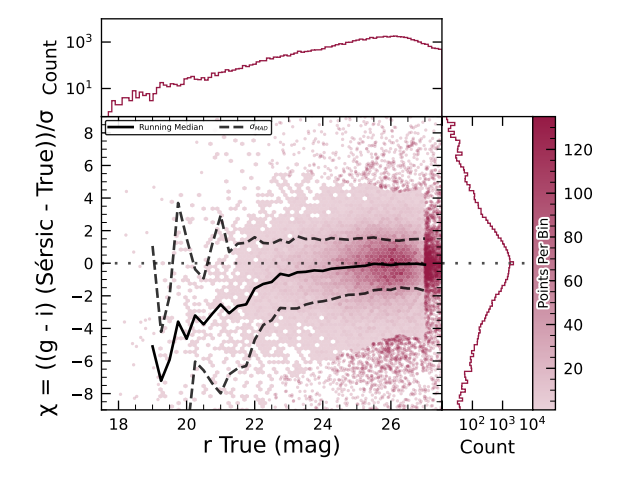
Figure 31. Color and flux uncertainty-scaled residuals for matched injected DC2 galaxies' CModel measurements in a portion of the ECDFS region.

281 candidate linkages, ranked with the most promising first. We then used find\_orb (B. Gray 2025) to derive orbit fits for each candidate, sorting the resulting list by  $\chi_{\rm dof}^2$ , a measure of fit quality. A conservative manual investigation of these candidates yielded a curated list of 93 probable new asteroid discoveries. Manual inspection of the linkages indicated that those ranked 0–137 corresponded to unique real asteroids; ranks 138–2374 200 contained additional real objects intermixed with some spurious linkages; and ranks higher than 200 were essentially all spurious. This analysis indicates that it will be possible to identify cuts on quality metrics such as  $\chi^2$  to define discovery candidate samples with high purity; determining the exact quantitative cut values re-

quires more data with LSSTCam. We next removed all observations matched to known asteroids (using Minor Planet Center (MPC)'s MPChecker service), reducing the number of candidates to 97. Of these, four had strong astrometric and/or photometric outliers, likely due to self-subtraction in difference images due to the unavoidable limitations of template generation from the limited quantity of data available from LSSTComCam. We suspect these four linkages do correspond to real objects, but have chosen to discard them out of an abundance of caution. The remaining 93 were submitted to the Minor Planet Center and accepted as discoveries, demonstrating the LSST pipelines are able to successfully discover new solar system objects.



(a) i-band flux uncertainty-scaled residuals for Sérsic model measurements of injected galaxies.



(b) g-i color uncertainty-scaled residuals for Sérsic model measurements of injected galaxies.

Figure 32. Color and flux uncertainty-scaled residuals for matched injected DC2 galaxies' Sérsic measurements in a portion of the ECDFS region.

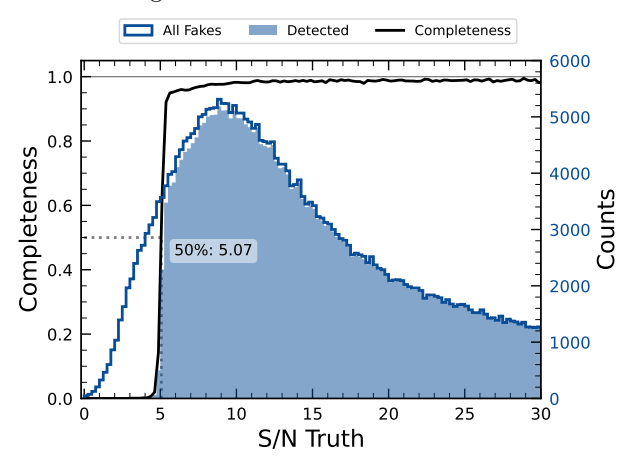


**Figure 33.** The difference image detection completeness for injected sources in the ECDFS field, for filters griz, as a function of the estimated signal to noise ratio SNR. This completeness is the ratio between the found fake sources (shaded histogram) and all the sources (solid line). The horizontal dashed line represents where the 50% completeness level is reached, at approximately SNR  $\simeq 5.07$ .

# 5.10.2. Asteroid Association Performance

2381

2382

2384

2385

2386

2387

2388

2389

2390

During the Solar System association step, 5988 *DiaSources* were linked to 431 unique Solar System objects, These include 3,934 *DiaSources* with 338 previously known objects cataloged by the MPC, and 2,054 *DiaSources* with the 93 newly-discovered objects. An additional 143 detections of these newly discovered objects were also recovered. These detections were not initially identified by the discovery pipelines, as they did not meet the required criteria for tracklet formation,

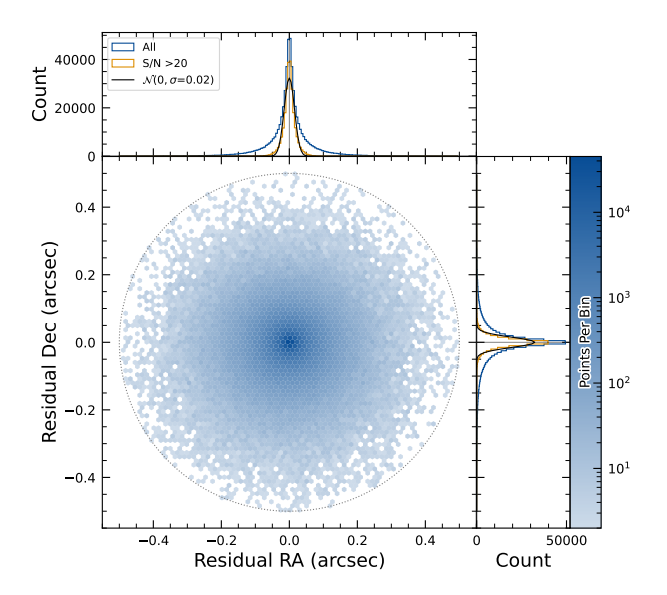


Figure 34. Coordinate residuals for detected synthetic sources in difference images, between recovered and true position of the sources in the ECDFS field. In the top and right panels we include the distribution of these offsets, for all sources as well as for sources with SNR> 20. These high SNR sources show gaussian coordinate residual distributions with  $\sigma=0.02$  (black solid lines). The circle reflects the matching radius of 0.52.

specifically the minimum number of detections and/or the maximum allowed time span between observations.

The astrometric residuals of known asteroid associations are shown in Figure 36. The astrometric precision for solar system sources is excellent, with the majority

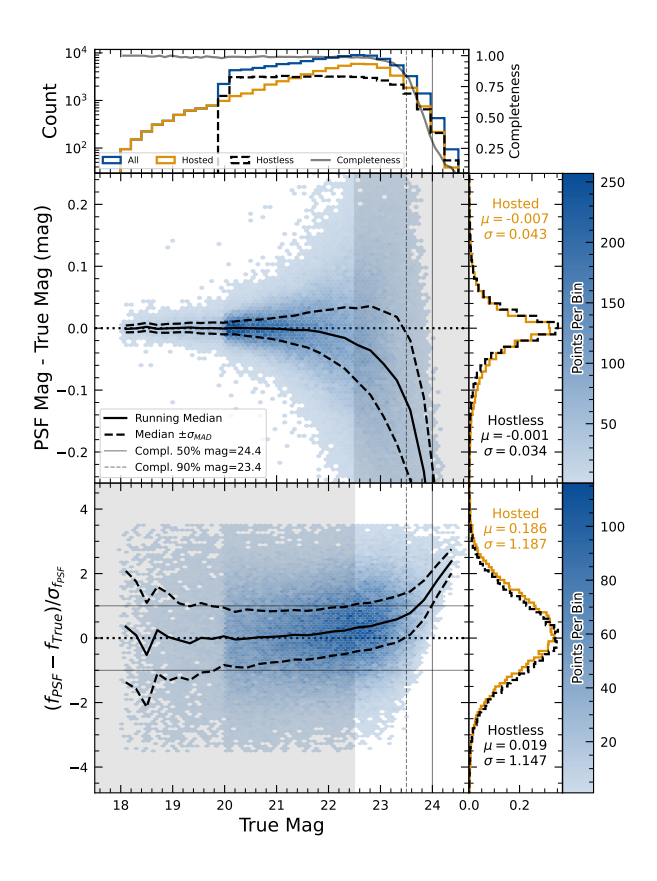


Figure 35. Magnitude residuals and flux pulls for i-band PSF photometry on difference images for ECDFS field in i for detected injected sources. Top panel: Distribution of true magnitudes for injected sources (blue), and split into hostless (black dash) and hosted (orange) sources, with detection completeness as a function of true magnitude (gray line). Vertical dashed lines indicate the 90% and 50% completeness magnitude limits. Center left panel: 2D hexbin plot of PSF magnitude residuals (measured minus true) versus true magnitude for detected sources, with running median (solid black) and  $\sigma_{MAD}$  (dashed black) overlaid. Center right panel: Marginalized distributions of PSF magnitude residuals for hostless (blue) and hosted (orange) sources with true magnitude  $m_i < 22.5$ , annotated with robust mean and standard deviation. Bottom left panel: 2D hexbin plot of PSF flux pulls versus true magnitude for detected sources, with running median (solid black) and  $\sigma_{MAD}$  (dashed black) overlaid. Bottom right panel: Marginalized distributions of PSF flux pulls for hostless (blue) and hosted (orange) sources with true magnitude  $m_i < 22.5$ , annotated with robust mean and standard deviation.

2407

2410

2411

2412

2414

2415

2416

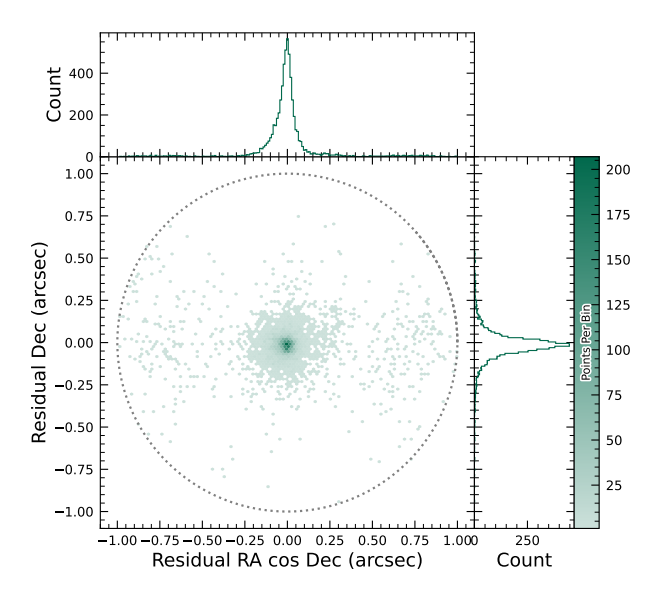


Figure 36. Astrometric residuals between expected and observed positions of Solar System Objects in DP1. The median residuals are 0.001 and -0.016 in R.A./Dec direction, with standard deviations of 0.019 and 0.010, respectively. No detectable systematic offset from zero indicates there are no major errors in either timing or astrometry delivered by the Rubin system. The wider scatter in the RA direction is due to objects whose measured orbital elements are less well constrained, translating to larger along-track positional errors in the predicted positions.

of objects detected within 0".1 of their expected positions. Taking the signed median residuals to search for biases, we find that previously-known objects have mean residuals of 0".001 and -0".016 in the RA and Dec directions respectively, while newly-discovered objects have mean residuals of -0".035 and -0".010 in the RA and Dec directions, respectively. These mean residuals are small enough to eliminate the possibility of a timing offset greater than the second-scale shutter motion, which is consistent with the timing studies presented in Section 2.2.2.

#### 5.11. Crowded Fields

Among the seven Rubin DP1 target fields, two stand out for their severe stellar crowding: the globular cluster 47 Tucanae (47\_Tuc) and the Fornax dwarf spheroidal galaxy (Fornax dSph). These fields were selected in part to stress-test the LSST Science Pipelines under high-density conditions. While both exhibit high stellar densities, the nature and spatial extent of the crowding differ significantly.

47 Tuc presents extreme crowding across much of the field, encompassing its dense core and the eastern re-

gions influenced by the Small Magellanic Cloud (SMC). 2469
This pervasive crowding leads to persistent challenges 2470
for deblending and reliable source detection, exposing 2471
field-wide limitations in the current pipeline performance (Y. Choi et al. 2025). In contrast, Fornax dSph 2473
shows significant crowding only in its central region, 2474
with outer areas remaining well resolved and easier to 2475
process. 2460

In both 47 Tuc and Fornax, extreme crowding led to the deblending step being skipped frequently when memory or runtime limits were exceeded, typically due to an excessive number of peaks, or large parent footprints. However, the impact of these limitations differed: in 47 Tuc, deblending was often skipped across the entire field, resulting in large gaps and substantially reduced completeness. In Fornax, these issues were largely confined to the central region, with much better recovery in the outskirts. This contrast highlights how the pipeline's limitations depend on the spatial extent of high-density regions: 47 Tuc exposed systematic, field-wide challenges, whereas Fornax revealed more localized, density-driven limits.

T. M. Wainer et al. (2025) explored the Rubin DP1 DiaObject catalog (§3.2) in the 47 Tuc field, which contains sources detected in difference images. Because forced photometry is performed at these positions across all single-epoch images, this dataset bypasses the coadd-based detection and deblending stages that often fail in crowded regions. By computing the median of the forced photometry for each DiaObject across available visits, they recovered approximately three times more candidate cluster members than found in the standard Object table (Y. Choi et al. 2025). This result underscores the value of difference-imaging—based catalogs for probing dense stellar regions inaccessible to standard coadd processing in DP1.

Although the DP1 pipeline was not optimized for crowded-field photometry, these early studies of 47 Tuc and Fornax provide critical benchmarks. They highlight both the limitations and opportunities for science with Rubin data in crowded environments, and they inform future pipeline development aimed at robust source recovery in complex stellar fields.

## 6. RUBIN SCIENCE PLATFORM

The RSP (M. Jurić et al. 2019) is a powerful, cloud-based environment for scientific research and analysis of petascale-scale astronomical survey data. It serves as the primary interface for scientists to access, visualize, and conduct next-to-the-data analysis of Rubin and LSST data. The RSP is designed around a "bring the compute to the data" principle, eliminating the need for

users to download massive datasets. Although DP1 is much smaller in size (3.5 TB) than many current survey datasets, future LSST datasets will be far larger and more complex, making it crucial to co-locate data and analysis for effective scientific discovery.

The RSP provides users with access to data and services through three distinct user-facing Aspects: a Portal, which facilitates interactive exploration of the data; a JupyterLab-based Notebook environment for data analysis using Python; and an extensive set of Application Programming Interfaces (APIs) that enable programmatic access to both data and services. The three Aspects are designed to be fully integrated, enabling seamless workflows across the RSP. The data products described in §3 are accessible via all three Aspects, and the system facilitates operations such as starting a query in one Aspect and retrieving its results in another. Figure 37 shows the Rubin Science Platform landing page in the Google cloud.

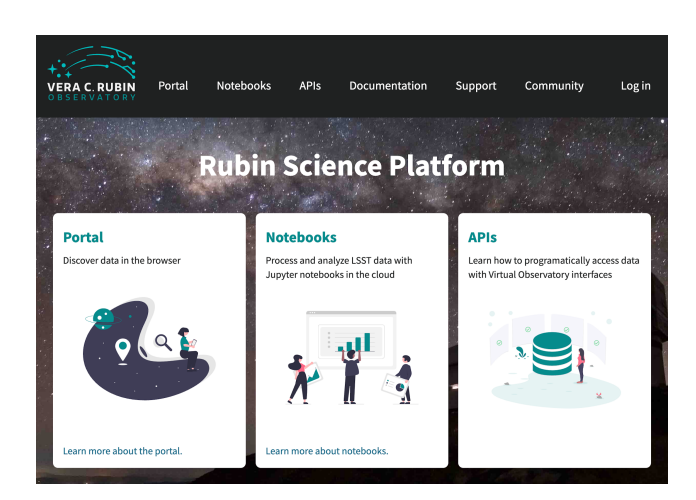


**Figure 37.** The Rubin Science Platform landing page at data.lsst.io showing the three user-facing Aspects as well as links to documentation and support information.

The RSP is supported by a number of back-end services, including databases, files, and batch computing. Support for collaborative work through shared workspaces is also included in the RSP.

A preview of the RSP was launched on Google Cloud in 2022, operating under a shared-risk model to support Data Preview 0 (W. O'Mullane et al. 2024a). This allowed the community to test the platform, begin preparations for science, and provide valuable feedback to inform ongoing development. It was the first time an astronomical research environment was hosted in a cloud environment. The DP1 release brings major updates to RSP services, enhancing scientific analysis capabilities. The RSP remains under active development, with incre-

2505

2507

2508

2509

2510

2511

2512

2513

2514

2515

2516

2517

2518

2519

2520

2521

2522

2524

2525

2526

2527

2528

2529

2530

2531

2532

2533

2535

2536

2537

2538

2539

2540

2542

2543

2545

2546

2547

2548

2549

2550

2551

mental improvements being rolled out as they mature. During the Rubin Early Science Phase, the RSP will continue to operate under a shared-risk model. This section outlines the RSP functionality available at the time of the DP1 release and provides an overview of planned future capabilities.

2555

2558

2559

2577

2582

2584

2585

2587

2588

2589

2590

2593

2597

# 6.1. Rubin Data Access Center

The Rubin US Data Access Center (US DAC) utilizes a novel hybrid on-premises-cloud architecture, which combines on-premises infrastructure at the USDF at SLAC with flexible and scalable resources in the Google cloud. This architecture has been deployed and tested using the larger simulated data set of DP0.2 (W. O'Mullane et al. 2024b).

In this hybrid model, user-facing services are deployed in the cloud to support dynamic scaling in response to user demand and to simplify the provisioning and management of large numbers of science user accounts. The majority of the static data products described in §3 are stored on-premises at the USDF to benefit from costeffective mass storage and close integration with Rubin data processing infrastructure, also located at the USDF. For imaging data, the Data Butler (§6.2.2) provides the interface between the cloud-based users and data services, and the on-premises data. For catalog data, a cloud-based TAP client (§6.2.1) submits queries to the on-premises Qserv database cluster (§6.5) and retrieves the results. In the initial DP1 deployment, catalog data is hosted at the USDF while image data is stored in the cloud. The full hybrid model will be rolled out and further tested following the release of DP1.

The RSP features a single-sign-on authentication and authorization system to provide secure access for Rubin data rights holders (R. Blum & the Rubin Operations Team 2020).

# 6.2. API Aspect

The API Aspect provides a comprehensive set of user-facing interfaces for programmatic access to the DP1 data products, through both IVOA-compliant services and the Rubin Data Butler. IVOA services enable standard queries and integration with existing tools, while the Butler facilitates advanced data processing within the LSST Science Pipelines.

At the time of the DP1 release, some IVOA services are unavailable, and certain data products are only accessible via the Butler. This section provides an overview of the available IVOA services and Butler access.

#### 6.2.1. IVOA Services

Rubin has adopted a Virtual Observatory (VO)-first design philosophy, prioritizing compliance with IVOA standard interfaces to foster interoperability, standardization, and collaboration. In cases where standardized protocols have yet to be established, additional services have been introduced to complement these efforts. This approach ensures that the RSP can be seamlessly integrated with community-standard tools such as Tool for OPerations on Catalogues And Tables (TOPCAT) (M. Taylor 2011) and Aladin (F. Bonnarel et al. 2000; T. Boch & P. Fernique 2014; M. Baumann et al. 2022), as well as libraries such as PyVO (M. Graham et al. 2014).

The user-facing APIs are also used internally within the RSP, creating a unified design that ensures consistent and reproducible workflows across all three Aspects. This reduces code duplication, simplifies maintenance, and ensures all users, both internal and external, access data in the same way. For example, an Astronomical Data Query Language (IVOA standard) (ADQL) query on the Object catalog via TAP yields identical results whether run from the Portal, Notebook, or an external client.

The following IVOA services are available at the time of the DP1 release:

• Table Access Protocol (TAP) Service: A TAP service (P. Dowler et al. 2019) enables queries of catalog data via the IVOA-standard ADQL, a dialect of SQL92 with spherical geometry extensions. The main TAP service for DP1 runs on the Rubin-developed Qserv database (§ 6.5), which hosts the core science tables described in §3.2, as well as the Visit database. It also provides image metadata in the IVOA ObsCore format via the standard ivoa. ObsCore table, making it an "ObsTAP" service (ObsTAP; M. Louys et al. 2017). The TAP service is based on the Canadian Astronomy Data Centre (CADC)'s open-source Java TAP implementation<sup>101</sup>, modified for the exact query language accepted by Qserv. It currently supports a large subset of ADQL, with limitations documented in the data release materials (see §7.1) and exposed via the TAP capabilities endpoint where possible.

The TAP service provides metadata annotations consistent with the standard, including table and column descriptions, indications of foreign-key relationships between tables, and column metadata

<sup>101</sup> https://github.com/opencadc/tap

such as units and IVOA Unified Content Descriptors (UCDs).

2651

2653

2654

2655

2658

2663

2668

2674

2675

2678

2679

2680

2681

2682

2693

2600

2601

2602

2603

2604

2605

2607

2608

2610

2611

2612

2613

2614

2615

2616

2617

2618

2619

2620

2621

2622

2623

2624

2625

2626

2627

2628

2629

2630

2631

2632

2633

2634

2635

2636

2637

2638

2639

2640

2641

2642

2643

2644

2645

2646

2647

• Image Access Services: Rubin image access services are compliant with IVOA SIAv2 (Simple Image Access Protocol, version 2; T. Jenness et al. 2024; P. Dowler et al. 2015) for discovering and accessing astronomical images based on metadata. SIAv2 is a REpresentational State Transfer (REST)-based protocol designed for the discovery and retrieval of image data. It allows, for instance, querying all images in a given band over a defined sky region and time period.

Users identify an image or observation of interest and query the service. The result set includes metadata about the image, such as the sky position, time, or band, and a data access URL, which includes an IVOA Identifier uniquely identifying the dataset (T. Jenness & G. P. Dubois-Felsmann 2025), allowing the dataset to be retrieved or a cutout requested via Server-side Operations for Data Access (IVOA standard) (SODA).

- Image Cutout Service: The Rubin Cutout Service (R. Allbery 2023, 2024) is based on the IVOA SODA standard (F. Bonnarel et al. 2017). Users submit requests specifying sky coordinates and the cutout size as the radius from the coordinates, and the service performs the operation on the full image and returns a result set. For DP1, the cutout service is a single cutout service only where N cutout requests will require N independent synchronous calls. We expect some form of bulk cutout service by mid 2026, approximately contemporaneously with DP2.
- **HiPS Data Service**: An authenticated HiPS (P. Fernique et al. 2017) data service for seamless pan-and-zoom access to large-scale co-adds. It supports fast interactive progressive image exploration at a range of resolutions.
- WebDAV: A Web Distributed Authoring and Versioning (WebDav) service is provided to enable users to remotely manage, edit, and organize files and directories on the RSP as if they were local files on their own computer. This is especially useful for local development.

## 6.2.2. Data Butler

The Rubin Data Butler (T. Jenness et al. 2022; N. B. Lust et al. 2023), is a high-level interface designed to facilitate seamless access to data for both users and

software systems. This includes managing storage formats, physical locations, data staging, and database mappings. A Butler repository contains two components:

- the *Data Store*: A physical storage system for datasets, e.g., a Portable Operating System Interface (POSIX) file system or S3 object store; and
- the *Registry*: An Structured Query Language (SQL)-compatible database that stores metadata about the datasets in the data store.

For DP1, the Butler repository is hosted in the Google Cloud, using an (Amazon) Simple Storage Service (S3)-compatible store for datasets and AlloyDB, a PostgreSQL-compatible database, for the registry.

In the context of the Butler, a dataset refers to a unique data product, such as an image, catalog or map, generated by the observatory or processing pipelines Datasets belong to one of the various types of data products, described in §3. The Butler ensures that each dataset is uniquely identifiable by a combination of three pieces of information: a data coordinate, a dataset type, and a run collection. For example, a dataset that represents a single raw image in the i band taken on the night starting 2024-11-11 with exposure ID 2024111100074 would be represented as dataId='exposure':2024111100074, 'band':'i', 'instrument':'LSSTComCam' and is associated with the raw DatasetType. For a deep coadd on a patch of sky in the Seagull field, there would be no exposure dimensions and instead the tract, patch and band would specified as dataId='tract':7850, 'patch': 6, 'band': 'g', 'instrument': 'LSSTComCam', skymap='lsst\_cells\_v1' and is associated with the deep coadd DatasetType.

The data coordinate is used to locate a dataset in multi-dimensional space, where dimensions are defined in terms of scientifically meaningful concepts, such as instrument, visit, detector or band. For example, a calibrated single-visit image (§3.1) has dimensions including band, instrument, and detector. In contrast, the visit table (§3.2), a catalog of all calibrated single-epoch visits in DP1, has only the instrument dimension. The main dimensions used in DP1 are listed, together with a brief description, in Table 6. To determine which dimensions are relevant for a specific dataset, the Butler defines dataset types, which associate each dataset with its specific set of relevant dimensions, as well as the associated Python type representing the dataset. The dataset type defines the kind of data a dataset represents, such as a raw image (raw), a processed catalog (object\_forced\_source), or a sky map (skyMap). Table 7 lists

2700

2701

2702

2703

2704

2707

2708

2709

2710

2711

2713

2714

2715

2716

2717

2719

2721

2722

2723

2725

2726

2727

2728

2729

2732

**Table 6.** Descriptions of and valid values for the key data dimensions in DP1. YYYYMMDD signifies date and # signifies a single 0–9 digit.

Dimension	Format/Valid values	Description	
day_obs	YYYYMMDD	A day and night of observations that rolls over during daylight hours.	
visit	YYYYMMDD#####	A sequence of observations processed together; synonymous with "exposure" in DP1.	
exposure	YYYYMMDD#####	A single exposure of all nine ComCam detectors.	
instrument	LSSTComCam	The instrument name.	
detector	0-8	A ComCam detector.	
skymap	lsst_cells_v1	A set of tracts and patches that subdivide the sky into rectangular regions with simple projections and intentional overlaps.	
tract	See Table 3	A large rectangular region of the sky.	
patch	0-99	A rectangular region within a tract.	
physical_filter	u_02, g_01, i_06, r_03,	A physical filter.	
	z_03, y_04		
band	u, g, r, i, z, y	An conceptual astronomical passband.	

2734

2749

all the dataset types available via the Butler in DP1, together with the dimensions needed to uniquely identify a specific dataset and the number of unique datasets of each type.

It is important to highlight a key difference between accessing catalog data via the TAP service versus the Butler. While the TAP service contains entire catalogs, many of the same catalogs in the Butler are split into multiple separate catalogs. This is partly due to how these catalogs are generated, but also because of the way data is stored within and retrieved from the Butler repository – it is inefficient to retrieve the entire Source catalog, for example, from the file system. Instead, because the Source catalog contains data for sources detected in the visit\_images, there is one Source catalog in the Butler for each visit image. Similarly, there is one Object catalog for each deep\_coadd. All the catalogs described in §3.2, aside from the CcdVisit, SSObject, SSSource, and Calibration catalogs, are split within the Butler.

A dataset is associated with one or more *Collections*; logical groupings of datasets within the Butler system that were created or processed together by the same batch operation. Collections allow multiple datasets with the same data coordinate to coexist without conflict. Collections support flexible, parallel processing by enabling repeated analyses of the same input data using different configurations.

For DP1, a subset of the consolidated database contents (§6.5.2) is accessible through the Data Butler. However, not all metadata from the Visit table (§3.5) are available. The DP1 Butler is read-only; a writeable Butler is expected by mid-2026, around the time of DP2.

#### 6.2.3. Remote Programmatic Access

The Rubin RSP API can be accessed from a local system by data rights holders outside of the RSP, by creating a user security token. This token can then be used as a bearer token for API calls to the RSP TAP service. This capability is especially useful for remote data analysis using tools such as TOPCAT, as well as enabling third-party systems, e.g., Community Alert Brokers, to access Rubin data. Additionally, it supports remote development, allowing for more flexible workflows and integration with external systems.

## 6.3. Portal Aspect

The Portal Aspect provides an interactive web-based environment for exploratory data discovery, filtering, querying ,and visualization of both image and catalog data, without requiring programming expertise. It enables users to access and analyze large datasets via tools for catalog queries, image browsing, time-series inspection, and cross-matching.

The Portal is built on Firefly (X. Wu et al. 2019), a web application framework developed by the Infrared Processing and Analysis Center (IPAC). Firefly provides interactive capabilities such as customizable table views, image overlays, multi-panel visualizations, and synchronized displays linking catalog and image data.

Designed to support both exploratory data access and detailed scientific investigation, the Portal delivers an intuitive user experience, allowing users to visually analyze data while retaining access to underlying metadata and query controls.

**Table 7.** The name and number of each type of data product in the Butler and the dimensions required to identify a specific dataset.

Data Product	Name in Butler	Required Dimensions	Number in DP1
Image Data Products			
raw	raw	instrument, detector, exposure	16125
visit_image	visit_image	instrument, detector, visit	15972
deep_coadd	deep_coadd	band, skymap, tract, patch	2644
template_coadd	template_coadd	band, skymap, tract, patch	2730
difference_image	difference_image	instrument, detector, visit	15972
Catalog Data Products			
Source	source	instrument, visit	1786
Object	object	skymap, tract	29
ForcedSource	object_forced_source	skymap, tract, patch	636
DiaSource	dia_source	skymap, tract	25
DiaObject	dia_object	skymap, tract	25
ForcedSourceOnDiaObject	dia_object_forced_source	skymap, tract, patch	597
SSSource	ss_source	_	1
SSObject	ss_object	_	1
Visit	visit_table	instrument	1
CCDVisit	visit_detector_table	instrument	1

# 6.4. Notebook Aspect

The Notebook Aspect provides an interactive, web-based environment built on Jupyter Notebooks, enabling users to write and execute Python code directly on Rubin and LSST data without downloading it locally. It offers programmatic access to Rubin and LSST data products, allowing users to query and retrieve datasets, manipulate and display images, compute derived properties, plot results, and reprocess data using the LSST Science Pipelines (§4.1). The environment comes preinstalled with the pipelines and a broad set of widely used astronomical software tools, supporting immediate and flexible data analysis.

#### 6.5. Databases

The user-facing Aspects of the RSP are supported by several backend databases that store catalog data products, image metadata, and other derived datasets. The schema for DP1 and other Rubin databases are available online at https://sdm-schemas.lsst.io.

#### 6.5.1. *Qserv*

The final 10-year LSST catalog is expected to reach 15 PB and contain measurements for billions of stars and galaxies across trillions of detections. To support efficient storage, querying, and analysis of this dataset, Rubin Observatory developed Qserv (D. L. Wang et al. 2011; F. Mueller et al. 2023) – a scalable, parallel, dis-

tributed SQL database system. Qserv partitions data over approximately equal-area regions of the celestial sphere, replicates data to ensure resilience and high availability, and uses shared scanning to reduce overall I/O load. It also supports a package of scientific user-defined functions (SciSQL: https://smonkewitz.github.io/scisql/) simplifying complex queries involving spherical geometry, statistics, and photometry. Qserv is built on robust production-quality components, including MariaDB (https://www.mariadb.org/) and XRootD (https://xrootd.org/). Qserv runs at the USDF and user access to catalog data is via the TAP service (§6.2.1). This enables catalog-based analysis through both the RSP Portal and Notebook Aspects.

Although the small DP1 dataset does not require Qserv's full capabilities, we nevertheless chose to use it for DP1 to accurately reflect the future data access environment and to gain experience with scientifically-motivated queries ahead of full-scale deployment. Qserv is open-source and available on GitHub: https://github.com/lsst/qserv.

#### 6.5.2. Consolidated Database

The Consolidated Database (ConsDB) (K.-T. Lim 2025) is an SQL-compatible database designed to store and manage metadata for Rubin Observatory science and calibration images. Metadata are recorded on a perexposure basis and includes information such as the tar-

2817

2819

2820

2821

2823

2824

2826

2827

2828

2830

2831

2832

2833

2834

2835

2837

2838

2839

2840

2841

2842

2843

2844

2845

2846

2847

2848

2850

2851

2853

2854

2856

2857

2858

2859

2860

2862

get name, pointing coordinates, observation time, physical filter and band, exposure duration, and environmental conditions (e.g., temperature, humidity, and wind speed). These key image metadata are also stored in the Butler Registry (§6.2.2), however the ConsDB stores additional information including derived metrics from image processing and information from the Engineering and Facility Database (EFD) transformed from the time dimension to the exposure dimension.

The ConsDB schema is organized into instrument-specific tables, e.g., LSSTComCam and LSSTCam, facilitating instrument-specific queries. Within the LSST-ComCam schema, data is further structured into tables for individual exposures and detectors. An example query on the DP1 dataset might retrieve all visits within a specified time range in the r-band for a given DP1 target.

The ConsDB is hosted at the USDF. Following the initial release of DP1, a release of the DP1 exposure-specific ConsDB data will be made available through the RSP, and accessible externally via TAP. The detailed LSSTComCam schema can be found at: https://sdm-schemas.lsst.io/cdb\_lsstcomcam.html

#### 7. SUPPORT FOR COMMUNITY SCIENCE

The Rubin Observatory has a science community that encompasses thousands of individuals worldwide, with a broad range of experience and expertise in astronomy in general, and in the analysis of optical imaging data specifically.

Rubin's model to support this diverse community to access and analyze DP1 emphasizes self-help via documentation and tutorials, and employs an open platform for asynchronous issue reporting that enables crowd-sourced solutions. These two aspects of community support are augmented by virtual engagement activities. In addition, Rubin supports its Users Committee to advocate on behalf of the science community, and supports the eight LSST Science Collaborations (§7.6).

All of the resources for scientists that are discussed in this section are discoverable by browsing the For Scientists pages of the Rubin Observatory website<sup>102</sup>.

## 7.1. Documentation

The data release documentation for DP1<sup>103</sup> provides an overview of the LSSTComCam observations, detailed descriptions of the data products, and a high-level summary of the processing pipelines. Although much of its content overlaps significantly with this paper, the documentation is presented as a searchable, web-based resource built using Sphinx<sup>104</sup>, with a focus on enabling scientific use of the data products.

## $7.2. \ Tutorials$

A suite of tutorials that demonstrate how to access and analyze DP1 using the RSP acompanies the DP1 release. Jupyter Notebook tutorials are available via the "Tutorials" drop-down menu within the Notebook aspect of the RSP. Tutorials for the Portal and API aspects of the RSP can be found in the data release documentation.

2869

2883

2889

2897

2898

2900

2903

These tutorials are designed to be inclusive, accessible, clear, focused, and consistent. Their format and contents follow a set of guidelines (M. L. Graham et al. 2025) that are informed by modern standards in technical writing.

## 7.3. Community Forum

The venue for all user support is the Rubin Community Forum  $^{105}$ .

Questions about any and all aspects of the Rubin data products, pipelines, and services should be posted as new topics in the Support category. This includes beginner-level and "naive" questions, advanced scientific analysis questions, technical bug reports, account and data access issues, and everything in between. The Support category of the Forum is monitored by Rubin staff, who aim to respond to all new unsolved topics within 24 hours.

The Rubin Community Forum is built on the opensource Discourse platform. It was chosen because, for a worldwide community of ten thousand Rubin users, a traditional (i.e., closed) help desk represents a risk to Rubin science (e.g., many users with the same question having to wait for responses). The open nature of the Forum enables self-help by letting users search for similar issues, and enables crowd-sourced problem solving (and avoids knowledge bottlenecks) by letting users help users.

# 7.4. Engagement Activities

A variety of live virtual and in-person workshops and seminars offer learning opportunities to scientists and students working with DP1.

 Rubin Science Assemblies (weekly, virtual, 1 hour): alternates between hands-on tutorials based on the most recent data release and open drop-in "office hours" with Rubin staff.

https://rubinobservatory.org/https://dp1.lsst.io

https://www.sphinx-doc.org/https://community.lsst.org/

Rubin DP1 45

• Rubin Data Academy (annual, virtual, 3-4 days): 2957 an intense set of hands-on tutorials based on the most recent data release, along with co-working and networking sessions.

2960

2966

2970

2971

2978

2979

2981

2982

2985

2986

2987

2988

2990

2993

2994

2996

2999

3002

3003

2909

2910

2911

2912

2913

2914

2915

2916

2917

2918

2919

2921

2922

2923

2924

2925

2926

2928

2929

2930

2931

2932

2933

2935

2936

2937

2938

2939

2940

2941

2943

2944

2946

2947

2948

2949

2950

2951

2952

2953

2954

2955

2956

• Rubin Community Workshop (annual, virtual, 5 days), a science-focused conference of contributed posters, talks, and sessions led by members of the Rubin science community and Rubin staff

For schedules and connection information, visit the For Scientists pages of the Rubin Observatory website. Requests for custom tutorials and presentations for research groups are also accommodated.

## 7.5. Users Committee

This committee is charged with soliciting feedback from the science community, advocating on their behalf, and recommending science-driven improvements to the LSST data products and the Rubin Science Platform tools and services. Community members are encouraged to attend their virtual meetings and raise issues to their attention, so they can be included in the committee's twice-yearly reports to the Rubin Observatory Director.

The community's response to DP1 will be especially valuable input to DP2 and Data Release 1 (DR1), and the Users Committee encourages all users to interact with them. For a list of members and contact information, visit the For Scientists pages of the Rubin Observatory website.

# 7.6. Science Collaborations

The eight LSST Science Collaborations are independent, worldwide communities of scientists, self-organized into collaborations based on their research interests and expertise. Members work together to apply for funding, build software infrastructure and analysis algorithms, and incorporate external data sets into their LSSTbased research.

The Science Collaborations also provide valuable advice to Rubin Observatory on the operational strategies and data products to accomplish specific science goals, and Rubin Observatory supports the collaborations via staff liaisons and regular virtual meetings with Rubin operations leadership.

#### 8. SUMMARY AND FUTURE RELEASES

Rubin Data Preview 1 (DP1) offers an initial look at the first on-sky data products and access services from the Vera C. Rubin Observatory. DP1 forms part of Rubin's Early Science Program, and provides the scientific community with an early opportunity to familiarize

themselves with the data formats and access infrastructure for the forthcoming Legacy Survey of Space and Time. This early release has a proprietary period of two years, during which time it is available to Rubin data rights holders only via the cloud-based Rubin Science Platform (RSP).

In this paper we have described the completion status of the observatory at the time of data acquisition, the commissioning campaign that forms the basis of DP1, and the processing pipelines used to produce early versions of data products. We provide details on the data products, their characteristics and known issues, and describe the Rubin Science Platform for access to and analysis of DP1.

The data products described in this paper derive from observations obtained by LSSTComCam. LSSTCom-Cam contains only around 5% the number of CCDs as the full LSST Science Camera (LSSTCam), yet the DP1 dataset that it has produced will already enable a very broad range of science. At 3.5 TB in size, DP1 covers a total area of  $\sim 15 \text{ deg}^2$  and contains 1792 single-epoch images, 2644 deep coadded images and 2.3 million distinct astrophysical objects, including 93 new asteroid discoveries.

While some data products anticipated from the LSST are not yet available, e.g., cell-based coadds, DP1 includes several products that will not be provided in future releases. Notably, difference images are included in DP1 as pre-generated products; in future releases, these will instead be generated on demand via dedicated services. The inclusion of pre-generated difference images in DP1 is feasible due to the relatively small size of the dataset, an approach that will not scale to the significantly larger data volumes expected in subsequent releases.

The RSP is continually under development, and new functionality will continue to be deployed incrementally as it becomes available, and independent of the future data release schedule. User query history capabilities, context-aware documentation and a bulk cutout services are just a few of the services currently under develop-

Coincident with the release of DP1, Rubin Observatory begins its Science Validation Surveys with the LSST Science Camera. This final commissioning phase will produce a dataset that will form the foundation for the second Rubin Data Preview, DP2, expected around mid-to-late 2026. Full operations, marking the start of the LSST, are expected to commence by the end of 2025.

3009

3010

3012

3013

3014

3015

3016

3017

3018

3019

3020

#### ACKNOWLEDGMENTS

. This material is based upon work supported in part by the National Science Foundation through Cooperative Agreements AST-1258333 and AST-2241526 and Cooperative Support Agreements AST-1202910 and AST-2211468 managed by the Association of Universities for Research in Astronomy (AURA), and the Department of Energy under Contract No. DE-AC02-76SF00515 with the SLAC National Accelerator Laboratory managed by Stanford University. Additional Rubin Observatory funding comes from private donations, grants to universities, and in-kind support from LSST-DA Institutional Members.

This work has been supported by the French National Institute of Nuclear and Particle Physics (IN2P3)

through dedicated funding provided by the National Center for Scientific Research (CNRS).

This work has been supported by STFC funding for UK participation in LSST, through grant ST/Y00292X/1.

Facilities: Rubin:Simonyi (LSSTComCam), Rubin:USDAC

Software: Rubin Data Butler (T. Jenness et al. 2022), LSST Science Pipelines (Rubin Observatory Science Pipelines Developers 2025), LSST Feature Based Scheduler v3.0 (P. Yoachim et al. 2024; E. Naghib et al. 2019) Astropy (Astropy Collaboration et al. 2013, 2018, 2022) PIFF (M. Jarvis et al. 2021), GBDES (G. M. Bernstein 2022), Qserv (D. L. Wang et al. 2011; F. Mueller et al. 2023), Slurm, HTCondor, CVMFS, FTS3, ESNet

#### APPENDIX

3036

3028

3030

3033

#### REFERENCES

```
Abazajian, K., Adelman-McCarthy, J. K., Agüeros, M. A.,
                                                                         Astropy Collaboration, Robitaille, T. P., Tollerud, E. J.,
3039
                                                                    3063
       et al. 2004, AJ, 128, 502, doi: 10.1086/421365
                                                                           et al. 2013, A&A, 558, A33,
3040
                                                                    3064
                                                                           doi: 10.1051/0004-6361/201322068
     Ahumada, R., Allende Prieto, C., Almeida, A., et al. 2020,
                                                                    3065
3041
       ApJS, 249, 3, doi: 10.3847/1538-4365/ab929e
                                                                         Astropy Collaboration, Price-Whelan, A. M., Sipőcz, B. M.,
                                                                    3066
3042
                                                                           et al. 2018, AJ, 156, 123, doi: 10.3847/1538-3881/aabc4f
     Aihara, H., AlSayyad, Y., Ando, M., et al. 2022, PASJ, 74,
                                                                    3067
3043
       247, doi: 10.1093/pasj/psab122
                                                                         Astropy Collaboration, Price-Whelan, A. M., Lim, P. L.,
                                                                    3068
3044
     Allbery, R. 2023, IVOA SODA implementation experience,
                                                                           et al. 2022, ApJ, 935, 167, doi: 10.3847/1538-4357/ac7c74
3045
       SQuaRE Technical Note SQR-063, NSF-DOE Vera C.
                                                                         Baumann, M., Boch, T., Pineau, F.-X., et al. 2022, in
                                                                    3070
3046
       Rubin Observatory. https://sqr-063.lsst.io/
                                                                           Astronomical Society of the Pacific Conference Series,
3047
                                                                    3071
     Allbery, R. 2024, Draft IVOA SODA web service
                                                                           Vol. 532, Astronomical Data Analysis Software and
3048
                                                                    3072
       specification, SQuaRE Technical Note SQR-093,
                                                                           Systems XXX, ed. J. E. Ruiz, F. Pierfedereci, &
                                                                    3073
3049
       NSF-DOE Vera C. Rubin Observatory.
                                                                           P. Teuben, 7
                                                                    3074
3050
       https://sqr-093.lsst.io/
                                                                         Bechtol, K., Sevilla-Noarbe, I., Drlica-Wagner, A., et al.
                                                                    3075
     AlSayyad, Y. 2018, Coaddition Artifact Rejection and
                                                                    3076
                                                                           2025, arXiv e-prints, arXiv:2501.05739,
3052
       CompareWarp, Data Management Technical Note
                                                                           doi: 10.48550/arXiv.2501.05739
                                                                    3077
3053
       DMTN-080, NSF-DOE Vera C. Rubin Observatory,
                                                                         Berk, A., Anderson, G. P., Bernstein, L. S., et al. 1999, in
3054
                                                                    3078
       doi: 10.71929/rubin/2583441
                                                                           Society of Photo-Optical Instrumentation Engineers
3055
                                                                    3079
                                                                           (SPIE) Conference Series, Vol. 3756, Optical
     Ansel, J., Yang, E., He, H., et al. 2024, in 29th ACM
3056
                                                                    3080
       International Conference on Architectural Support for
                                                                           Spectroscopic Techniques and Instrumentation for
3057
       Programming Languages and Operating Systems, Volume
                                                                           Atmospheric and Space Research III, ed. A. M. Larar,
                                                                    3082
3058
       2 (ASPLOS '24) (ACM), doi: 10.1145/3620665.3640366
                                                                           348-353, doi: 10.1117/12.366388
                                                                    3083
3059
     Antilogus, P., Astier, P., Doherty, P., Guyonnet, A., &
                                                                         Bernstein, G. M. 2022, gbdes: DECam instrumental
3060
                                                                    3084
       Regnault, N. 2014, Journal of Instrumentation, 9,
                                                                           signature fitting and processing programs,, Astrophysics
3061
                                                                    3085
       C03048, doi: 10.1088/1748-0221/9/03/C03048
                                                                           Source Code Library, record ascl:2210.011
3062
                                                                    3086
```

Bernstein, G. M., & Jarvis, M. 2002, AJ, 123, 583, Eggl, S., Juric, M., Moeyens, J., & Jones, L. 2020, in 3087 3134 doi: 10.1086/338085 AAS/Division for Planetary Sciences Meeting Abstracts, 3088 3135 Vol. 52, AAS/Division for Planetary Sciences Meeting Bernstein, G. M., Armstrong, R., Plazas, A. A., et al. 2017, 3136 3089 Abstracts, 211.01 PASP, 129, 074503, doi: 10.1088/1538-3873/aa6c55 3137 3090 Esteves, J. H., Utsumi, Y., Snyder, A., et al. 2023, PASP, Bertin, E. 2011, in Astronomical Society of the Pacific 3138 3091 135, 115003, doi: 10.1088/1538-3873/ad0a73 3139 Conference Series, Vol. 442, Astronomical Data Analysis 3092 Euclid Collaboration, Romelli, E., Kümmel, M., et al. 2025, 3140 Software and Systems XX, ed. I. N. Evans, 3093 arXiv e-prints, arXiv:2503.15305, 3141 A. Accomazzi, D. J. Mink, & A. H. Rots, 435 3094 doi: 10.48550/arXiv.2503.15305 3142 Bianco, F. B., Ivezić, Ž., Jones, R. L., et al. 2022, ApJS, 3095 Fagrelius, P., & Rykoff, E. S. 2025, Rubin Observatory 3143 258, 1, doi: 10.3847/1538-4365/ac3e72 3096 Baseline Calibration Plan, Commissioning Technical 3144 Blum, R., & the Rubin Operations Team. 2020, Vera C. 3097 Note SITCOMTN-086, NSF-DOE Vera C. Rubin 3145 Rubin Observatory Data Policy, Data Management 3098 Observatory, doi: 10.71929/rubin/2583850 3146 Operations Controlled Document RDO-013, NSF-DOE 3099 Ferguson, P. S., Rykoff, E. S., Carlin, J. L., Saunders, C., & 3147 Vera C. Rubin Observatory. https://ls.st/RDO-013 Parejko, J. K. 2025, The Monster: A reference catalog 3148 Boch, T., & Fernique, P. 2014, in Astronomical Society of 3101 with synthetic ugrizy-band fluxes for the Vera C. Rubin 3149 the Pacific Conference Series, Vol. 485, Astronomical 3102 observatory, Data Management Technical Note 3150 Data Analysis Software and Systems XXIII, ed. 3103 DMTN-277, NSF-DOE Vera C. Rubin Observatory, 3151 N. Manset & P. Forshay, 277 3104 doi: 10.71929/rubin/2583688 3152 Bonnarel, F., Dowler, P., Demleitner, M., Tody, D., & 3105 Fernique, P., Allen, M. G., Boch, T., et al. 2015, A&A, 578, 3153 Dempsey, J. 2017, IVOA Server-side Operations for Data 3106 A114, doi: 10.1051/0004-6361/201526075 3154 Access Version 1.0,, IVOA Recommendation 17 May 2017 3107 Fernique, P., Allen, M., Boch, T., et al. 2017, HiPS -3155 doi: 10.5479/ADS/bib/2017ivoa.spec.0517B Hierarchical Progressive Survey Version 1.0,, IVOA 3108 3156 Bonnarel, F., Fernique, P., Bienaymé, O., et al. 2000, Recommendation 19 May 2017 3109 3157 A&AS, 143, 33, doi: 10.1051/aas:2000331 doi: 10.5479/ADS/bib/2017ivoa.spec.0519F 3110 3158 Fortino, W. F., Bernstein, G. M., Bernardinelli, P. H., et al. Bosch, J., Armstrong, R., Bickerton, S., et al. 2018, PASJ, 3159 3111 2021, AJ, 162, 106, doi: 10.3847/1538-3881/ac0722 70, S5, doi: 10.1093/pasj/psx080 3160 3112 Gaia Collaboration, Montegriffo, P., Bellazzini, M., et al. Broughton, A., Utsumi, Y., Plazas Malagón, A. A., et al. 3161 3113 2023a, A&A, 674, A33, 2024, PASP, 136, 045003, doi: 10.1088/1538-3873/ad3aa2 3162 3114 doi: 10.1051/0004-6361/202243709 Burke, D. L., Rykoff, E. S., Allam, S., et al. 2018, AJ, 155, 3115 Gaia Collaboration, Vallenari, A., Brown, A. G. A., et al. 3164 41, doi: 10.3847/1538-3881/aa9f22 3116 2023b, A&A, 674, A1, doi: 10.1051/0004-6361/202243940 3165 Chambers, K. C., Magnier, E. A., Metcalfe, N., et al. 2016, 3117 Górski, K. M., Hivon, E., Banday, A. J., et al. 2005, ApJ, 3166 arXiv e-prints, arXiv:1612.05560, 3118 622, 759, doi: 10.1086/427976 3167 doi: 10.48550/arXiv.1612.05560 3119 Graham, A. W., & Driver, S. P. 2005, PASA, 22, 118, 3168 Choi, Y., Olsen, K. A. G., Carlin, J. L., et al. 2025, arXiv 3120 doi: 10.1071/AS05001 3169 e-prints, arXiv:2507.01343, 3121 Graham, M., Plante, R., Tody, D., & Fitzpatrick, M. 2014, 3170 doi: 10.48550/arXiv.2507.01343 3122 PyVO: Python access to the Virtual Observatory, 3171 de Vaucouleurs, G. 1948, Annales d'Astrophysique, 11, 247 3123 Astrophysics Source Code Library, record ascl:1402.004 3172 de Vaucouleurs, G. 1953, MNRAS, 113, 134, 3124 Graham, M. L., Carlin, J. L., Adair, C. L., et al. 2025, 3173 doi: 10.1093/mnras/113.2.134 3125 Guidelines for User Tutorials, Technical Note RTN-045, 3174 Dowler, P., Bonnarel, F., & Tody, D. 2015, IVOA Simple 3126 NSF-DOE Vera C. Rubin Observatory, 3175 Image Access Version 2.0,, IVOA Recommendation 23 3127 doi: 10.71929/rubin/2584020 3176 December 2015 3128 Gray, B. 2025, find orb: Orbit determination from 3177 doi: 10.5479/ADS/bib/2015ivoa.spec.1223D 3129 observations, https://github.com/Bill-Gray/find\_orb 3178 Dowler, P., Rixon, G., Tody, D., & Demleitner, M. 2019, Guy, L. P., Bechtol, K., Bellm, E., et al. 2025, Rubin 3130 3179 Table Access Protocol Version 1.1,, IVOA 3131 Observatory Plans for an Early Science Program, 3180 Recommendation 27 September 2019 Technical Note RTN-011, NSF-DOE Vera C. Rubin 3132 3181 doi: 10.5479/ADS/bib/2019ivoa.spec.0927D Observatory, doi: 10.71929/rubin/2584021 3133 3182

```
Heinze, A., Eggl, S., Juric, M., et al. 2022, in AAS/Division
                                                                        Juric, M. 2025, mpsky: Multi-purpose sky catalog
3183
       for Planetary Sciences Meeting Abstracts, Vol. 54.
                                                                           cross-matching, https://github.com/mjuric/mpsky
3184
                                                                   3234
       AAS/Division for Planetary Sciences Meeting Abstracts,
                                                                        Jurić, M., Ciardi, D., Dubois-Felsmann, G., & Guy, L.
3185
                                                                   3235
       504.04
                                                                           2019, LSST Science Platform Vision Document, Systems
                                                                   3236
3186
     Heinze, A., Juric, M., & Kurlander, J. 2023, heliolinx: Open
                                                                           Engineering Controlled Document LSE-319, NSF-DOE
                                                                   3237
3187
       Source Solar System Discovery Software,
                                                                           Vera C. Rubin Observatory, doi: 10.71929/rubin/2587242
                                                                   3238
3188
       https://github.com/heliolinx/heliolinx
                                                                        Jurić, M., Axelrod, T., Becker, A., et al. 2023, Data
                                                                   3239
3189
     Hirata, C., & Seljak, U. 2003, MNRAS, 343, 459,
                                                                           Products Definition Document, Systems Engineering
                                                                   3240
3190
       doi: 10.1046/j.1365-8711.2003.06683.x
                                                                           Controlled Document LSE-163, NSF-DOE Vera C. Rubin
3191
                                                                   3241
     Holman, M. J., Payne, M. J., Blankley, P., Janssen, R., &
                                                                           Observatory, doi: 10.71929/rubin/2587118
3192
       Kuindersma, S. 2018, AJ, 156, 135,
                                                                        Kannawadi, A. 2025, Consistent galaxy colors with
3193
                                                                   3243
                                                                           Gaussian-Aperture and PSF photometry, Data
       doi: 10.3847/1538-3881/aad69a
3194
                                                                   3244
     Howard, J., Reil, K., Claver, C., et al. 2018, in Society of
                                                                           Management Technical Note DMTN-190, NSF-DOE Vera
3195
                                                                   3245
       Photo-Optical Instrumentation Engineers (SPIE)
                                                                           C. Rubin Observatory, doi: 10.71929/rubin/2583849
                                                                   3246
       Conference Series, Vol. 10700, Ground-based and
                                                                        Kron, R. G. 1980, ApJS, 43, 305, doi: 10.1086/190669
                                                                   3247
3197
       Airborne Telescopes VII, ed. H. K. Marshall &
                                                                        Kuijken, K. 2008, A&A, 482, 1053,
3198
                                                                   3248
       J. Spyromilio, 107003D, doi: 10.1117/12.2312684
                                                                           doi: 10.1051/0004-6361:20066601
3199
                                                                   3249
     Illingworth, G., Magee, D., Bouwens, R., et al. 2016, arXiv
                                                                        Lange, T., Nordby, M., Pollek, H., et al. 2024, in Society of
3200
                                                                   3250
       e-prints, arXiv:1606.00841,
                                                                           Photo-Optical Instrumentation Engineers (SPIE)
3201
                                                                   3251
       doi: 10.48550/arXiv.1606.00841
                                                                           Conference Series, Vol. 13096, Ground-based and
3202
                                                                   3252
     Ingraham, P., Fagrelius, P., Stubbs, C. W., et al. 2022, in
                                                                           Airborne Instrumentation for Astronomy X. ed. J. J.
3203
                                                                   3253
       Society of Photo-Optical Instrumentation Engineers
                                                                           Bryant, K. Motohara, & J. R. D. Vernet, 130961O,
3204
                                                                   3254
       (SPIE) Conference Series, Vol. 12182, Ground-based and
                                                                           doi: 10.1117/12.3019302
3205
                                                                   3255
       Airborne Telescopes IX, ed. H. K. Marshall,
                                                                        Léget, P. F., Astier, P., Regnault, N., et al. 2021, A&A,
3206
                                                                   3256
       J. Spyromilio, & T. Usuda, 121820R,
                                                                           650, A81, doi: 10.1051/0004-6361/202140463
3207
                                                                   3257
       doi: 10.1117/12.2630185
                                                                        Lim, K.-T. 2023, Proposal and Prototype for Prompt
3208
                                                                   3258
     Ivezić, Ž., Kahn, S. M., Tyson, J. A., et al. 2019a, ApJ,
                                                                           Processing, Data Management Technical Note
                                                                   3259
3209
       873, 111, doi: 10.3847/1538-4357/ab042c
                                                                           DMTN-219, NSF-DOE Vera C. Rubin Observatory,
                                                                   3260
3210
3211
     Ivezić, Ž., Kahn, S. M., Tyson, J. A., et al. 2019b, ApJ,
                                                                   3261
                                                                           doi: 10.71929/rubin/2585429
       873, 111, doi: 10.3847/1538-4357/ab042c
                                                                        Lim, K.-T. 2025, The Consolidated Database of Image
3212
                                                                   3262
     Jarvis, M., et al. 2021, Mon. Not. Roy. Astron. Soc., 501,
                                                                           Metadata, Data Management Technical Note
3213
       1282, doi: 10.1093/mnras/staa3679
                                                                           DMTN-227, NSF-DOE Vera C. Rubin Observatory,
3214
                                                                   3264
     Jenness, T., & Dubois-Felsmann, G. P. 2025, IVOA
                                                                           doi: 10.71929/rubin/2586436
                                                                   3265
3215
                                                                        Louys, M., Tody, D., Dowler, P., et al. 2017, Observation
       Identifier Usage at the Rubin Observatory, Data
3216
                                                                   3266
       Management Technical Note DMTN-302, NSF-DOE Vera
                                                                           Data Model Core Components, its Implementation in the
                                                                   3267
3217
       C. Rubin Observatory, doi: 10.71929/rubin/2583848
                                                                           Table Access Protocol Version 1.1,, IVOA
                                                                   3268
3218
     Jenness, T., Voutsinas, S., Dubois-Felsmann, G. P., &
                                                                           Recommendation 09 May 2017
                                                                   3269
3219
       Salnikov, A. 2024, arXiv e-prints, arXiv:2501.00544,
                                                                           doi: 10.5479/ADS/bib/2017ivoa.spec.0509L
3220
                                                                   3270
       doi: 10.48550/arXiv.2501.00544
                                                                        LSST Dark Energy Science Collaboration (LSST DESC),
3221
                                                                   3271
     Jenness, T., Bosch, J. F., Salnikov, A., et al. 2022, in
                                                                           Abolfathi, B., Alonso, D., et al. 2021, ApJS, 253, 31,
3222
                                                                   3272
                                                                           doi: 10.3847/1538-4365/abd62c
       Society of Photo-Optical Instrumentation Engineers
                                                                   3273
3223
       (SPIE) Conference Series, Vol. 12189, Software and
                                                                        Lust, N. B., Jenness, T., Bosch, J. F., et al. 2023, arXiv
                                                                   3274
3224
       Cyberinfrastructure for Astronomy VII, 1218911,
                                                                           e-prints, arXiv:2303.03313,
                                                                   3275
3225
       doi: 10.1117/12.2629569
                                                                           doi: 10.48550/arXiv.2303.03313
                                                                   3276
3226
     Jones, R. L., Yoachim, P., Ivezić, Ž., Neilsen Jr., E. H., &
                                                                        Mandelbaum, R., Hirata, C. M., Seljak, U., et al. 2005,
3227
                                                                   3277
                                                                           MNRAS, 361, 1287,
       Ribeiro, T. 2021, Survey Strategy and Cadence Choices
                                                                   3278
3228
       for the Vera C. Rubin Observatory Legacy Survey of
                                                                           doi: 10.1111/j.1365-2966.2005.09282.x
3229
       Space and Time (LSST), Project Science Technical Note
                                                                        Megias Homar, G., Kahn, S. M., Meyers, J. M., Crenshaw,
                                                                   3280
3230
       PSTN-051, NSF-DOE Vera C. Rubin Observatory,
                                                                           J. F., & Thomas, S. J. 2024, The Astrophysical Journal,
3231
                                                                   3281
       doi: 10.71929/rubin/2584084
                                                                           974, 108, doi: 10.3847/1538-4357/ad6cdc
3232
                                                                   3282
```

```
NSF-DOE Vera C. Rubin Observatory. 2025i, Legacy
     Megias Homar, G., Tighe, R., Thomas, S., et al. 2024, in
3283
                                                                  3330
                                                                        Survey of Space and Time Data Preview 1: ForcedSource
       Ground-based and Airborne Telescopes X, ed. H. K.
3284
                                                                  3331
                                                                        searchable catalog [Data set], NSF-DOE Vera C. Rubin
       Marshall, J. Spyromilio, & T. Usuda, Vol. 13094,
                                                                  3332
3285
                                                                         Observatory, doi: 10.71929/RUBIN/2570327
       International Society for Optics and Photonics (SPIE),
                                                                  3333
3286
                                                                      NSF-DOE Vera C. Rubin Observatory. 2025j, Legacy
                                                                  3334
       130943C, doi: 10.1117/12.3019031
3287
                                                                        Survey of Space and Time Data Preview 1: DiaSource
                                                                  3335
     Melchior, P., Moolekamp, F., Jerdee, M., et al. 2018,
3288
                                                                        searchable catalog [Data set], NSF-DOE Vera C. Rubin
                                                                  3336
       Astronomy and Computing, 24, 129,
                                                                        Observatory, doi: 10.71929/RUBIN/2570317
                                                                  3337
       doi: 10.1016/j.ascom.2018.07.001
3290
                                                                      NSF-DOE Vera C. Rubin Observatory. 2025k, Legacy
                                                                 3338
    Mueller, F., et al. 2023, in ASP Conf. Ser., Vol. TBD,
3291
                                                                        Survey of Space and Time Data Preview 1: DiaObject
                                                                  3339
       ADASS XXXII, ed. S. Gaudet, S. Gwyn, P. Dowler,
3292
                                                                        searchable catalog [Data set], NSF-DOE Vera C. Rubin
                                                                  3340
       D. Bohlender, & A. Hincks (San Francisco: ASP), in
3293
                                                                        Observatory, doi: 10.71929/RUBIN/2570319
                                                                  3341
       press. https://dmtn-243.lsst.io
3294
                                                                      NSF-DOE Vera C. Rubin Observatory. 2025l, Legacy
     Naghib, E., Yoachim, P., Vanderbei, R. J., Connolly, A. J.,
3295
                                                                        Survey of Space and Time Data Preview 1:
                                                                  3343
       & Jones, R. L. 2019, The Astronomical Journal, 157, 151,
                                                                        ForcedSourceOnDiaObject searchable catalog [Data set],
                                                                  3344
       doi: 10.3847/1538-3881/aafece
                                                                        NSF-DOE Vera C. Rubin Observatory,
3297
                                                                  3345
     NSF-DOE Vera C. Rubin Observatory. 2025a, Legacy
                                                                        doi: 10.71929/RUBIN/2570321
3298
                                                                  3346
       Survey of Space and Time Data Preview 1 [Data set],
                                                                      NSF-DOE Vera C. Rubin Observatory. 2025m, Legacy
3299
                                                                  3347
                                                                        Survey of Space and Time Data Preview 1: CcdVisit
       NSF-DOE Vera C. Rubin Observatory,
                                                                  3348
3300
                                                                        searchable catalog [Data set], NSF-DOE Vera C. Rubin
       doi: 10.71929/RUBIN/2570308
                                                                  3349
3301
                                                                        Observatory, doi: 10.71929/RUBIN/2570331
                                                                  3350
     NSF-DOE Vera C. Rubin Observatory. 2025b, Legacy
3302
                                                                      NSF-DOE Vera C. Rubin Observatory. 2025n, Legacy
                                                                  3351
       Survey of Space and Time Data Preview 1: raw dataset
3303
                                                                        Survey of Space and Time Data Preview 1: SSObject
                                                                  3352
       type [Data set], NSF-DOE Vera C. Rubin Observatory,
3304
                                                                        searchable catalog [Data set], NSF-DOE Vera C. Rubin
                                                                  3353
       doi: 10.71929/RUBIN/2570310
3305
                                                                         Observatory, doi: 10.71929/RUBIN/2570335
                                                                  3354
     NSF-DOE Vera C. Rubin Observatory. 2025c, Legacy
3306
                                                                      NSF-DOE Vera C. Rubin Observatory. 2025o, Legacy
                                                                  3355
       Survey of Space and Time Data Preview 1: visit_image
3307
                                                                        Survey of Space and Time Data Preview 1: SSSource
                                                                  3356
       dataset type [Data set], NSF-DOE Vera C. Rubin
3308
                                                                        searchable catalog [Data set], NSF-DOE Vera C. Rubin
                                                                  3357
       Observatory, doi: 10.71929/RUBIN/2570311
3309
                                                                        Observatory, doi: 10.71929/RUBIN/2570333
                                                                  3358
     NSF-DOE Vera C. Rubin Observatory. 2025d, Legacy
3310
                                                                      NSF-DOE Vera C. Rubin Observatory. 2025p, Legacy
                                                                  3359
       Survey of Space and Time Data Preview 1: deep_coadd
3311
                                                                        Survey of Space and Time Data Preview 1: survey
       dataset type [Data set], NSF-DOE Vera C. Rubin
                                                                        property dataset type [Data set], NSF-DOE Vera C.
3312
                                                                  3361
       Observatory, doi: 10.71929/RUBIN/2570313
                                                                        Rubin Observatory, doi: 10.71929/RUBIN/2570315
3313
                                                                      Oke, J. B., & Gunn, J. E. 1983, ApJ, 266, 713,
    NSF-DOE Vera C. Rubin Observatory. 2025e, Legacy
3314
                                                                  3363
                                                                        doi: 10.1086/160817
       Survey of Space and Time Data Preview 1:
                                                                  3364
3315
                                                                      O'Mullane, W., Economou, F., Huang, F., et al. 2024a, in
       template coadd dataset type [Data set], NSF-DOE Vera
                                                                  3365
3316
                                                                        Astronomical Society of the Pacific Conference Series,
       C. Rubin Observatory, doi: 10.71929/RUBIN/2570314
                                                                 3366
3317
                                                                         Vol. 535, Astromical Data Analysis Software and Systems
                                                                  3367
     NSF-DOE Vera C. Rubin Observatory. 2025f, Legacy
3318
                                                                        XXXI, ed. B. V. Hugo, R. Van Rooyen, & O. M.
                                                                  3368
       Survey of Space and Time Data Preview 1:
3319
                                                                        Smirnov, 227, doi: 10.48550/arXiv.2111.15030
                                                                  3369
       difference_image dataset type [Data set], NSF-DOE Vera
3320
                                                                      O'Mullane, W., AlSayyad, Y., Chiang, J., et al. 2024b, in
                                                                  3370
       C. Rubin Observatory, doi: 10.71929/RUBIN/2570312
3321
                                                                        Society of Photo-Optical Instrumentation Engineers
                                                                  3371
     NSF-DOE Vera C. Rubin Observatory. 2025g, Legacy
3322
                                                                        (SPIE) Conference Series, Vol. 13101, Software and
                                                                  3372
       Survey of Space and Time Data Preview 1: Source
3323
                                                                        Cyberinfrastructure for Astronomy VIII, ed. J. Ibsen &
                                                                  3373
       searchable catalog [Data set], NSF-DOE Vera C. Rubin
3324
                                                                        G. Chiozzi, 131012B, doi: 10.1117/12.3018005
                                                                  3374
       Observatory, doi: 10.71929/RUBIN/2570323
3325
                                                                      Onken, C. A., Wolf, C., Bessell, M. S., et al. 2019, PASA,
                                                                  3375
     NSF-DOE Vera C. Rubin Observatory. 2025h, Legacy
3326
                                                                        36, e033, doi: 10.1017/pasa.2019.27
                                                                  3376
       Survey of Space and Time Data Preview 1: Object
3327
                                                                      Park, H. Y., Nomerotski, A., & Tsybychev, D. 2017,
                                                                  3377
       searchable catalog [Data set], NSF-DOE Vera C. Rubin
                                                                        Journal of Instrumentation, 12, C05015,
3328
                                                                  3378
       Observatory, doi: 10.71929/RUBIN/2570325
                                                                        doi: 10.1088/1748-0221/12/05/C05015
3329
                                                                  3379
```

```
Petrosian, V. 1976, ApJL, 210, L53,
                                                                        Rykoff, E. S., Tucker, D. L., Burke, D. L., et al. 2023, arXiv
3380
                                                                   3430
       doi: 10.1086/18230110.1086/182253
                                                                          e-prints, arXiv:2305.01695,
3381
                                                                   3431
     Plazas, A. A., Shapiro, C., Smith, R., Huff, E., & Rhodes,
                                                                          doi: 10.48550/arXiv.2305.01695
3382
                                                                   3432
       J. 2018, Publications of the Astronomical Society of the
                                                                        Saunders, C. 2024, Astrometric Calibration in the LSST
3383
                                                                   3433
       Pacific, 130, 065004, doi: 10.1088/1538-3873/aab820
                                                                          Pipeline, Data Management Technical Note DMTN-266,
3384
                                                                   3434
     Plazas Malagón, A. A., Digel, S. W., Roodman, A.,
                                                                          NSF-DOE Vera C. Rubin Observatory,
3385
                                                                   3435
       Broughton, A., & LSST Camera Team. 2025, LSSTCam
                                                                          doi: 10.71929/rubin/2583846
3386
                                                                   3436
       and LSSTComCam Focal Plane Layouts, Camera
                                                                        Schutt, T., Jarvis, M., Roodman, A., et al. 2025, The Open
3387
                                                                   3437
       Technical Note CTN-001, NSF-DOE Vera C. Rubin
3388
                                                                          Journal of Astrophysics, 8, 26, doi: 10.33232/001c.132299
                                                                   3438
       Observatory, doi: 10.71929/rubin/2584019
3389
                                                                        Sérsic, J. L. 1963, Boletin de la Asociacion Argentina de
                                                                   3439
     Plazas Malagón, A. A., Waters, C., Broughton, A., et al.
3390
                                                                          Astronomia La Plata Argentina, 6, 41
                                                                   3440
       2025, Journal of Astronomical Telescopes, Instruments,
3391
                                                                        Sersic, J. L. 1968, Atlas de Galaxias Australes (Cordoba,
                                                                   3441
       and Systems, 11, 011209,
3392
                                                                          Argentina: Observatorio Astronomico)
                                                                   3442
       doi: 10.1117/1.JATIS.11.1.011209
                                                                        Shanks, T., Metcalfe, N., Chehade, B., et al. 2015,
                                                                   3443
     Refregier, A. 2003, ARA&A, 41, 645,
                                                                          MNRAS, 451, 4238, doi: 10.1093/mnras/stv1130
                                                                   3444
       doi: 10.1146/annurev.astro.41.111302.102207
3395
                                                                        SLAC National Accelerator Laboratory, & NSF-DOE Vera
                                                                   3445
     Reiss, D. J., & Lupton, R. H. 2016, Implementation of
3396
                                                                          C. Rubin Observatory. 2024, LSST Commissioning
                                                                   3446
       Image Difference Decorrelation, Data Management
3397
                                                                          Camera, SLAC National Accelerator Laboratory (SLAC),
                                                                   3447
       Technical Note DMTN-021, NSF-DOE Vera C. Rubin
3398
                                                                          Menlo Park, CA (United States),
                                                                   3448
       Observatory, doi: 10.71929/rubin/2586490
3399
                                                                          doi: 10.71929/RUBIN/2561361
                                                                   3449
     Roodman, A., Rasmussen, A., Bradshaw, A., et al. 2024, in
3400
                                                                        Slater, C. T., Ivezić, Ž., & Lupton, R. H. 2020, AJ, 159, 65,
                                                                   3450
       Society of Photo-Optical Instrumentation Engineers
3401
                                                                          doi: 10.3847/1538-3881/ab6166
                                                                   3451
       (SPIE) Conference Series, Vol. 13096, Ground-based and
3402
                                                                        Smith, G. E. 2010, Rev. Mod. Phys., 82, 2307,
                                                                   3452
       Airborne Instrumentation for Astronomy X, ed. J. J.
3403
                                                                          doi: 10.1103/RevModPhys.82.2307
                                                                   3453
       Bryant, K. Motohara, & J. R. D. Vernet, 130961S,
3404
                                                                        Stalder, B., Reil, K., Claver, C., et al. 2020, in Society of
                                                                   3454
       doi: 10.1117/12.3019698
3405
                                                                          Photo-Optical Instrumentation Engineers (SPIE)
                                                                   3455
     Rubin, V. C., & Ford, Jr., W. K. 1970, ApJ, 159, 379,
3406
                                                                          Conference Series, Vol. 11447, Ground-based and
                                                                   3456
       doi: 10.1086/150317
3407
                                                                          Airborne Instrumentation for Astronomy VIII, ed. C. J.
                                                                   3457
     Rubin, V. C., Ford, Jr., W. K., & Thonnard, N. 1980, ApJ,
3408
                                                                          Evans, J. J. Bryant, & K. Motohara, 114470L,
                                                                   3458
       238, 471, doi: 10.1086/158003
3409
                                                                          doi: 10.1117/12.2561132
                                                                   3459
     Rubin Observatory Science Pipelines Developers. 2025, The
3410
                                                                        Stalder, B., Reil, K., Aguilar, C., et al. 2022, in Society of
                                                                   3460
       LSST Science Pipelines Software: Optical Survey
3411
                                                                          Photo-Optical Instrumentation Engineers (SPIE)
                                                                   3461
       Pipeline Reduction and Analysis Environment, Project
3412
                                                                          Conference Series, Vol. 12184, Ground-based and
                                                                   3462
       Science Technical Note PSTN-019, NSF-DOE Vera C.
3413
                                                                          Airborne Instrumentation for Astronomy IX, ed. C. J.
                                                                   3463
       Rubin Observatory, doi: 10.71929/rubin/2570545
3414
                                                                          Evans, J. J. Bryant, & K. Motohara, 121840J,
                                                                   3464
     Rubin's Survey Cadence Optimization Committee, Bauer,
3415
                                                                          doi: 10.1117/12.2630184
                                                                   3465
       F. E., Brough, S., et al. 2022, Survey Cadence
3416
                                                                        Stalder, B., Munoz, F., Aguilar, C., et al. 2024, in Society
       Optimization Committee's Phase 1 Recommendation,
                                                                   3466
3417
                                                                          of Photo-Optical Instrumentation Engineers (SPIE)
                                                                   3467
       Project Science Technical Note PSTN-053, NSF-DOE
3418
                                                                          Conference Series, Vol. 13094, Ground-based and
       Vera C. Rubin Observatory, doi: 10.71929/rubin/2584276
                                                                   3468
3419
                                                                          Airborne Telescopes X, ed. H. K. Marshall, J. Spyromilio,
     Rubin's Survey Cadence Optimization Committee, Bauer,
                                                                   3469
3420
                                                                          & T. Usuda, 1309409, doi: 10.1117/12.3019266
       F. E., Bianco, F. B., et al. 2023, Survey Cadence
                                                                   3470
3421
                                                                        Swinbank, J., Axelrod, T., Becker, A., et al. 2020, Data
       Optimization Committee's Phase 2 Recommendations,
                                                                   3471
3422
                                                                          Management Science Pipelines Design, Data
       Project Science Technical Note PSTN-055, NSF-DOE
                                                                   3472
3423
                                                                          Management Controlled Document LDM-151, NSF-DOE
       Vera C. Rubin Observatory, doi: 10.71929/rubin/2585249
                                                                   3473
3424
                                                                          Vera C. Rubin Observatory, doi: 10.71929/rubin/2587108
     Rubin's Survey Cadence Optimization Committee, Bianco,
                                                                   3474
3425
                                                                        Taranu, D. S. 2025, The MultiProFit astronomical source
       F. B., Jones, R. L., et al. 2025, Survey Cadence
                                                                   3475
3426
       Optimization Committee's Phase 3 Recommendations,
                                                                   3476
                                                                          modelling code, Data Management Technical Note
3427
                                                                          DMTN-312, NSF-DOE Vera C. Rubin Observatory,
       Project Science Technical Note PSTN-056, NSF-DOE
                                                                   3477
3428
       Vera C. Rubin Observatory, doi: 10.71929/rubin/2585402
                                                                          doi: 10.71929/rubin/2584108
                                                                   3478
```

Rubin DP1 51

```
Taylor, M. 2011, TOPCAT: Tool for OPerations on
3479
       Catalogues And Tables, Astrophysics Source Code
3480
       Library, record ascl:1101.010
3481
     Thomas, S., Connolly, A., Crenshaw, J. F., et al. 2023, in
3482
       Adaptive Optics for Extremely Large Telescopes
3483
       (AO4ELT7), 67, doi: 10.13009/AO4ELT7-2023-069
3484
     Tonry, J. L., Denneau, L., Heinze, A. N., et al. 2018, PASP,
       130, 064505, doi: 10.1088/1538-3873/aabadf
     Wainer, T. M., Davenport, J. R. A., Bellm, E. C., et al.
3487
       2025, Research Notes of the American Astronomical
3488
       Society, 9, 171, doi: 10.3847/2515-5172/adecef
3489
     Wang, D. L., Monkewitz, S. M., Lim, K.-T., & Becla, J.
3490
       2011, in State of the Practice Reports, SC '11 (New
3491
       York, NY, USA: ACM), 12:1-12:11,
3492
       doi: 10.1145/2063348.2063364
3493
     Waters, C. Z., Magnier, E. A., Price, P. A., et al. 2020,
3494
       ApJS, 251, 4, doi: 10.3847/1538-4365/abb82b
3495
```

Whitaker, K. E., Ashas, M., Illingworth, G., et al. 2019, 3496 ApJS, 244, 16, doi: 10.3847/1538-4365/ab3853 3497 Wu, X., Roby, W., Goldian, T., et al. 2019, in Astronomical 3498 Society of the Pacific Conference Series, Vol. 521, 3499 Astronomical Data Analysis Software and Systems 3500 XXVI, ed. M. Molinaro, K. Shortridge, & F. Pasian, 32 3501 Xin, B., Claver, C., Liang, M., et al. 2015, ApOpt, 54, 3502

9045, doi: 10.1364/AO.54.009045 3503 Yoachim, P. 2022, Survey Strategy: Rolling Cadence, 3504 Project Science Technical Note PSTN-052, NSF-DOE 3505 Vera C. Rubin Observatory, doi: 10.71929/rubin/2584109 3506 Yoachim, P., Jones, L., Eric H. Neilsen, J., & Becker, M. R. 3507 2024, lsst/rubin\_scheduler: v3.0.0, v3.0.0 Zenodo,

Zhang, T., Almoubayyed, H., Mandelbaum, R., et al. 2023, 3510 MNRAS, 520, 2328, doi: 10.1093/mnras/stac3350 3511

doi: 10.5281/zenodo.13985198

3508

3509